PERFORMANCE EVALUATION OF A HYBRID (DRY / WET) COOLING SYSTEM

by
André Hendri Graaff

Thesis presented in partial fulfilment of the requirements for the degree of Master of Engineering (Mechanical) in the Faculty of Engineering at Stellenbosch University

Supervisor: Prof. Hanno Carl Rudolf Reuter
Co-Supervisor: Dr. Michael Owen

March 2017

Declaration

By submitting this thesis electronically, I declare that the entirety of the work contained therein is my own, original work, that I am the sole author thereof (save for the extent explicitly otherwise stated), that reproduction and publication thereof by Stellenbosch University will not infringe any third party rights that I have not previously in its entirety or in part submitted it for obtaining any qualification.

Date: March 2017

ABSTRACT

The performance of a hybrid (dry/wet) cooling system (HDWCS) is investigated. The HDWCS aims to compete with dry cooling systems with added performance stability during hot ambient periods. The system consists of two stages – the first, finned tube bundles operating dry, and the second, a bare tube bundle operating dry or wet.

A numerical performance prediction model is developed to predict the performance of the HDWCS in terms of outlet process medium temperature, outlet air temperature and air-side pressure loss. For the finned tube bundles, the heat transfer coefficient correlation and pressure loss correlation proposed by Ganguli *et al.* (1985) are used to predict the air-side heat transfer coefficient and air-side pressure drop over the bundle. For the bare tube bundle under dry operation, the air-side heat transfer coefficient of Khan *et al.* (2006) and the air-side pressure drop correlation of Reuter and Anderson (2016) is used. For the bare tube bundle under wet operation, the mass and heat transfer coefficients proposed by Mizushina *et al.* (1967) are used together with the air-side pressure drop correlation from Reuter and Anderson (2016) to predict the thermal performance. Analysis of both the finned tube bundles and the bare tube bundle are based on a so-called integral method, where the outlet conditions were determined across the bundles from inlet conditions.

Experimental work investigates air flow rate, to avoid high air pressure drop across the bare tube bundle, and the minimum water flow rate to avoid dry-out inside the bare tube bundle are determined. A maximum air mass velocity of $G_{av} = 3$ kg/sm^2 and a minimum water mass velocity of $\Gamma_{dw}/d_o = 1.89$ kg/sm^2 is suggested. Thermocouple attachment methods are investigated for the bare tube bundle under wet operation. It is found that by attaching the thermocouples with 4 zip ties instead of 3, the certainty for measuring water temperature is significantly improved under the suggested air and water flow rates. The air-side pressure drop across the bare tube bundle is influenced by the number of tube rows present, together with air and water flow rates. The pressure drop under wet operation is slightly higher than under dry operation.

The bare tube bundle's dimensions are determined from a parametric study, delivering a bare bundle, 800 mm in both width and height which can boost the cooling systems' performance by between 35 % and 140 % relative to a conventional system, depending on air relative humidity at an ambient dry bulb temperature of 32 ºC. Inlet process medium temperature remains at 38 ºC. The HDWCS can serve as a strong competitor, delivering a significant increase in performance compared to dry coolers especially during hot periods, when the performance of dry only cooling systems are low.

OPSOMMING

Die prestasievermoë van ’n hibriede (droog/nat) verkoelingstelsel (HDNVS) word ondersoek. Dit word gedoen om sodoende ’n verkoelingstelsel te ontwikkel, wat met droëverkoelingstelsels kan meeding en `n beter prestasievermoë gedurende hoë omgewingslugtemperature kan handhaaf. Die beoogde HDNVS bestaan uit 2 dele. Die eerste deel bevat vinbuisbundels wat net droog bedryf word terwyl die tweede deel uit `n skoonbuisbundel bestaan wat droog of nat bedryf kan word.

`n Numeriese voorspellingsprogram is ontwikkel om die prestasie, in terme van die uitlaat-temperature van lug- en prosesmedium te bepaal, gegee die inlaat-toestand van prosesmedium en atmosferiese lug. Korrelasies vanuit die literatuur word soos volg geïmplementeer: vir die vinbuisbundels is die warmteoordragskoëffisiënt en lugkantdrukverlies-korrelasies van Ganguli *et al.* (1985) gebruik. Wanneer die skoonbuisbundel nat bedryf word, is die massa- en warmteoordragskoëffisiënt van Mizushina *et al.* (1967) geïmplementeer en wanneer dit droog bedryf word, die warmteoordragskoëffisiënt van Khan *et al.* (2006). Reuter en Anderson (2016) verskaf die lugkantdrukverlies-korrelasies vir die skoonbuisbundel wanner dit nat of droog bedryf word. Die vinbuis- én skoonbuisbundel is volgens `n sogenaamde integralemetode opgelos, met ander woorde, net die uitlaat-toestande word bereken vanaf die gegewe inlaat-toestande.

Eksperimentele werk sluit in (1) die ondersoek na watervloeipatrone aan die lugkant van die skoonbuisbundel onder kritieke lugvloeitoestande asook uitdroogkolle binne in die skoonbuisbundel, (2) twee hegtingsmetodes vir termokoppels aan skoonbuise, om die meetsekerheid van watertemperatuur te verseker en (3) die effek van aantal buisrye, teenwoordig in die skoonbuisbundel, op die lugdrukval oor die bundel onder verskeie nat- en droëvloeitempo’s. Daar is gevind dat kritieke lugvloeitempo’s tot hoë drukverliese oor die skoonbuisbundel lei en `n maksimum lugmassasnelheid van $G_{av}$ = 3 kg/sm$^2$ word voorgestel, terwyl `n minimum watermassasnelheid van Γ_{dw}/d_o = 1.89 kg/sm^2 voorgestel word om uitdroogkolle in die bundel te vermy. Vir die termokoppels is daar gevind dat indien vier kabel bande gebruik word om die termokoppel aan die skoonbuis te heg, verseker dit die meetpunte bly nat ongeag die lug- en watervloeitempo’s. Laastens is daar gevind dat die lugdrukval oor die skoonbuisbundel, `n sterk funksie van die aantal buisrye is, gevolg deur die lug- en watermassasnelhede. Wanneer die skoonbuisbundel nat bedryf word, is die drukval ietwat hoër as vir droë bedryf.

Vanaf die parameterstudie is daar gevind dat `n vierkantige bundel met `n breedte en hoogte van 800 mm, die prestasievermoë met tussen 35 % en 140 % kan verbeter, in vergelyking met `n konvensionele droëverkoelingstelsel, afhangende van die relatiewe lughumiditeit. Die prestasie is bewerkstellig by `n lugtemperatuur van 32 ºC en prosesmediumtemperatuur van 38 ºC. Vanuit die studie is daar bevind dat die HDNVS as `n sterk mededinger kan dien vir droëverkoelingstelsels en die vermoë het om `n wesenlike impak te maak op verkoelingsprestasie gedurende

tydperke van hoë lugtemperature – wanneer die verkoelingsvermoë van droëverkoelers drasties afneem.

ACKNOWLEDGEMENTS

I would like to thank the following people and entities for their continued support and valuable input:

- The LORD almighty, whom I have come to know personally and whom without, all my works and effort are nullified. To Him be all the glory forever, Amen.
- Department of Mechanical Engineering for their financial support and providing me with this opportunity to further my engineering skills and abilities.
- Prof. Hanno Reuter, for his ongoing technical guidance, mentorship and support.
- Dr. Mike Owen for his willingness to oversee the final stages of this thesis.
- Mr. Cobus Zietsman, Julian Stanfliet and the rest of the workshop staff for their help building the experiments.
- My parents, Andries and Gerda Graaff, for their unconditional love, financial and emotional support.
- Otto Scheffler, Matthys du Toit and Jean-Gerard de la Bat, for their friendship and support during late nights and long weekends.

CONTENTS

LIST OF TABLES

LIST OF FIGURES

NOMENCLATURE

Symbols

A	Area	[m^2]
C	Discharge coefficient	-
c_p	Specific heat at constant pressure	[J/kgK]
c_v	Specific heat at constant volume	[J/kgK]
D	Diffusion coefficient	[m^2/s]
d	Diameter	[m]
e	Fin effectiveness	-
F_r	Relaxation factor	-
f	Friction factor	-
G	Mass velocity	[kg/$sm^{2]}$
H	Height	[m]
h	Heat transfer coefficient	[W/m^2K]
h_d	Mass transfer coefficient	[kg/sm^2]
i	Enthalpy	[J/kg]
i_{fg}	Latent heat	[J/kg]
K	Loss coefficient	-
k	Thermal conductivity	[W/mK]
L	Length	[m]
m	Mass flow rate	[kg/s]
n	Quantity	-
P	Pitch, power	[W]
p	Pressure	[Pa]

Q	Heat transfer rate	[W]
R	Thermal resistance	[K/W]
T	Temperature	[ºC or K]
t	Thickness	[m]
U	Total heat transfer coefficient	[W/m^{2}K]
V	Volumetric flow rate	[m^3/s]
W	Width	[m]
w	Humidity ratio	[kg/kg d.a.]
x	Distance	[m]
y	Distance	[m]
z	Distance	[m]

Greek letters

Γ	Water mass flow rate over halve a tube side per unit length	[kg/sm]
Δ	Difference	-
Ω	Electric resistance	[ohm]
η	fin efficiency	-
μ	Dynamic viscosity	[kg/sm]
ρ	Density, kg/m^3	[kg/m^3]

Subscripts

a	Ambient, air, air-side
abs	Absolute
atm	Atmosphere

av	air vapour mixture
b	Bare, bundle
c	Cross section, convection, critical
d	Diffusion, mass transfer
db	Dry bulb
de	Drift eliminator
dry	Dry operation
dw	Deluge water
f	Fin
i	Internal, inlet, initial
l	Log, longitudinal
m	Mass, mean, mixture
meas	Measured
n	Nozzle
o	Outlet, outside
p	Process medium
r	Root, row
rec	Recovery
ref	Reference
sat	Saturated
sp	Spray
sys	System
t	Tube, Thermal, transverse
tb	bare tube

tr	Transverse
v	Vapour
w	Water, wet
wb	Wet-bulb
wds	Water distribution system
wet	Wet operation

Dimensionless numbers

NTU	Number of transfer units
Nu	Nusselt number, (hd/k) for a tube
Pr	Prandtl number, ($\mu c_p/k$)
Re	Reynolds number, ($md/A_c\mu$)
Sc	Schmidt number, ($\mu/(\rho D$)
Sh	Sherwood number, ($h_D L/D$)
Le	Lewis number, (Sc/Pr)

Abbreviations

ACC	Air-cooled condenser
HDWCS	Hybrid (dry / wet) cooling system
HDWD	Hybrid (dry / wet) dephlegmator
HT	Heat transfer
RH	Relative humidity
RTD	Reference thermocouple device
VSD	Variable speed drive

WDS	Water distribution system

1. INTRODUCTION

The performance of a hybrid (dry/wet) cooling system (HDWCS) is investigated. This is done by determining the heat transfer rate and outlet temperatures and/or enthalpy of the working fluids based on a set of known inlet parameters. A one-dimensional numerical model is developed to evaluate the performance of a standard air-cooled heat exchanger with and without a second stage delugeable bare tube bundle. A small-scale bare tube bundle is designed, built and tested to investigate the effects of air and deluge water flow rate on pressure drop and on the flow patterns by means of digital photography. Thermocouple placement for the accurate measurement of deluge water temperature is investigated, essential for determining the transfer characteristics from test data.

1.1 Background

Cooling systems are used to reject waste heat from a process medium to the environment – atmospheric air or natural water bodies. Small scale cooling systems are found all around us, for example the radiator in motor cars or refrigerators and domestic air-conditioning units. Large scale cooling systems are found in industrial processes, chemical, petrochemical and power plants as well as heating, ventilation and air-conditioning (HVAC) systems. This project focuses on air cooling systems for the HVAC industry.

1.1.1 Wet, dry and combined cooling systems

Figure 1.1 illustrates the different categories into which air-cooled systems are usually classified. The two primary air-cooled classifications, are wet (sensible and latent cooling) and dry (sensible only) cooling. Wet and dry systems can be combined in different ways to realise the benefits of the respective systems while reducing their primary disadvantages. These systems are referred to as combined systems. The first cooling systems originated from once through systems (Oosthuizen, 1995), where natural water bodies are used as heat sinks. By redirecting water through a heat exchanger, heat is rejected from a hot process fluid to a cold water body without air cooling taking place. The heating of natural water bodies have adverse effects on the biological systems dependant on them (Kröger, 2004). Evaporative cooling systems are developed to mitigate these adverse effects, once through systems have on natural water bodies.

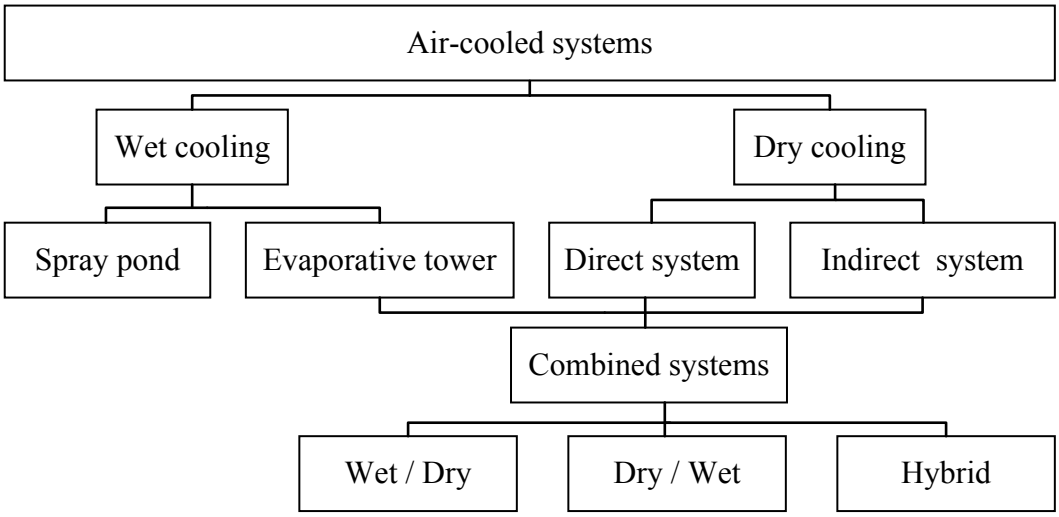

Figure 1.1: Classification of air-cooled systems

Evaporative cooling systems are systems where sensible and latent heat is transferred by exposing hot water directly to the atmospheric air. Sensible heat transfer takes place due to the difference between the water temperature and dry bulb air temperature while latent heat transfer takes place due to mass transfer, resulting from a concentration gradient of vapour in the air - at the water surface and that of the cooling air stream. Although a natural water resource is required to supply make-up water, no heat is rejected to it as the water in an evaporation system is recirculated instead of rejected to the natural water resource.

Evaporative cooling systems discharge large quantities of water vapour into the atmosphere from a concentrated source which make them dependant on water resources to make up these losses. Large quantities of water vapour in the atmosphere leads to plumes and visibility hazards, ice formations in cold conditions and pollution of other water resources through precipitation (Oosthuizen, Kröger and Heyns (2008)). Dry cooling systems were developed for arid regions and to mitigate challenges faced with evaporative cooling systems.

Dry cooling systems reject heat from a process medium to surrounding air through sensible heat transfer (Kröger, 2004). This is achieved by forcing atmospheric air over finned tube bundles, carrying a hot process medium. Sensible heat is thereby transferred from the process medium to the atmospheric air via forced convection.

Dry cooling systems are independent of natural water resources. This makes them the preferred cooling system in arid or other water constrained regions. Due to the low heat capacity of air and sensitivity towards high ambient temperatures, dry cooling systems are typically large structures which necessitate high capital costs and produce low efficiencies during hot days. Lower plant efficiencies results in increased air pollution due to more fossil fuel being burnt. Combined systems are thus developed to draw on the advantages of both evaporative and dry cooling systems.

Combined systems consist of a primary cooling system (dry or wet) with an opposite auxiliary system. For instance, a dry/wet cooling system is mainly a dry system with an evaporative (wet) system as an auxiliary to boost performance when required. A wet/dry cooling system consists of a primary evaporative cooler with a dry cooling system as auxiliary which is used to realise plume abatement. With combined systems, more environmentally friendly systems are designed. Figure 1.2 depicts a dry/wet combined system, with a series water flow configuration, originally presented by Oosthuizen (1995).

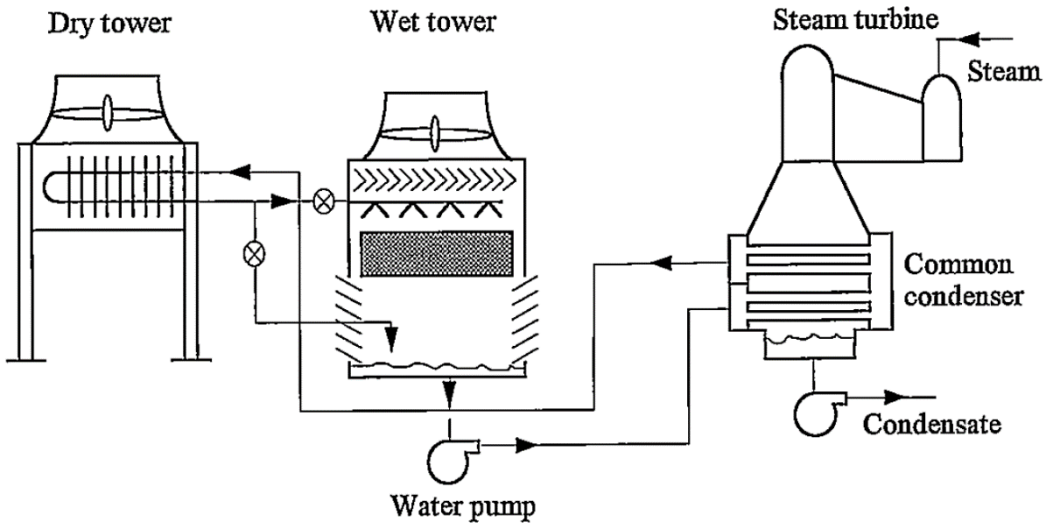

Figure 1.2: Dry/wet combined system with series water flow. (Oosthuizen, 1995)

The dry tower initially cools down the water before passing some of the cooled water through an evaporative cooling system where it is further cooled. The rest of the water is directly fed into the water basin where it is pumped back to the steam surface condenser.

Figure 1.3 depicts the wet/dry cooling system, with parallel steam flow, originally presented in Oosthuizen (1995).This wet/dry cooling system divides the steam from turbines between a direct dry cooling system and a steam surface condenser. Steam in the dry cooling system is directly condensed by drawing air over the finned tubes. Cooling water in the surface condenser, heated by the condensing steam, is cooled in an evaporative cooling system. Condensed steam from the dry tower and surface condenser is pumped back to the process to complete the cycle.

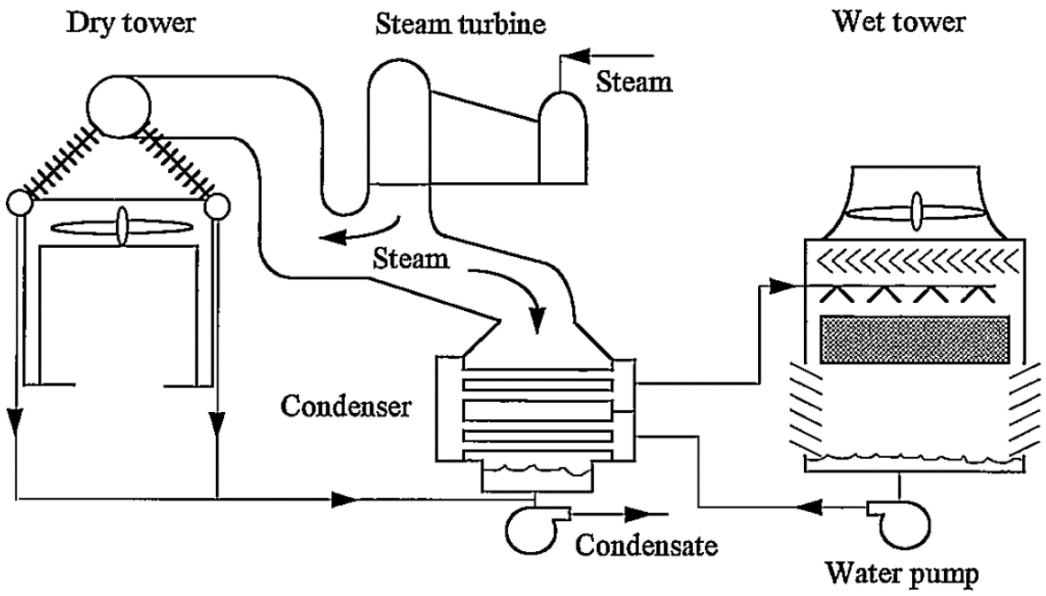

Figure 1.3: Wet/dry cooling system with parallel steam flow. (Oosthuizen, 1995)

Combined systems are rarely fully utilised. A cooling system functions optimally when sized according to a given work load. With combined systems, multiple work points exist for both systems making it difficult to size optimally. For the combined system to function optimally each subsystem has to function optimally.

1.1.2 Hybrid cooling systems

Hybrid cooling systems are combined systems which are housed in a single structure. Hybrid systems are more compact and require less floor area compared to combined systems (Anderson, 2014). Numerous combinations exist, making hybrid systems flexible, application specific cooling systems (Heyns, 2008).

Hybrid cooling systems are either classified as combined (consisting of individual wet and dry sections) systems or delugeable (one section operated wet or dry) systems. Further, hybrid systems are classified by the air and water travel paths that occur in parallel, series or a mixture of parallel and series. The classification of hybrid cooling systems is presented in Figure 1.5

A parallel flow system is one where the inlet condition of the fluid to each section is identical. For instance in a parallel air flow system, the inlet air conditions for the wet and dry sections of the hybrid system are the same. A series flow system is one where the working fluid moves sequentially through the hybrid system. For instance, a series water flow system is one where the water outlet temperature of one section is the inlet temperature to the following section (Heyns, 2008).

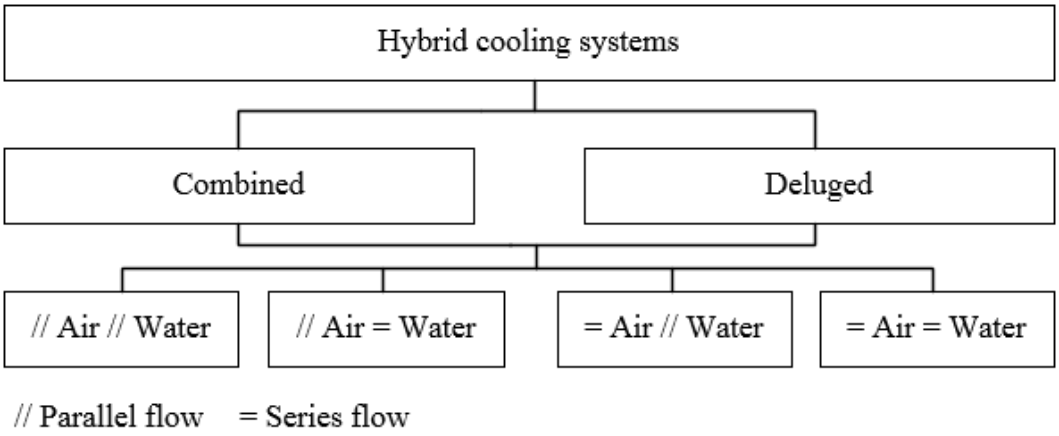

Figure 1.5: Classification of hybrid cooling systems

An example of a hybrid delugeable cooling system, currently available in industry, is presented in Figure 1.4. This hybrid system consists of finned tube bundles which can be operated either dry or wet. A cathodic dip paint process enhances resistance to fouling and corrosion, commonly associated with wet finned tube bundles. Air travels over the outside of the finned tube bundles while the process medium travels through the finned tube. The hybrid system in Figure 1.4 functions as a dry cooling system during cold ambient periods. During hot ambient periods or periods requiring a boost in performance, the finned tube bundles are deluged with water enabling the system to function as an evaporative system. This gives it the advantage of less water consumption compared to an evaporative cooler and the ability to maintain the required performance during unfavourable conditions for dry cooling.

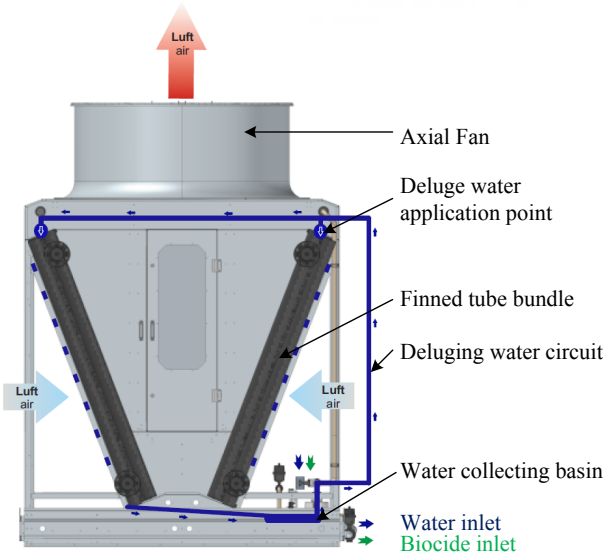

Figure 1.4: Current hybrid cooling system from industry. (Thermofin, 2013)

This hybrid system however requires a costly chemical process to protect the fin surfaces from corrosion and fouling. The system presented and evaluated in this study mitigates this disadvantage by adding a separate bare tube bundle to operate wet or dry, keeping the finned tube bundle dry during operation and thus eliminating the need for a costly tube treatment process.

Hybrid (dry / wet) cooling system (HDWCS)

The HDWCS, presented in Figure 1.6, is a hybrid air-cooled system that consists of two stages, connected in series on the process medium side and in parallel on the air-side. The first stage, which consists of two finned tube bundles with horizontal tubes, operates only dry while the second stage operates wet or dry depending on ambient conditions and performance requirements.

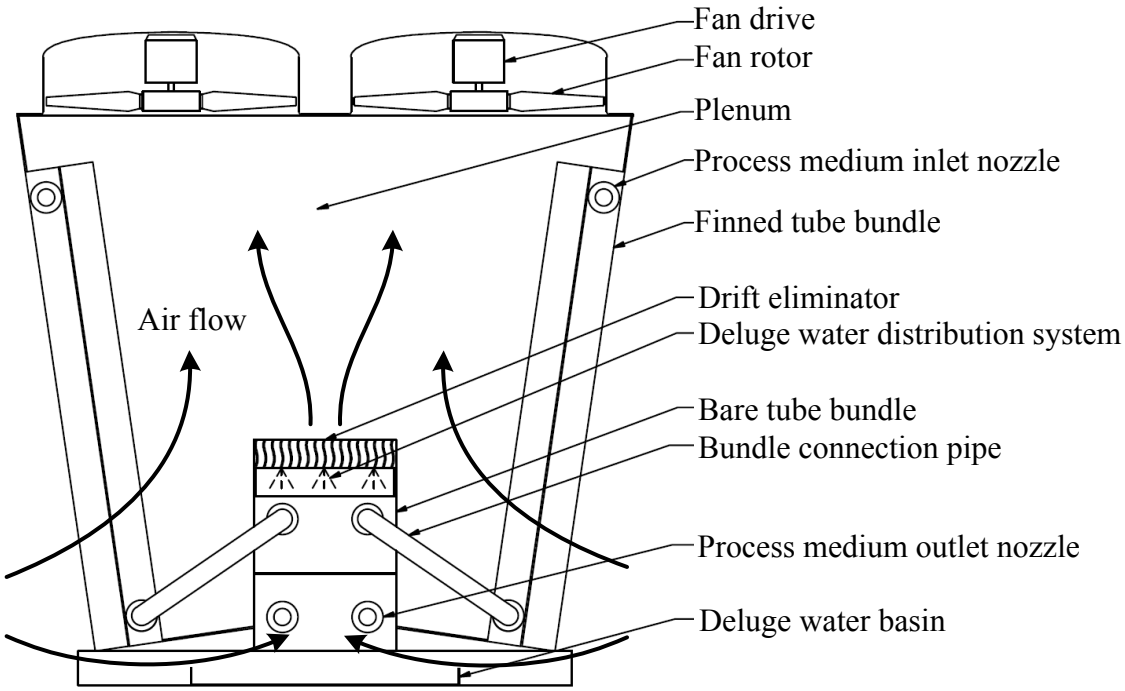

Figure 1.6: Schematic of the HDWCS

The second stage, a delugeable bare tube bundle has a water distribution system and drift eliminator above, and a water collection basin for water recirculation below. Induced draft axial fans are located on top of the HDWCS.

Bare tube bundles are easier to clean compared to finned tubes and are less susceptible to bio-fouling and corrosion. This second stage system can be retro fitted to existing dry cooled systems with minor modifications.

The process medium enters the HDWCS at the process medium inlet nozzle where it passes through the finned tube bundles (first stage). Cooling in the first stage is achieved by drawing air over the finned tube bundles thereby transferring sensible

heat from the process fluid to atmospheric air by forced convection and conduction through the tube walls and fins.

The bundle connection pipe links the finned tube bundles with the bare tube bundle (second stage) that is operated either dry or wet. Under wet operation, the bare tube bundle is deluged with water and operates as an evaporative cooler. Cooling is achieved by sensible heat transfer when operating dry, or by a combination of sensible and latent heat transfer when operating wet. The cooled process medium leaves the HDWCS at the process medium outlet nozzle.

By configuring the HDWCS in this arrangement, air enters both stages at the ambient temperature and humidity. Wet cooling is utilised in the second stage when high ambient temperatures render dry cooling less effective or when winds reduce the fan performance. Wet cooling can also be used under favourable dry cooling conditions if desired.

The novelty of this cooling system is that it combines a dry and wet cooling system into one compact unit. It utilises the environmental advantages of dry cooling together with the cooling effectiveness of wet cooling to offer a robust and versatile cooling system.

1.1.3 Context

This study stems from research done at Stellenbosch University into the workings of hybrid coolers by Heyns (2008), Owen (2013), and Anderson (2014).

Heyns (2008) investigated a hybrid reflux condenser design, called the hybrid (dry/wet) dephlegmator (HDWD), for application in large air-cooled steam condensers (ACCs). The HDWD aims to replace the standard all-dry reflux condenser in ACCs. He proposed a forced draft design that could easily be retrofitted to existing condenser infrastructure. Figure 1.7 displays the forced draft HDWD suggested by Heyns (2008).

Heyns (2008) did experimental tests on a bare tube bundle with an outer tube diameter, d_o = 38.1 mm, eight tubes per row and 15 tube rows, spaced with a $2d_o$ triangular pitch. He developed correlations for the mass transfer, heat transfer and air-side pressure drop coefficients in his bundle and implemented them in an analytical performance model. In his performance model, Heyns (2008) ignored steam-side pressure drop in the bare tube bundle.

Heyns (2008) found that the mass transfer and air-side pressure drop coefficients are functions of the air and deluge water mass velocities while the heat transfer coefficient is a function of these velocities as well as the deluge water temperature.

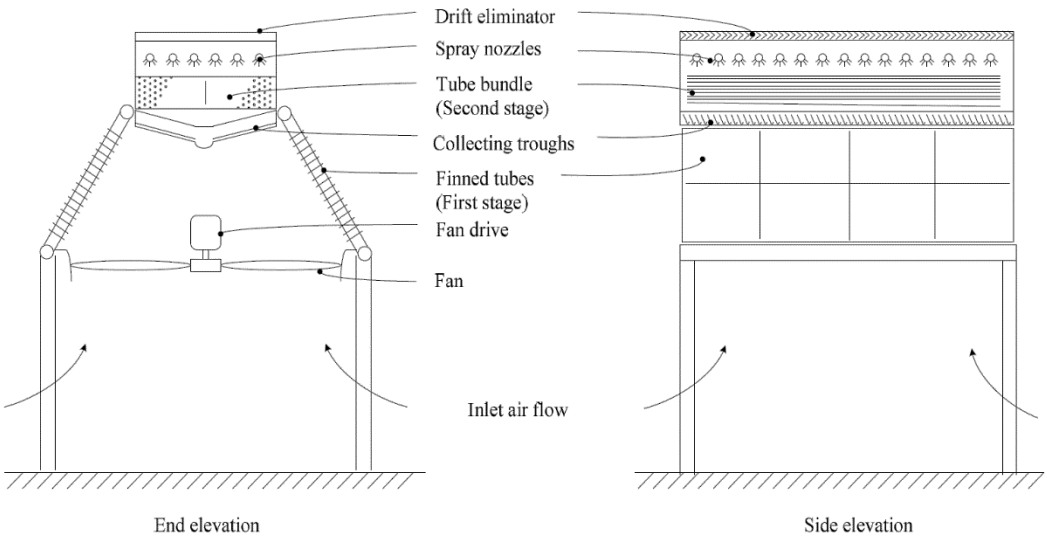

Figure 1.7: Forced draft hybrid (dry/wet) dephlegmator (HDWD).

(Heyns, 2008)

The correlations suggested by Mizushina *et al*. (1967) for the mass and heat transfer coefficients agreed well with correlations from Heyns' experimental results. The correlations of Heyns (2008) are only applicable to bare tube bundles with similar geometry and tube size as used in his study.

Apart from investigating steam side pressure losses in ACCs, Owen (2013) refined the second stage design of the HDWD proposed by Heyns (2008). Further, Owen investigated the effect of tube outer diameter, number of tube rows, number of vapour passes and number of tube rows per vapour pass on turbine performance for the HDWD second stage bare tube bundle.

Owen (2013) found that the forced draft design would lead to internal flooding in the first stage counter-flow finned tube bundles. He proposed an induced draft design with co-current vapour/condensate flow in the first stage to eliminate flooding. He recommends a bare tube diameter of d_o = 19 mm, with 25 tube rows and three passes. The first pass would have 20 tube rows, the second pass 4 tube rows and the final pass, a single tube row. With this configuration minimal flooding is expected together with no vapour backflow in the bare tube bundle. Figure 1.8 presents the induced draft HDWD design.

Owen (2013) recommended further experimental investigations into the performance of the bare tube bundle in order to validate the predicted performance. No reliable air-side pressure drop correlations could be found in literature for a bare tube bundle under wet operation.

Anderson (2014) focused on the bare tube bundle design recommended by Owen (2013) and conducted experimental investigations to determine mass and heat transfer correlations between the deluge water and air, together with air-side

pressure loss correlations. A prototype bare tube bundle with the recommended dimensions was designed and tested at Stellenbosch University. Hot water at 50 ºC was used instead of steam as the process fluid.

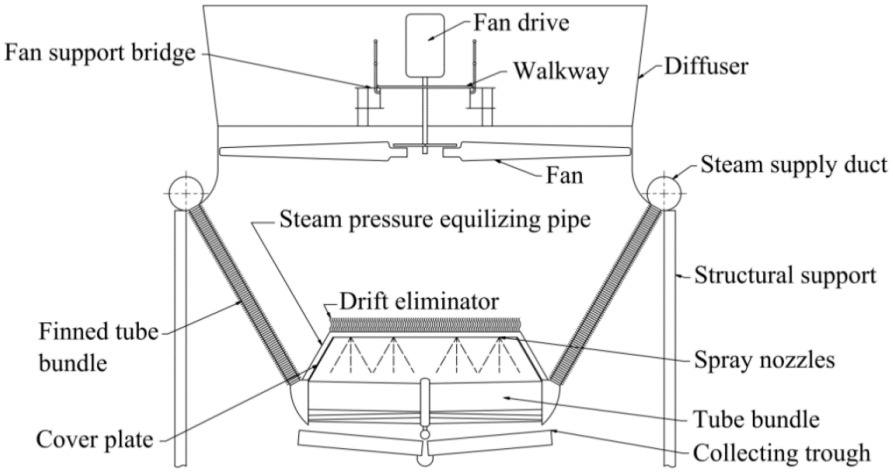

Figure 1.8: Induced hybrid (dry/wet) dephlegmator (HDWD). (Anderson, 2014)

Anderson (2014) found good agreement between the correlations developed from his experimental data and those suggested by Mizushina *et al*. (1967) for the mass and heat transfer coefficients. He concluded that the bare tube bundle of the HDWD could deliver between 215 % and 595 % increase in performance under wet operation compared to dry operation.

The air-side pressure drop correlation for wet operation determined by Anderson (2014) is only applicable to his bundle dimensions and geometry layout. Uncertainty around the measuring techniques of the deluge water temperature was found. Visual investigations on a bare tube bundle are required to gain a better understanding of heat transfer mechanisms and pressure losses.

1.2 Scope

This study investigates the possibility of incorporating the principles developed with the HDWD into the HDWCS in order to evaluate the performance under wet and dry operation.

This study incorporates the test data of Anderson (2014) where process water was cooled by a prototype bare tube bundle. Deluge water flow tests are conducted under different flow conditions. Uncertainties surrounding the sharp rise in air-side pressure drop under high air mass velocities and bundle wetting under low water mass velocities, as mentioned in Anderson (2014), are investigated. A concept of the HDWCS is presented and its performance is compared to current conventional dry cooling systems.

1.3 Objectives

The objectives of this study are to:

1. Present a system concept description of the HDWCS.
2. Review literature relating to hybrid cooling systems.
3. Develop a numerical performance prediction model for the HDWCS concept.
4. Experimentally investigate air-side pressure drop under high air mass velocities and bundle wetting.
5. Perform a parametric study on the HDWCS using the as-developed numerical performance prediction model.

1.4 Motivation

This study is a continuation of research done at Stellenbosch University on the topic of hybrid (dry/wet) cooling to find more environmentally friendly solutions for cooling with reduced life-cycle costs.

The proposed HDWCS is expected to require less floor area and can deliver better performance during high ambient temperatures with potentially lower life cycle costs compared to a wet only or dry only cooling system.

1.5 Thesis overview

Chapter 1 introduced the topic of wet, dry and hybrid cooling systems. The scope of the project was outlined together with the objectives and motivation for undertaking of this research.

Chapter 2 presents literature on the subjects of evaporative cooling, dry cooling, performance characteristics of bare and finned tube bundles and novel cooling system technologies.

Chapter 3 presents the theory used to develop a performance prediction model for the HDWCS. The calculation procedure is presented with formulas for the first and second stages of the HDWCS. Two performance prediction models for the bare tube bundle are developed. The predicted performance is compared to that obtained with correlations from literature. Recommendations are made on which correlations are to be used with a performance prediction model for the HDWCS.

Chapter 4 presents the experimental work conducted in this study.

The first experiment examines the development of the deluge water film visually on a bundle section similar to that of Anderson (2014) under different deluge water and air flow rates. Possible dry-out sections in the bundle are identified. Recommendations on the preferred flow rates for deluge water and air is given.

The second experiment presents two methods for attaching the thermocouple to the bare tubes to measure deluge water temperature and recommends one of the designs to incorporate when thermal tests are done on full scale prototypes.

The third experiment modifies the experimental apparatus to investigate the pressure drop over the bare tube bundle under different deluge water and air flow rates as well as under dry operation. Tube rows are sequentially removed to obtain pressure drop correlations as functions of the amount of tube rows present.

Chapter 5 presents a system description of the HDWCS together with a numerical model for predicting the performance. A parametric study is presented. The predicted performance of the HDWCS is compared to current dry cooled systems and savings in terms of area and performance are presented.

Chapter 6 provides the conclusions and recommendations for each of the objectives set out in Chapter 1. New uncertainties that arose from this study are presented together with recommendations from the observations made.

2. LITERATURE REVIEW

2.1 Introduction

This chapter presents literature on current research into novel cooling systems, followed by the performance modelling and characteristics of finned tube and bare tube bundles. Further, certain aspects of a bare tube bundle under wet operation are explored before a conclusion is presented.

2.2 Current research on novel cooling systems

Novel cooling systems and methods to reduce air-cooled systems' energy consumption or increase their efficiency are presented in an updated overview concerning refrigeration systems by Harby *et al*. (2016). They present 15 studies in which evaporative condensers are incorporated as components into air-cooled systems to either enhance the system's performance or reduce its work requirements. Ways of doing this includs (1) replacing air-cooled condensers with evaporative condensers, (2) precooling of inlet air by either adiabatic spray systems or by adding an upstream evaporator or (3) making use of heat storage facilities.

By replacing air-cooled condensers with evaporative cooled condensers a gain in cooling performance of 14 % to 113% is achieved and a reduction in mechanical energy of 15 % to 58 % is observed (Harby *et al*., 2016).

Vakiloroaya *et al*. (2014) presents a review of different strategies to save energy in the HVAC industry, focusing mainly on the building environment. They compare 11 different cooling systems in order to find an optimal combination of different system components to deliver maximum performance at minimum cost. In order to achieve high economic efficiency, systems need to use current components in novel configurations rather than developing novel components. Efficient systems depend on several factors including climate, cost, available energy sources and the purposes for which the buildings are used. They consider a wide variety of cooling systems although most cooling systems includs an evaporative cooler. No specific or multiple stage cooling systems similar to the HDWCS are considered.

Popli *et al*. (2014) investigates deluge cooling of inclined finned tube heat exchangers. Their experimental study determines the heat transfer rate and air side pressure drop of three finned tube heat exchangers, where the effect of fin spacing and adding a hydrophobic coating under wet and dry conditions are investigated for a vertical and an inclined (at 70º) finned tube bundle.

Popli *et al*. found that deluge cooling increases the heat transfer capacity by a factor of 2.78 and the air-side pressure drop by a factor 2.28 compared to dry cooling. A fin spacing of 2.4 mm achieved 2 % to 30 % gain in heat transfer performance compared to a 3 mm fin spacing under wet and dry conditions. The hydrophobic coating deliveres a 5 % to 30 % gain in heat transfer performance compared to an

uncoated bundle when under wet operation. This could be due to smaller drop formation which led to an increased evaporation surface area. The hydrophobic coating has no significant impact dry cooling performance or on the pressure drop across the finned tube bundle.

Popli *et al*. does not elaborate on ways to enhance dry operation bundle efficiency without adding additional flow resistances, for instance spacing the fins closer together, as the hydrophobic coating only increased heat transfer performance under wet operation.

In current research, no literature is found on hybrid systems similar to that considered by Owen (2013) and Anderson (2014). From the above studies it is evident that there is a lack of experimental research into industrial systems that reside over multiple stages and consist of delugeable heat transfer surfaces. This study aims to use available bundle designs and arrange the components in a unique way to deliver a cooling system that can be incorporated into the HVAC industry on an industrial scale.

2.3 Performance models and characteristics of air-cooled heat exchangers

Various performance predicting models for cooling systems are found in literature. Different models are used depending on the required degree of accuracy coupled with correlations for mass transfer, heat transfer and air-side pressure loss coefficients. Experimental data is used to validate performance models and determine correlations for mass transfer (under wet operation), heat transfer and air-side pressure drop coefficients.

2.3.1 Finned tube bundles

Finned tubes are available in different shapes and sizes with fins protruding from the sides, and may be round, elliptical, flattened or otherwise streamlined to reduce their air-side flow resistance. For this study round finned tubes, with a coiled fin, are used in the first stage of the HDWCS. Kröger (2004) found that round tubes perform better compared to elliptical tubes when the process medium is at a positive pressure compared to the ambient environment.

Finned tube bundles under dry operation are commonly modelled as whole bundles where the outlet conditions are determined based on the inlet conditions and heat transfer coefficients.

The general heat transfer equation for a tube bundle can be defined as,

$$Q = F_T U_a A_a \Delta T_{lm} \tag{2.3.1}$$

where F_T is a correction factor for a cross flow heat exchanger and defined by Kröger (2004) as:

$$F_T = 1 - \sum_{i=1}^{4} \sum_{k=1}^{4} a_{i,k}(1-\phi_3)^k \sin\left\{2i\left[\arctan(\phi_1/\phi_2)\right]\right\} \tag{2.3.2}$$

The dimensionless temperature changes may be defined as:

$$\phi_1 = \frac{T_{pi}-T_{po}}{T_{pi}-T_{ai}}$$

$$\phi_2 = \frac{T_{ao}-T_{ai}}{T_{pi}-T_{ai}}$$

$$\phi_3 = \frac{\phi_1-\phi_2}{ln\left[(\phi_1-\phi_2)/(1-\phi_1)\right]}$$

where the constants in equation. (2.3.2) are given in Table 2.1.

Table 2.1: Constants for equation (2.3.2)

$a_{i,k}$	$i = 1$	2	3	4
$k = 1$	-0.339	0.0277	0.179	-0.0199
2	2.38	-0.0999	-1.21	0.04
3	-5.26	0.0904	2.62	0.0494
4	3.9	-0.000845	-1.81	-0.0981

The log mean temperature difference (LMTD) is as follows:

$$\Delta T_{lm} = \frac{T_{po}-T_{ai}-(T_{pi}-T_{ao})}{ln\left(\frac{T_{po}-T_{ai}}{T_{pi}-T_{ao}}\right)} \tag{2.3.3}$$

The overall heat transfer coefficient is determined from the respective heat transfer coefficients for internal and external forced convection found in literature as expressed in equation (2.3.4).

$$U_a = \left[\frac{d_o}{d_i h_p} + \frac{d_o ln\left(\frac{d_o}{d_i}\right)}{2k_t} + \frac{1}{h_a e_f}\right]^{-1} \tag{2.3.4}$$

The first term in equation (2.3.4) represents the internal convection heat transfer. The second term represents the conduction heat transfer through the tube wall, and the third term represents the heat transfer on the outside of the tube (combined convection and conduction under wet operation). For the internal convection heat transfer coefficient, Kröger (2004) recommends the equation of Pethukov (1970) in conjunction with equation (2.3.6) to calculate the internal wall friction.

$$h_p = \frac{0.125 f_D Re Pr}{1.07+12.7(0.125 f_D)^{0.5}\left(Pr^{0.667}-1\right)} \frac{k_p}{d_i} \tag{2.3.5}$$

$$f_D = \left[1.82log_{10}(Re) - 1.64\right]^{-2} \tag{2.3.6}$$

Kröger (2004) presented various air-side heat transfer and pressure drop correlations for finned tube bundles based on various bundle parameters. Ackers (2012) investigated finned tube bundle air-side heat transfer and pressure loss coefficients which consisted of validating heat transfer coefficient correlations from literature and showed that the heat transfer and pressure drop correlations of Ganguli *et al*. (1985) correlated his experimental data best. The external heat transfer coefficient correlation for a finned bundle with three or more rows, under dry operation, is given by Ganguli *et al*. (1985) as,

$$h_a = 0.38 Re_c^{0.6} Pr^{0.333} (A/A_r)^{-0.15}\, k/d_r \tag{2.3.7}$$

where $Re_c = \frac{G_c d_r}{\mu}$.

The air-side pressure drop correlation given by Ganguli *et al*. (1985) is,

$$\Delta p_{fb} = \frac{2n_r G_c^2}{\rho_{avm}} \left\{ 1 + \frac{2exp\left[-\frac{\left(P_t - d_f\right)}{4d_r}\right]}{1 + \frac{\left(P_t - d_f\right)}{d_r}} \right\} \left\{ 0.021 + \frac{13.6\left(d_f - d_r\right)}{Re_c\left(P_f - t_f\right)} + 0.25246 \left[\frac{d_f - d_r}{Re_c\left(P_f - t_f\right)}\right]^{0.2} \right\} \tag{2.3.8}$$

and is applicable for,

$$2.5 < \frac{d_f - d_r}{2\left(P_f - t_f\right)} < 12.5 .$$

2.3.2 Bare tube bundles: Dry operation

For dry performance of bare tube bundles, numerous correlations for the Nusselt number (dimensionless heat transfer coefficient) are found in literature like those proposed by Zukauskas (1987), Khan *et al*. (2006) and Reuter and Anderson (2016). Gaddis and Gnielinski (1985) does a thorough study on tube bundles in crossflow and presents pressure drop correlations for a wide range of Reynolds numbers.

The bare tube bundle under dry operation is modelled in a similar fashion to the finned tube bundle, with the appropriate heat transfer coefficient correlations.

Anderson (2014) found that the correlation of Khan *et al*. (2006) predicts the heat transfer coefficient he measured across his bare tube bundle to within 5 %. Due to

the similar layout of the bare tube bundle, the air-side pressure loss coefficient suggested by Reuter and Anderson (2016) is employed in the performance prediction model to predict the air-side pressure drop for dry operation.

The air-side heat transfer coefficient correlation proposed by Khan *et al*. (2006) is given as,

$$h_a = \frac{k_{avm}}{d_o} \frac{0.61\left(\frac{P_t}{d_o}\right)^{0.091}\left(\frac{P_l}{d_o}\right)^{0.053}}{1-2exp\left(-1.09\,\frac{P_l}{d_o}\right)} Re_D^{0.5}\, Pr_{avm}^{1/3} \tag{2.3.9}$$

where $Re_D = \frac{m_{avm} d_o}{A_c \mu_{avm}}$

The pressure loss correlation proposed by Reuter and Anderson (2016) for dry operation is,

$$K_{tb(d)} = 14.5049 Re_D^{-0.04678} \tag{2.3.10}$$

and valid over $2 \cdot 10^3 < Re_D < 10^4$

Figure 2.1 presents (a) different heat transfer equations for bare tube bundles in terms of the Nusselt number and (b) different air-side pressure drops under dry operation.

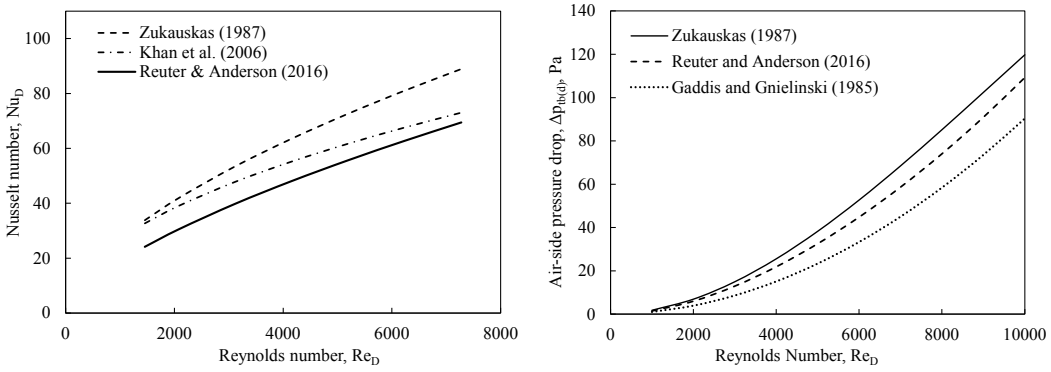

(a) (b)

Figure 2.1: Dry operation (a) Nusselt Number and (b) air-side pressure drop

From Figure 2.1 (a), the correlations for the heat transfer coefficient proposed by Khan et al. (2006) fall between that proposed by Zukauskas (1987) and Reuter and Anderson (2016). The air-side pressure drop correlations presented in Figure 2.1 (b), show that the correlation proposed by Reuter and Anderson (2016) fall between the other two.

2.3.3 Bare tube bundles: Wet operation

Bare tube bundles, under wet operation, are commonly modelled using an integral method. Kröger (2004) noted that the effectiveness-NTU (ε-NTU) method has a

simple calculation procedure, employing an enthalpy potential difference between the air at the deluge water film and the air stream as derived by Merkel (1925). Numerical models, which solve more than two differential equations, were presented by Poppe and Rögener (1984), Papaefthimiou *et al*. (2012) and Zheng *et al*. (2012).

Dreyer (1988) presents an extensive literature review on modelling of evaporative coolers and condensers over the period of 1928 to 1986. He found that Parker and Treybal (1961) presents the first accurate heat transfer performance model for deluged bare tube bundles.

Since then various integral models are presented in literature. Many articles fail to define the mass transfer and heat transfer correlations explicitly. Dreyer concludes at the time of his study, that none of the reviewed models are established as the accepted standard.

Discretised numerical models present an alternative to integral models. In a discretised model, a row by row solution is obtained which has the advantage of analysing the bundle on a spatial level by solving the (1) process water temperature, (2) the deluge water temperature and (3) air enthalpy at any location in the bundle.

Dreyer (1988) presents a row discretised counter flow model for a bare tube bundle where the temperature profile of the deluge water is solved through the height of the bundle. He found that this model is very sensitive to the deluge water outlet temperature and suggested that an integral model may be used without serious loss of accuracy.

Mizushina *et al*. (1967) investigates the performance of bare tube bundles, of various tube diameters, and presents correlations for the mass transfer and heat transfer coefficients by employing an integral method for analysing experimental data.

Three bare tube bundles, each with a different tube diameter namely, 12.7 mm, 19 mm and 40 mm were tested by Mizushina *et al*. (1967) to determine the transfer coefficients. The bundles consisted of six tubes per row with eight and twelve tube rows. They found small variations in the deluge water temperature (< 2 ºC) across the height of the bundle. Mizushina *et al* (1967) gives a correlation for the mass transfer coefficient as a function of the air and deluge water Reynolds numbers as well as the tube outside diameter (d_o),

$$h_d = 5.5439 \times 10^{-8} Re_{avm}{}^{0.9} Re_{dwm}{}^{0.15} d_o{}^{-1.6} \qquad (2.3.11)$$

where the air Reynolds number is defined with an applicable range by,

$$1.2 \times 10^3 < Re_{avm} = \frac{m_{avm} d_o}{A_c \mu_{avm}} < 1.4 \times 10^4$$

and the deluge water Reynolds number with applicable range from,

$$50 < Re_{dwm} = \frac{m_{dwm} d_o}{A_c \mu_{dwm}} < 280$$

Their heat transfer coefficient under wet operation is presented as a power function of the deluge water flow rate and given by,

$$h_{dw} = 2102.9 \left(\frac{\Gamma_{dw}}{d_o}\right)^{1/3} \tag{2.3.12}$$

where Γ_{dw}/d_o is the deluge water mass velocity or mass flux and defined as,

$$\frac{\Gamma_{dw}}{d_o} = \frac{m_{dw}}{2 n_{tr} P_t L} \tag{2.3.13}$$

and applicable over $0.2 < \Gamma_{dw}/d_o < 5.5$ kg/sm^2 and $1.2 \times 10^3 < Re_{avm} < 1.4 \times 10^4$.

Anderson (2014) confirms the observations made by Mizushina *et al*. (1967) regarding the small change in deluge water temperature and presented an updated literature review on evaporative and dry cooling of bare tube bundles. Table 2.2 presents details of the various studies considered by him including details of his study.

Table 2.2: Summary of bundle characteristics found in literature

Author	Parker and Treybal (1961)	Mizushina *et al.* (1967)	Nitsu *et al.* (1969)	Finlay and Harris (1984)	Hasan and Sirén (2002)	Papaefthimiou *et al.* (2012)	Anderson (2014)
d_i [mm]	15.8	-	-	15.0	-	15.0	15.8
d_o [mm]	19.0	12.7, 19.1 and 40.0	16.0	19.1	12.0	19.1	19.1
n_{tr}	6	6	-	31	19	31	39
n_r	10	8 and 12	-	16	12	16	25
P_t	$2d_o$	$2d_o$	$2.34d_o$	$1.5d_o$	$1.67d_o$	$1.5d_o$	$2d_o$
P_l	-	-	$2.38d_o$	-	$5d_o$	-	-
Layout	Tri	Tri	Stag	Tri	Stag	Tri	Tri
Analysis	Num. Int.	ε-NTU	-	Num. Int.	Num. Int.	Num. Int.	Num. Int.

Note:
Tri = Triangular layout; Stag = Staggered layout
Num. Int. = Numerical integration

From the reviewed literature, only Nitsu *et al*. (1969) presented a pressure drop correlation for a bare tube bundle under wet operation in addition to heat and mass transfer coefficients.

Anderson (2014) found that the pressure drop correlation presented by Nitsu *et al*. under predicts the measured pressure drop for wet operation by 30 % compared to his experimental results. This could be due to Nitsu *et al*. using a tube spacing of $2.35d_o$ which leads to a lower air flow resistance compared to Anderson's tube spacing of $2d_o$. Due to Nitsu *et al*.'s tube diameter and bundle layout, their correlations were not used in this study.

Anderson and Reuter (2016) presented a mass transfer, heat transfer and air-side pressure loss coefficient correlation for the bare tube bundle under wet and dry operation based on the experimental data of Anderson (2014). These correlations were all power functions of the critical air mass velocity, the deluge water flow rate and mean deluge water temperature. The correlations for the mass transfer, heat transfer and air-side pressure loss coefficients are presented as equations (2.3.14), (2.3.15) and (2.3.16).

$$h_d = 6.215 \times 10^{-4} \left(\frac{m_{avm}}{A_c}\right)^{0.8405} \left(\frac{\Gamma_{dw}}{d_o}\right)^{-0.4084} T_{dwm}{}^{1.1447} \tag{2.3.14}$$

$$h_{dw} = 90.186 G_c{}^{0.4242} \left(\frac{\Gamma_{dw}}{d_o}\right)^{0.4231} T_{dwm}{}^{0.5685} \tag{2.3.15}$$

$$K_{tb(w)} = 74.227 \left(\frac{m_{avm}}{A_c}\right)^{-0.1104} \left(\frac{\Gamma_{dw}}{d_o}\right)^{0.1955} T_{dwm}{}^{-0.08875} \tag{2.3.16}$$

which are valid for $2 < \left(\frac{m_{avm}}{A_c}\right) < 5.5$ kg/sm^2, $0.79 < \left(\frac{\Gamma_{dw}}{d_o}\right) < 1.45$ kg/sm^2 and $30 < T_{dwm} < 40$ ºC.

Figure 2.2 (a) presents a comparison of the mass transfer coefficients and Figure 2.2 (b) a comparison of the heat transfer coefficients of Parker and Treybal (1961), Mizushina *et al*. (1967), Nitsu *et al*. (1969) and Reuter and Anderson (2016). These mass transfer coefficients were evaluated at various air and deluge water mass velocities for a mean deluge water temperature of T_{dwm} = 30 ºC.

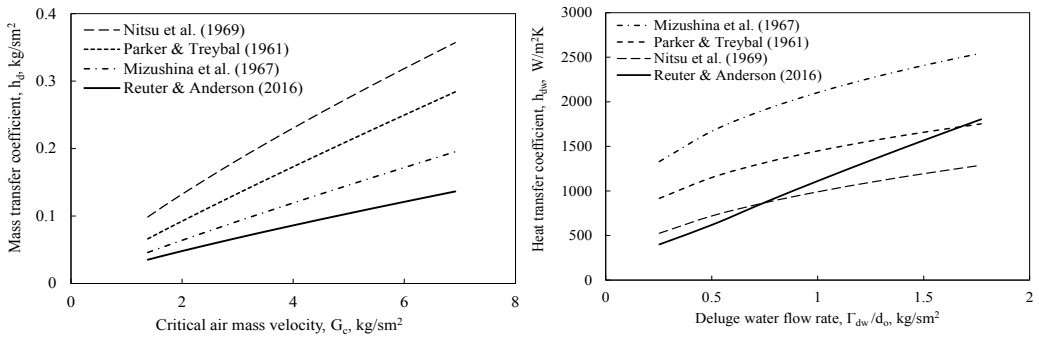

(a) (b)

Figure 2.2: Mass and heat transfer coefficients for wet operation

The mass transfer coefficient of Parker and Treybal (1961) and Nitsu *et al*. (1969) disregards the deluge water flow rate whereas Mizushina *et al*. (1967) and Reuter and Anderson (2016) defines the mass transfer coefficient as a function of both the deluge water and air flow rates.

The heat transfer rate defined by Parker and Treybal (1961) compensates for the deluge water temperature but disregards air flow. The heat transfer coefficient defined by Mizushina *et al*. (1967) and Nitsu *et al*. (1969) is a function of the deluge water flow rate whereas Reuter and Anderson (2016) presents the heat transfer coefficient as a function of the mean deluge water temperature, deluge water flow and air flow rate.

The current study stems from that of Anderson (2014), and the same bundle layout, tube diameter and tube spacing are incorporated. Figure 2.2, together with literature reviewed by Anderson supported the use of the integral model together with correlations suggested by Mizushina *et al*. (1967).

Figure 2.3 presents the air-side pressure drop under wet operation for Nitsu *et al*. (1969) and Reuter and Anderson (2016).

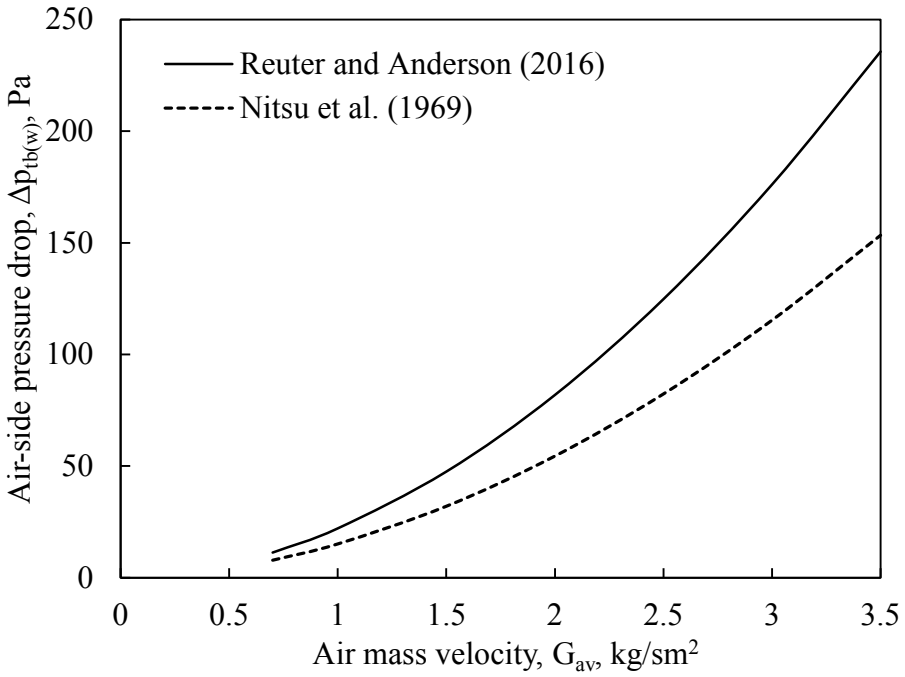

Figure 2.3: Air-side pressure drop under wet operation.

2.4 Wet operation parameters of bare tube bundles

2.4.1 Deluge water mass velocities

Nitsu *et al*. (1969) suggested that the mass transfer coefficient becomes dependant only on the deluge water mass velocity above $\Gamma_{dw}/d_o = 0.7$ kg/sm^2 and recommends

a deluge water mass velocity greater than Γ_{dw}/d_o = 0.8 kg/sm^2 to ensure perfect wetting of the tube surfaces.

Anderson (2014) concluded that increasing the deluge water mass velocity from Γ_{dw}/d_o = 0.95 kg/ms^2 to Γ_{dw}/d_o = 1.3 kg/ms^2 only lead to a 2 % gain in the bundle's heat transfer performance. This could be once perfect wetting was realised, the evaporation rate of water was independent of the deluge water flow rate.

Ribatski and Jacobi (2005) mentioned in their critical review on falling film evaporation that dry-out areas in deep bundles are common and responsible for poor heat transfer performance. Apart from this it was observed that enhanced surfaces (adding fins or grooves to the external surface of tubes) resulted in better heat transfer rates due to better wetting. They concluded that deluge water distribution had a significant effect on bundle performance and recommended that enhanced surfaces be used to increase water distribution.

2.4.2 Deluge water temperature measurement techniques

Apart from confirming small temperature deviations as observed by Mizushina *et al*. (1967), Anderson (2014) measured the deluge water temperature distribution through the height of the bare tube bundle. Temperature distributions are used in this study to validate the temperature profiles predicted by a row discretised performance model for the bare tube bundle under wet operation.

Dreyer (1988) measured the deluge water temperature by fabricating a funnel apparatus that is placed over the thermocouple tip to redirect deluge water and measure its temperature. Figure 2.4 (a) shows a drawing of the funnel apparatus. Dreyer did not mention how he attached thermocouples to his bundle.

Anderson (2014) measured the deluge water temperature by fabricating a small trough that is used to probe the bare tube bundle at different heights shown in Figure 2.4 (b). Eight thermocouples were laterally inserted through holes, across the height of the bare tube bundle after assembling it, but were not attached to the tubes in any way to guarantee their position during experiments, which in turn increases measurement uncertainty during experiments.

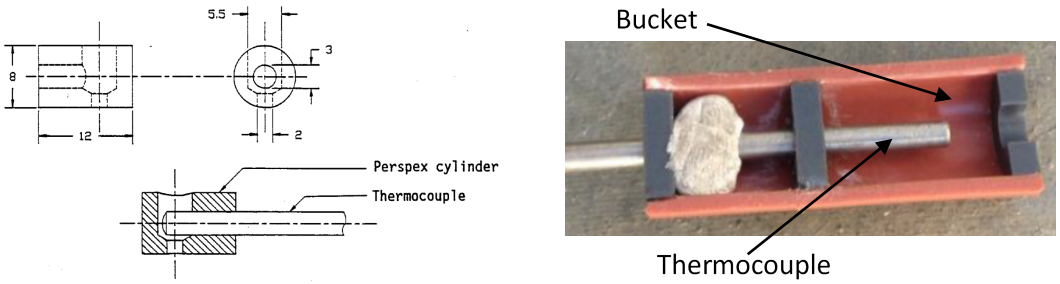

Figure 2.4: Deluge water catchment designs.

A new method of measuring the deluge water temperature profiles across the bundle is investigated in this study. In this method, the thermocouples are externally fastened to tubes throughout the bundle to ensure they remain in place during experiments. This is elaborated on in Chapter 4.

2.5 Chapter summary

This chapter presented a discussion on current research found in literature on novel cooling systems. From current literature into novel cooling systems, no similar multi stage cooling system as described by Owen (2013) and Anderson (2014), is found.

Apart from the integral model, row discretised models are developed to analyse the bundle on a spatial level. The row discretised model is presented in Chapter 3 together with applicable areas of employment.

The mass and heat transfer correlations of Mizushina *et al*. (1967) are selected for use in the integral model as their correlation set presided over the widest range of applicability.

Anderson (2014) noted a sharp rise in the pressure drop across the bare tube bundle above an air mass velocity of $G_{av} = 2.8$ kg/ms^2. He observed water retention in the bundle at this air mass velocity. This study investigates what leads to water retention in the bundle and how this phenomenon is affected by different deluge water flow and air flow rates. This is done by varying the air mass velocity between 0 kg/ms^2 to a maximum of 3.5 kg/sm^2.

Further, this study investigates how the bundle wetting develops by increasing the deluge water flow rate from Γ_{dw}/d_o = 0.5 kg/sm^2 to a maximum of Γ_{dw}/d_o = 1.9 kg/sm^2 which is a wider range than that investigated by Anderson (2014).

The severity of dry-out is analysed by investigating the dry-out areas in the bundle at lower deluge water flow rates. By documenting the deluge water flow through the bundle at various deluge water and air flow rates, the water retention phenomenon and minimum required deluge water flow rate can be determined.

3. THEORY

3.1 Introduction

The theory used in the development of a performance model for a bare tube bundle under wet (evaporative) and dry operation is presented in this chapter, together with that for a finned tube bundle under dry operation. Both an integral and a row discretised model are presented for the bare tube bundle. Experimental data from Anderson (2014) is used to compare the results of the integral and row discretised models. The integral and row discretised models are compared in order to establish if the integral model can be used to accurately model the bare tube bundle.

3.2 Evaporative cooler performance modelling

3.2.1 General mathematical model

The method of derivation presented in this thesis is adopted from Kröger (2004). Consider an elementary control volume of differential size containing a single round tube as depicted in Figure 3.1.

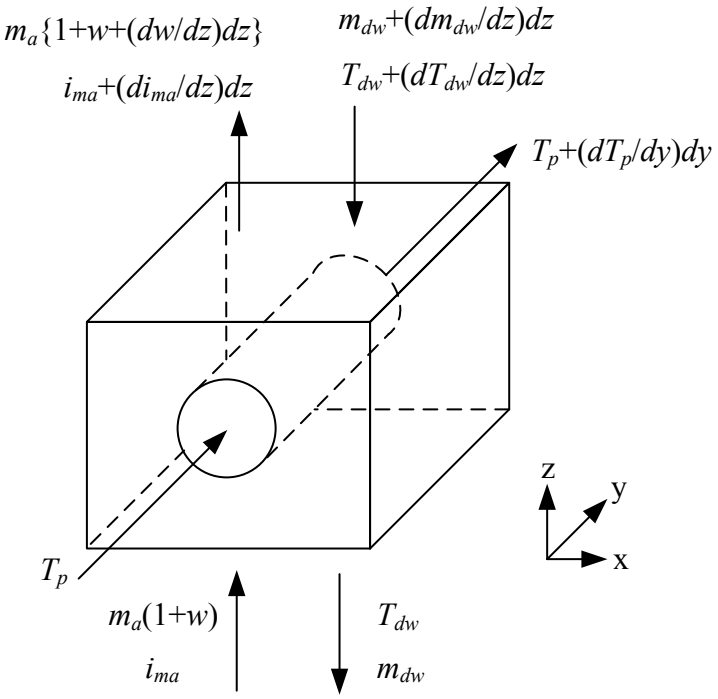

Figure 3.1: Elementary control volume (Kröger, 2004)

Tubes are sprayed with water which then falls down, in the negative z-direction, into an air stream flowing upward. The deluge water forms a thin water film, covering the outside tube area. A hot process medium travels inside the tube in the

y-direction and heats up deluge water. The deluge water partially evaporates into the passing air stream.

The equations governing the heat transfer process are derived by making the following assumptions:

- The process depicted in Figure 3.1 occurs at steady state.
- Radiation heat transfer is negligibly small.
- The temperature and humidity ratio of the air at the deluge water-air interface is that of a saturated air-vapour mixture at the mean deluge water temperature.
- A one dimensional analysis is applicable as the air, deluge water and process medium flow distributions are all uniform, resulting in fully wetted tubes.

An energy balance for the system can be written in differential form as,

$$dT_{dw} = \frac{m_a di_{ma} + m_p c_{ppm} dT_p}{m_{dw} c_{pdwm}} \tag{3.2.1}$$

where the change in air enthalpy is calculated by equation (3.2.2) and the change in process medium temperature is calculated by equation (3.2.3).

$$di_{ma} = \frac{h_d}{m_a}(i_{masdwm} - i_{ma}) dA_a \tag{3.2.2}$$

$$dT_p = \frac{U_a}{m_p c_{ppm}}\left(T_p - T_{dw}\right) dA_a \tag{3.2.3}$$

Equation (3.2.2) represents the change in air enthalpy due to mass transfer driven by an enthalpy difference. Equation (3.2.3) represents the change in temperature of the process medium due to heat transfer between the process medium and the deluge water driven by a temperature difference.

3.2.2 Integral model

The integral model solves the heat transfer rate across the whole bundle and assumes a constant deluge water temperature through the bundle to achieve this. To simplify the analysis procedure for the integral model, the assumptions of Merkel (1925) are employed, which are:

- The change in deluge water flow rate due to evaporation is negligible.
- A Lewis factor of unity is employed.
- The air stream leaving the bare tube bundle is saturated.

Mizushina *et al*. (1967) observed small changes in deluge water temperature across the bare tube bundle and proposed that a constant deluge water temperature ($dT_{dw} = 0$) could be assumed, eliminating equation (3.2.1). This method of analysis is known as the effectiveness – NTU (ε-NTU) method and is recommended by Kröger (2004) to evaluate the heat transfer performance for evaporative bundles.

Figure 3.2 displays the heat transfer resistance diagram, adapted from Anderson (2014) for the various modes of heat transfer between the hot process medium, deluge water and air stream. Heat is transferred by convection from the process medium to the inner tube wall, through the tube wall by conduction and through the deluge water film, into the air stream by convection heat transfer and mass transfer.

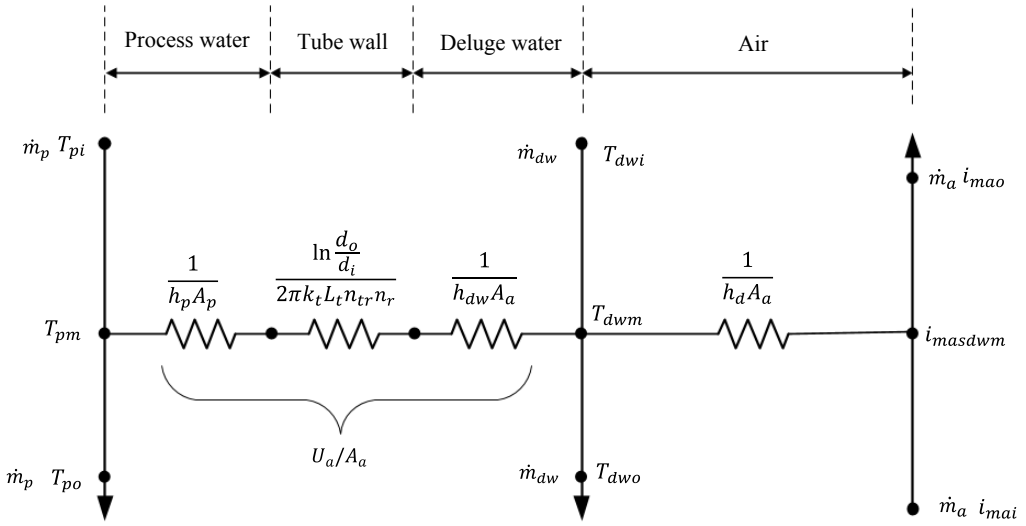

Figure 3.2: Wet thermal resistance diagram (Anderson, 2014)

With $dT_{dw} = 0$, equation (3.2.1) can be rearranged to form equation (3.2.4) which gives the overall heat transfer rate as,

$$Q = m_a(i_{mao} - i_{mai}) = m_p c_{ppm}(T_{pi} - T_{po}) \tag{3.2.4}$$

and links equations (3.2.2) and (3.2.3).

Equation (3.2.2) is integrated across the bundle and produces a log mean air enthalpy difference (Δi_{lm}) between the free stream air and the air at the water-air interface. The heat transfer rate to the air was calculated with equation (3.2.5) where the mass transfer coefficient (h_d) was determined with correlations from literature (equation 2.3.11 or 2.3.14).

$$Q = h_d A_o \frac{i_{mao} - i_{mai}}{ln\left(\frac{i_{masdwm} - i_{mai}}{i_{masdwm} - i_{mao}}\right)} = h_d A_o \Delta i_{lm} \tag{3.2.5}$$

The first definition in equation (3.2.4) is substituted into the left hand side (LHS) of equation (3.2.5) and the result rearranged, to give a relation for the outlet air enthalpy as presented in equation (3.2.6).

$$i_{mao} = i_{masdwm} - (i_{masdwm} - i_{mai})e^{-NTU_a} \tag{3.2.6}$$

where the air-side number of transfer units (NTU_a) is defined as,

$$NTU_a = \frac{h_d A_a}{m_a} \tag{3.2.7}$$

The enthalpy of saturated air (i_{masdwm}), is evaluated at the mean deluge water temperature, using equation (3.2.8).

$$i_{masdwm} = c_{pa} T_{dwm} + w_{sdwm}(i_{fgwo} + c_{pv} T_{dwm}) \tag{3.2.8}$$

where c_{pa} and c_{pv} are evaluated at $T_{dwm}/2 + 273.15$ K. Equation (3.2.3) is integrated to produce equation (3.2.9) in terms of a log mean water temperature difference (ΔT_{lm}) between the mean deluge water temperature and the process medium temperature.

$$Q = U_a A_a \frac{T_{pi} - T_{po}}{ln\left(\frac{T_{pi} - T_{dwm}}{T_{po} - T_{dwm}}\right)} = U_a A_a \Delta T_{lm} \tag{3.2.9}$$

The second relation of equation (3.2.4) is substituted into the LHS of equation (3.2.9) and rearranged to give a relation for the process medium outlet temperature given by,

$$T_{po} = T_{dwm} + (T_{pi} - T_{dwm}) e^{-NTU_p} \tag{3.2.10}$$

where the process side number of transfer units (NTU_p) is defined as,

$$NTU_p = \frac{U_a A_a}{m_p c_{ppm}} \tag{3.2.11}$$

The overall heat transfer coefficient (U_a) is based on the outside tube area and is defined by,

$$U_a = \left[\frac{d_o}{d_i h_p} + \frac{d_o ln\left(\frac{d_o}{d_i}\right)}{2k_t} + \frac{1}{h_{dw}}\right]^{-1} \tag{3.2.12}$$

In equation (3.2.12), the process medium heat transfer coefficient (h_p) is determined from equation (2.3.5) and deluge water heat transfer coefficient (h_{dw}) is obtained from equation (2.3.12) or (2.3.15). For heat exchanger performance modelling, equations (3.2.4) and (3.2.6) are used to solve the outlet air enthalpy, and equations (3.2.4) and (3.2.10) are used to solve the outlet process medium temperature.

Substituting equations (3.2.6) and (3.2.10) back into equation (3.2.4) and rearranging, the following relation for the mean deluge water temperature is found:

$$T_{dwm} = T_{pi} - \frac{m_a (i_{masdwm} - i_{mai})\left(1 - e^{-NTU_a}\right)}{m_p c_{ppm}\left(1 - e^{-NTU_p}\right)} \tag{3.2.13}$$

The heat transfer rate from the process fluid needs to equal that to the air. By adjusting the process medium outlet temperature, the heat transfer rate is adjusted.

A converged solution is iteratively found for the outlet air enthalpy, outlet process water temperature and mean deluge water temperature. This is achieved by solving the heat transfer rate from the process medium and to the air stream separately. The heat transfer rate is additionally solved by invoking the general heat transfer equation, equation (3.2.9). The outlet air conditions are assumed to be saturated, enabling the outlet air temperature to be solved iteratively with equation (3.2.8) by substituting i_{masdwm} with i_{mao}.

The process medium outlet temperature and mean deluge water temperature is solved by a backwards differencing scheme using equation (3.2.10) for the process water temperature and equation (3.2.13) for the mean deluge water temperature.

The air-side pressure drop over the bare tube bundle is calculated as,

$$\Delta p_{total(tb)} = K_{tb}\frac{G_{avm}^2}{2\rho} + \rho_{avo}\upsilon_{avo}^2 - \rho_{avi}\upsilon_{avi}^2 \qquad (3.2.14)$$

Where the air-side bundle loss coefficient (K_{tb}) is calculated with equation (2.3.16). The second and the third terms in equations (3.2.14) represent the change in momentum due to a change in air density and as such, air velocity.

One of the main advantages of the integral model is that the calculation procedure is simple and it models the heat transfer performance for the bare tube bundle as a whole. Anderson (2014) found the integral model accurate by implementing the correlations of Mizushina *et al*. (1967) (equations 2.3.11 and 2.3.12) which resulted in predicting the heat transfer rate to within 5% of his experimental data.

Air entering the bare tube bundle is unsaturated, and as such it cannot be assumed that air leaving a row is saturated with water vapour. The natural logarithm function in equations (3.2.5) and (3.2.9) is undefined when $i_{masdwm} < i_{mao}$ or $T_{dwm} > T_{po}$. These limits make the integral model sensitive to the mean deluge water temperature, and care should be taken when calculating the mean deluge water temperature from experimental results.

3.2.3 Row discretised model

The row discretised model, developed in this study, is an explicit model that calculates the heat transfer rate and unknown fluid temperatures for each row based on the inlet air condition and outlet process water temperature of the bundle. The deluge water recirculates over the bare tube bundle and as such the inlet and outlet temperatures thereof are equal (i.e. the water collected below the bundle is pumped directly to the spray nozzles above the bundle). Figure 3.3 highlights the differences between the integral model and the row discretised model.

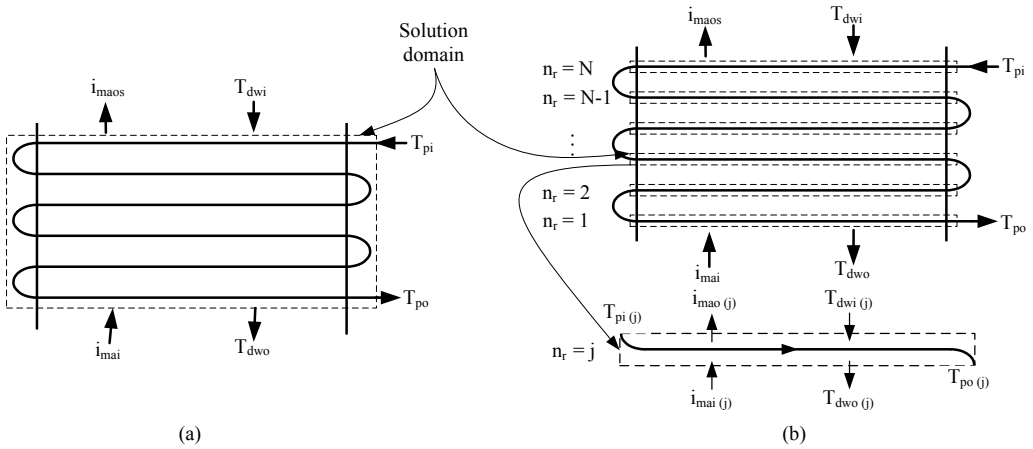

Figure 3.3: The (a) integral and (b) row discretised bare tube bundle models

Consider the control volume in Figure 3.3(b). By assuming negligible water mass loss due to evaporation, an energy balance for row $n_r = j$, where Q represents heat transfer rate, is written as,

$$Q_{p(j)} = Q_{a(j)} + Q_{dw(j)} \tag{3.2.15}$$

where

$$Q_{p(j)} = m_p c_{ppm}\left(T_{pi(j)} - T_{po(j)}\right) \tag{3.2.16}$$

$$Q_{a(j)} = m_a\left(i_{mao(j)} - i_{mai(j)}\right) \tag{3.2.17}$$

$$Q_{dw(j)} = m_{dw} c_{pdwm}\left(T_{dwo(j)} - T_{dwi(j)}\right) \tag{3.2.18}$$

By discretising the integral model, the log mean differences in equations (3.2.5) and (3.2.9) are replaced with average differences to increase stability. Equations (3.2.5) and (3.2.9) are subsequently rewritten as,

$$Q_{a(j)} = h_d A_a\left(i_{masdwm(j)} - \frac{i_{mao(j)}+i_{mai(j)}}{2}\right) = h_d A_a \Delta i_{avg} \tag{3.2.19}$$

$$Q_{p(j)} = U_a A_a\left(\frac{T_{pi(j)}+T_{po(j)}}{2} - T_{dwm(j)}\right) = U_a A_a \Delta T_{avg(j)} \tag{3.2.20}$$

with A_a the total outside tube area of the tube row and $T_{dwm(j)} = 0.5\left(T_{dwi(j)} + T_{dwo(j)}\right)$.

The calculation procedure for determining the performance characteristics from measurement data initiates at the bottom row ($n_r = 1$ from Figure 3.3(b)) where the air inlet condition and process medium outlet temperature are known. An initial deluge water outlet temperature, smaller than the given process medium outlet temperature, is guessed as an initial value.

With this information available, the inlet process medium temperature and heat transfer rate can be calculated from equations (3.2.19) and (3.2.20) for row $n_r = 1$. By combining equations (3.2.17) and (3.2.19) and rearranging, the air outlet enthalpy for the row is calculated as,

$$i_{mao(j)} = (1 + 0.5NTU_a)^{-1}\left[i_{masdwm(j)}NTU_a + i_{mai(j)}(1 - 0.5NTU_a)\right] \qquad (3.2.21)$$

The heat transfer rate to the air is calculated from equation (3.2.17). Rearranging equation (3.2.15), the heat transfer rate to the deluge water is determined. From equation (3.2.18) the deluge water inlet temperature is calculated. A new mean deluge water temperature is calculated and the calculation process is repeated for the current row.

Calculated values for the current row are set as initial conditions for the next row. In general, for row $n_r = j+1$ the inlet values can be expressed as,

$$T_{po(j+1)} = T_{pi(j)} \qquad (3.2.22)$$

$$i_{mai(j+1)} = i_{mao(j)} \qquad (3.2.23)$$

$$T_{dwo(j+1)} = T_{dwi(j)} \qquad (3.2.24)$$

This process is repeated for each row. For the top row ($n_r = N$ from Figure 3.3(b)), the calculated deluge water inlet temperature ($T_{dwi(N)}$) is compared to the outlet deluge water temperature ($T_{dwo(1)}$) from the bottom row. $T_{dwo(1)}$ is adjusted as,

$$T_{dwo(1)}{}^{new} = T_{dwo(1)}{}^{old} + F_r(T_{dwi(N)}{}^{old} - T_{dwo(1)}{}^{old}) \qquad (3.2.25)$$

where $F_r < 1$ is a relaxation factor to ensure the model does not diverge in its initial calculation phase.

The row discretised model is solved iteratively until the second term on the right hand side of equation (3.2.25) is effectively zero, resulting in the outlet and inlet deluge water temperatures being equal.

By discretising the integral model into rows, the log mean differences (in equations 3.2.5 and 3.2.9) are replaced by average differences (equations 3.2.19 and 3.2.20). This substitution eliminates areas where the natural logarithm is undefined and leads to a more stable performance prediction model. Apart from increased solving stability the row discretised model calculates temperature profiles for the process medium and deluge water through the height of the bundle. The row discretised model allows for investigation of the water temperature and air enthalpy changes anywhere in the bundle.

The row discretised model converges sequentially on a row by row level and as such requires more time to solve compared to the integral model.

3.3 Obtaining heat transfer performance characteristics from experimental data

Reuter & Anderson (2016) presented mass transfer and heat transfer correlations based on a bare tube bundle of 25 tube rows (equations 2.3.14 and 2.3.15) which are determined using the integral method together with experimental data from Anderson (2014). In order to evaluate if the integral model solves to an accurate degree, this study uses Andersons' experimental data together with the row discretised model to validate the accuracy of the integral model as well as to determine new correlations for the mass transfer and heat transfer coefficients.

Anderson (2014) experimental work included 16 thermal tests, where the air and deluge water mass velocities were varied. Table 3.1 presents Anderson's experimental data ranges.

Table 3.1: Experimental input data ranges. (Anderson, 2014)

Input data	Symbol	Range	Unit
Inlet dry bulb temperature	T_{ai}	16.8 to 21.4	ºC
Inlet wet bulb temperature	T_{wbi}	13.6 to 14.8	ºC
Inlet process water temperature	T_{pi}	37.1 to 48.4	ºC
Mean deluge water temperature	T_{dwm}	21.1 to 40.9	ºC
Air mass velocity	G_{av}	1 to 2.8	kg/sm^2
Critical air mass velocity	G_c	2.1 to 5.8	kg/sm^2
Deluge water mass velocity	G_{dw}	1.5 to 3.5	kg/sm^2
Process water mass flow rate	m_p	10.0	kg/s

Andersons' experimental data is used to calculate heat and mass transfer coefficients on a row by row level (employing the row discretised model). With multiple linear regression, these calculated heat transfer coefficients are correlated as functions of the air mass velocity, deluge water mass velocity and mean deluge water temperature. The correlation for the mass transfer coefficient is presented as equation (3.3.1) and the correlation for the heat transfer coefficient as equation (3.3.2).

$$h_d = 0.1823 G_c^{0.5301} \left(\frac{\Gamma_{dw}}{d_o}\right)^{0.1720} T_{dwm}^{-0.4063} \tag{3.3.1}$$

$$h_{dw} = 1799270\, G_c^{-0.3589} \left(\frac{\Gamma_{dw}}{d_o}\right)^{0.5274} T_{dwm}^{-1.8889} \tag{3.3.2}$$

where T_{dwm} is the mean temperature of the deluge water across the bundle in degrees Celsius (ºC).

Figure 3.4 presents a power curve fit through the data by comparing the calculated mass and heat transfer coefficients with that predicted by the correlations obtained through linear regression (equations. 3.3.1 and 3.3.2).

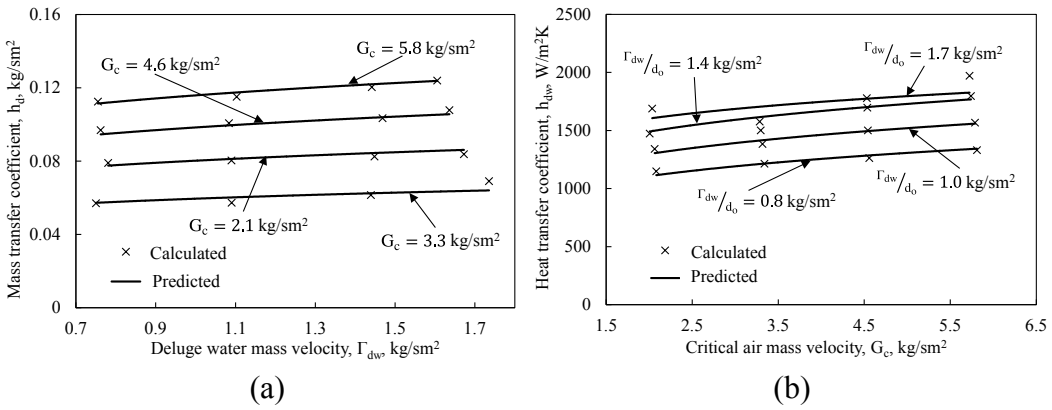

Figure 3.4: Row discretised model mass and heat transfer coefficients

Two measured deluge water temperature profiles from Anderson (2014) together with the deluge water temperature profile predicted by the row discretised model (using equations 3.3.1 and 3.3.2) are presented in Figure 3.5.

These two deluge water temperature profiles are used to validate the row discretised model. The row discretised model predicts Anderson's data well in Figure 3.5 (b) except for a deviation between the measured and predicted deluge water temperature in the lower part of the bundle as presented in Figure 3.5 (a). This deviation could be attributed to uncertainty surrounding the deluge water temperature measurement techniques employed by Anderson.

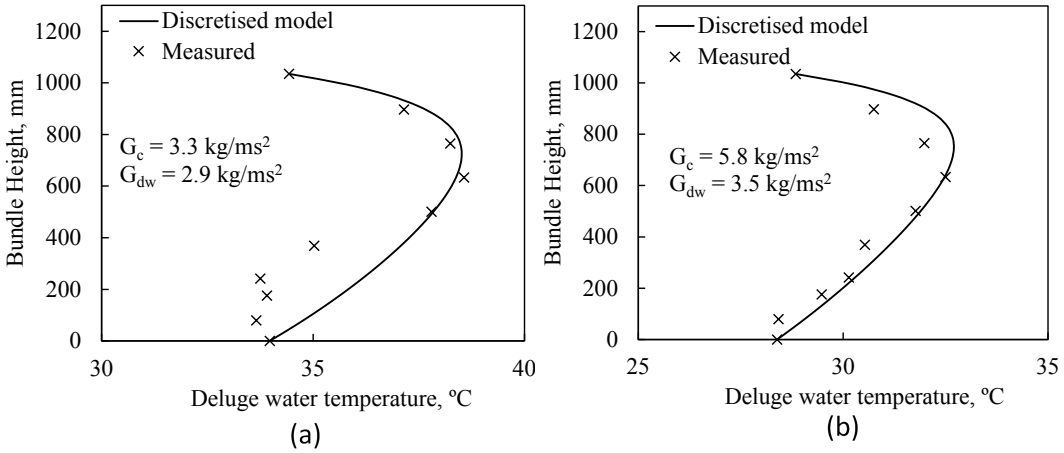

Figure 3.5: Discretised model validation with measured data

3.4 Comparison of the integral and row discretised models

The integral and row discretised models are compared to each other based on the heat transfer rate predicted when different correlations for the mass and heat transfer coefficients are employed. The calculated correlation set, presented as equations (3.3.1) and (3.3.2), together with the correlation set from Mizushina *et al*. (1967), presented as equations (2.3.11) and (2.3.12), are employed in both the integral and row discretised models. The correlation set by Reuter and Anderson (2016), equations (2.3.14) and (2.3.15), are employed in the integral model together with that from Parker and Treybal (1961) to show how they compare to equations (3.3.1) and (3.3.2) and those proposed by Mizushina *et al*. (1967).

The correlation set of Mizushina *et al* (1967) is implemented in the row discretised model to determine if correlations determined from the integral method can accurately predict the heat transfer rate when employed in a row discretised model. The integral and row discretised models both require the process water outlet temperature together with the air inlet condition as given parameters.

Based on these parameters, the integral model calculates the process water inlet temperature, mean deluge water temperature and outlet air temperature, whereas the row discretised model calculates temperature profiles of the process water and deluge water, together with the air enthalpy profile through the bare tube bundle.

Figure 3.6 presents the process water and deluge water temperature profiles predicted through the bare tube bundle.

From Figure 3.6, the correlation set of Mizushina *et al*. (1967) over predicts both the process medium and deluge water temperature profiles, compared to equations (3.3.1) and (3.3.2). This demonstrates that the correlation set of Mizushina *et al*. (1967) cannot be employed in the row discretised model to predict accurate temperature profiles.

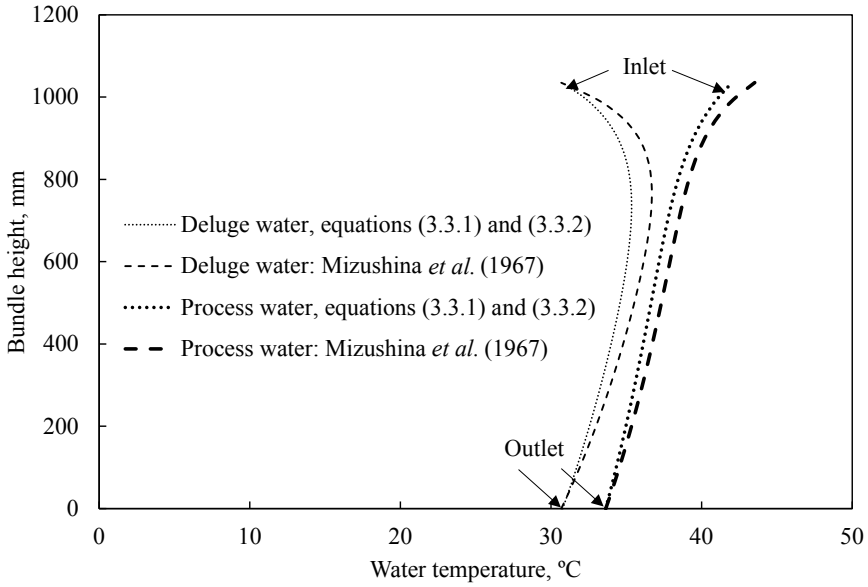

Figure 3.6: Temperature profiles from the row discretised model.

3.4.1 Predicted heat transfer rate from the integral and row discretised models

When implemented in the row discretised model, Mizushina *et al*. (1967) over predicted the heat transfer rate with as much as 28% and on average over predicted the heat transfer rate by 20%. The predicted heat transfer rates from the various other correlation sets employed in the integral and row discretised models are presented in Figure 3.7.

Figure 3.7 presents a comparison of the different heat transfer rates as predicted by different correlation sets. From Figure 3.7 the following deductions are made:

- Equation (3.3.1) and (3.3.2) predicts the heat transfer rate accurately when implemented in both the integral and row discretised models. With these equations, a maximum prediction error of 5.6 % is observed in the integral model. A maximum prediction error of 6.2 % is observed in the row discretised model. On average, equations (3.3.1) and (3.3.2) predicts the heat transfer rate to within 2.9 % of the measured value.

- From the correlation sets found in literature, Mizushina *et al*. (1967) predicts the heat transfer rate best in the integral model. In fact, Mizushina *et al*. (1967) predicts the heat transfer rate almost just as accurately (with an average prediction error of 3.0 %) as equations (3.3.1) and (3.3.2) - with an average prediction error of 2.9 %. Reuter and Anderson (2016) followed with an average over prediction of 4 %, and Parker and Treybal (1961) predicted the heat transfer to the least accurate degree with an average of 5.6 %.

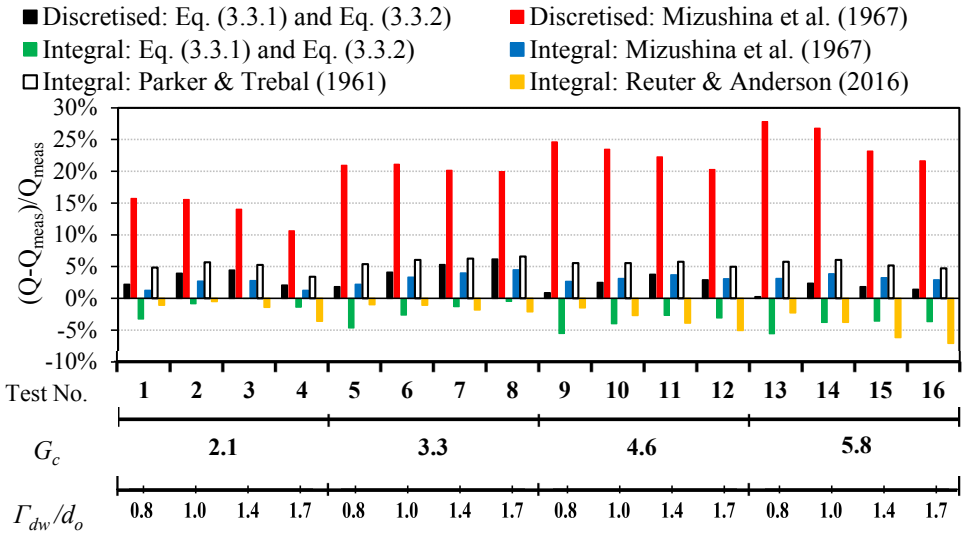

Figure 3.7: Predicted heat transfer rates from integral and discretised models

3.4.2 Applicability of different models

The previous subsection section shows it is possible to predict temperature profiles for the process water and deluge water from a certain mass transfer and heat transfer coefficient correlation set, using the row discretised model together with experimental data.

Good agreement between the various heat transfer rates, predicted using certain mass transfer and heat transfer coefficient correlations sets, are found with the integral model.

The correlations of Mizushina *et al*. (1967) do not predict the heat transfer rate to an accurate degree when implemented in the row discretised model. However, accurate performance predictions are observed when the correlation set of Mizushina *et al*. (1967) is implemented in the integral model. Possible reasons for the over prediction using the correlation set of Mizushina *et al*. (1967) could be the relative large heat transfer coefficient compared to the calculated value from equation (3.3.1). The predicted temperature profiles are less sensitive for a change in the mass transfer coefficient compared to a change in the heat transfer coefficient.

The row discretised model delivers more accurate temperature predictions compared to the integral model as it calculates temperature profiles for the process water and deluge water through the height of the bundle instead of inlet and outlet conditions across the bundle.

The row discretised model will be the preferred model for predicting condenser performance due to its ability to identify regions of vapour backflow. Condenser performance is dramatically decreased with the onset of vapour back-flow in tube rows. This occurs when higher heat transfer rates (typically in the bottom tube rows in a bundle due to colder air) allow for total condensation of steam midway through the tube row.

The pressure recovery inside tubes, due to condensation, creates a negative pressure gradient between the point of total condensation, midway through the tube, and the collecting header. This allows for steam to be drawn in from both the distributing and collection headers. Non-condensable gasses accumulate in these areas (midway in the tube) and dead spots arise, which severely affects the heat transfer performance of a condenser.

As the HDWCS is intended to be used as a cooler and not a condenser (liquid is cooled instead of a phase change occurring, vapour back-flow is thus not a problem). Apart from this, the integral model converges quicker compared to the row discretised model due to it not evaluating the bundle on a row by row basis. For this study, the heat transfer performance of the bare tube bundle will be predicted using the integral model.

3.5 Dry cooler performance modelling

3.5.1 Performance modelling for dry operation

The bare tube bundle operates as a dry cooler during colder periods and periods with low wind speeds. The control volume is similar to that in Figure 3.1, with the exception of no deluge water present. Figure 3.8 is adapted from Anderson (2014) and presents the thermal resistance diagram for dry operation.

Following a similar procedure as in section 3.2 the heat transfer rate from the process water is equal to that of the air and expressed by,

$$Q = m_a c_{pam}(T_{ao} - T_{ai}) = m_p c_{ppm}\left(T_{pi} - T_{po}\right) \tag{3.5.1}$$

Using the general heat exchanger equation, the heat transfer rate can also be expressed as,

$$Q = U_a A_a \frac{(T_{pi} - T_{ao}) - (T_{po} - T_{ai})}{ln\left(\frac{T_{pi} - T_{ao}}{T_{po} - T_{ai}}\right)} = U_a A_a \Delta T_{lm} \tag{3.5.2}$$

where U_a is the overall heat transfer coefficient based on the outside tube area and defined by,

$$U_a = \left[\frac{d_o}{h_p d_i} + \frac{d_o ln\frac{d_o}{d_i}}{2k_t} + \frac{1}{h_a}\right]^{-1} \tag{3.5.3}$$

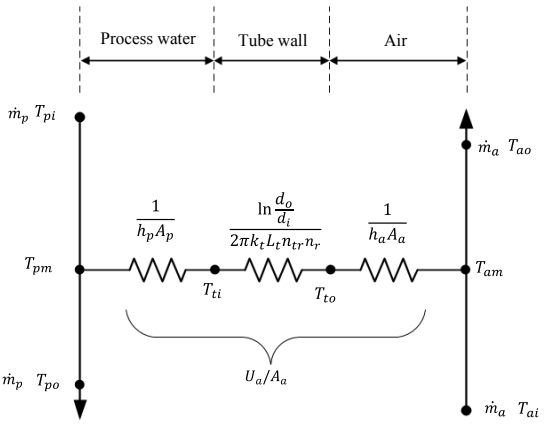

Figure 3.8: Dry thermal resistance diagram (Anderson, 2014)

The internal convection heat transfer coefficient (h_p) is presented as equation (2.3.5), the convection heat transfer rate between the tube outside surface and air stream (h_a) is that suggested by Khan *et al*. (2006) and presented as equation (2.3.9).

The average tube outside surface temperature is required by some correlations in literature and can be obtained from rearranging equations. (3.5.1) and (3.5.3) to yield,

$$T_{to} = T_{pm} - Q\left[\frac{1}{h_p A_p} + \frac{ln\frac{d_o}{d_i}}{2\pi k_t L_t n_{tr} n_r}\right] \tag{3.5.4}$$

The air outlet temperature is determined by rearranging the first definition of equation (3.5.1) as,

$$T_{ao} = T_{ai} + \frac{Q}{m_{av} c_{pam}} \tag{3.5.5}$$

The process water outlet temperature can similarly be calculated by rearranging the second definition of equation (3.5.1) as,

$$T_{po} = T_{pi} - \frac{Q}{m_p c_{ppm}} \tag{3.5.6}$$

And the pressure drop over the dry bare tube bundle is calculated from,

$$\Delta p_{tb(d)} = \frac{K_{tb(d)}\rho_{avm}v_{avm}^2}{2} + \rho_{avo}v_{avo}^2 - \rho_{avi}v_{avi}^2 \tag{3.5.7}$$

where $K_{tb(d)}$ is the bundle loss coefficient for dry operation determined from equation (2.3.10).

The pressure drop under wet operation can similarly be determined by inserting the air-side pressure loss coefficient under wet operation as determined from equation (2.3.16) into equation (3.5.7). The second and third terms in equation (3.5.7) represent the change in dynamic pressure due to a change in the velocity and density of the air mixture across the bare tube bundle.

3.6 Finned bundle performance modelling

The finned bundle remains under dry operation due to fouling and corrosion concerns. Cleaning of finned tube bundles would be cumbersome due to the small gaps between fins, and bio-fouling can easily occur if the finned bundle is deluged with water. Small gaps between fins, together with the surface tension of water bring forth the capillary effect, where water particles are trapped between fins and can easily corrode the fin material.

For finned tube bundles, the total heat transfer coefficient (U_a) is modified to accommodate the additional transfer surface of fins. In addition to this, the air-side heat transfer coefficient by Ganguli *et al*. (1985), presented as equation (2.3.9) is implemented. Equation (3.5.3) is subsequently modified for a finned tube bundle under dry operation as,

$$U_a = \left[\frac{d_o}{h_p d_i} + \frac{d_o ln\frac{d_o}{d_i}}{2k_t} + \frac{1}{h_a e_f}\right]^{-1} \tag{3.6.1}$$

where e_f is the fin effectiveness and defined by,

$$e_f = 1 - \left(1 - \eta_f\right)\frac{A_f}{A_a} \tag{3.6.2}$$

where A_f is the total finned area and A_a the total air-side area of the finned tube bundle. The fin efficiency (η_f) is defined by Schmidt (1946) as,

$$\eta_f = \frac{tanh\left(bd_r\frac{\phi}{2}\right)}{bd_r\frac{\phi}{2}} \tag{3.6.3}$$

where,

$$b = \sqrt{\frac{2h_a}{k_f t_f}} \tag{3.6.4}$$

and k_f is the fin thermal conductivity with t_f the fin thickness. The parameter ϕ is defined as

$$\phi = \left(\frac{d_f}{d_r} - 1\right)\left[1 + 0.35ln\left(\frac{d_f}{d_r}\right)\right] \tag{3.6.5}$$

where d_f and d_r are the root and the fin diameters respectively.

As the air-side transfer surface increases for finned tubes, higher pressure losses are expected. Equation (2.3.8) is used to predict the air-side pressure drop over the finned tube bundles.

The core finned tube model is validated against that of Ackers (2012) in Appendix D. From this core model, components such as other heat transfer coefficient correlations as used in the example, are added to further develop the HDWCS performance model.

3.7 Discussion and recommendations

3.7.1 Delugeable bare tube bundle

This chapter presents theory concerning the performance evaluation of the bare tube bundle under wet and dry operation and the finned tube bundle under dry operation. The performance of the bare tube bundle is modelled in two ways. The integral model considers the bundle as a whole and the row discretised model considers each tube row as an independent bundle.

Correlation sets from literature accurately predict the heat transfer rate when implemented with the integral model. The correlation set of Mizushina *et al*. (1967), predicted the performance best when used with the integral model and are to be implemented in HDWCS performance prediction model to predict the heat transfer performance of the bare tube bundle under wet operation. The row discretised model is recommended when condenser performance is modelled.

Numerous correlations from literature are available for the air-side heat transfer coefficient for bare tube bundles under dry operation and are in good agreement with each other. The heat transfer correlation proposed by Khan *et al*. (2006) will be used to predict the heat transfer performance for the bare tube bundle under dry performance as Anderson (2014) showed it predicted his dry performance best compared to his experimental results.

The pressure drop correlation proposed by Reuter & Anderson (2016) will be used to predict the air-side pressure drop over the bare tube bundle under dry and wet operation, as their bare tube bundle is of a similar geometry and layout, used in the HDWCS.

3.7.2 Finned tube bundle performance

The finned bundle performance is predicted in a similar fashion to the bare tube bundle under dry operation. A fin effectiveness is introduced in the total heat transfer coefficient to accommodate the additional heat transfer area and compensate for the fin temperature distribution.

The heat transfer correlation of Ganguli *et al*. (1985) will be used to determine the air-side heat transfer coefficient together with their air-side pressure loss coefficient correlation as proposed by Ackers (2012).

4. EXPERIMENTAL WORK

4.1 Introduction

In this chapter, the experimental work is presented. The heat transfer wind tunnel at Stellenbosch University is described followed by a description of the experimental apparatus and subsequent modifications thereof to accommodate each investigation surrounding the bare tube bundle. Further the experiments are presented together with measuring techniques employed, followed by the experimental procedure and the results thereof, before recommendations pertaining to the observations are presented.

4.2 Test Facility

The experiments are conducted in the heat transfer laboratory at Stellenbosch University. Figure 4.1 displays the wind tunnel used to induce an air flow and measure the air mass flow rate through the test apparatus.

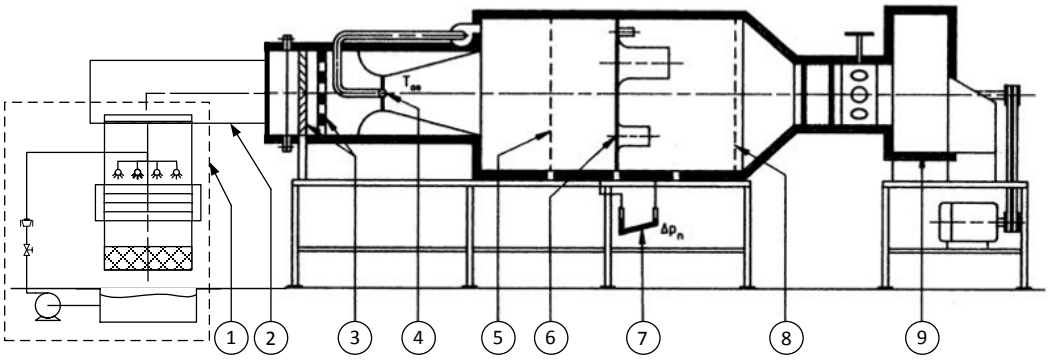

Figure 4.1: Heat transfer wind tunnel at Stellenbosch University

From Figure 4.1, the test apparatus (1) is attached to the wind tunnel with a modified inlet (2). A set of mixing vanes (3) are followed by a Venturi contraction with a sampling tube (4) to measure air temperature. Perforated plates at (5) and (8) ensure a uniform velocity distribution over elliptical nozzles (6). The air mass flow rate is determined from measuring static pressure drop at (7). Air flow through the wind tunnel is induced by a radial fan (9).

4.3 Apparatus

4.3.1 Description

The experimental apparatus is presented in Figure 4.2, with Figure 4.2 (a) a schematic of the experimental apparatus and Figure 4.2 (b) an annotated photograph. Bundle dimensions and layout geometry are presented in Figure 4.3.

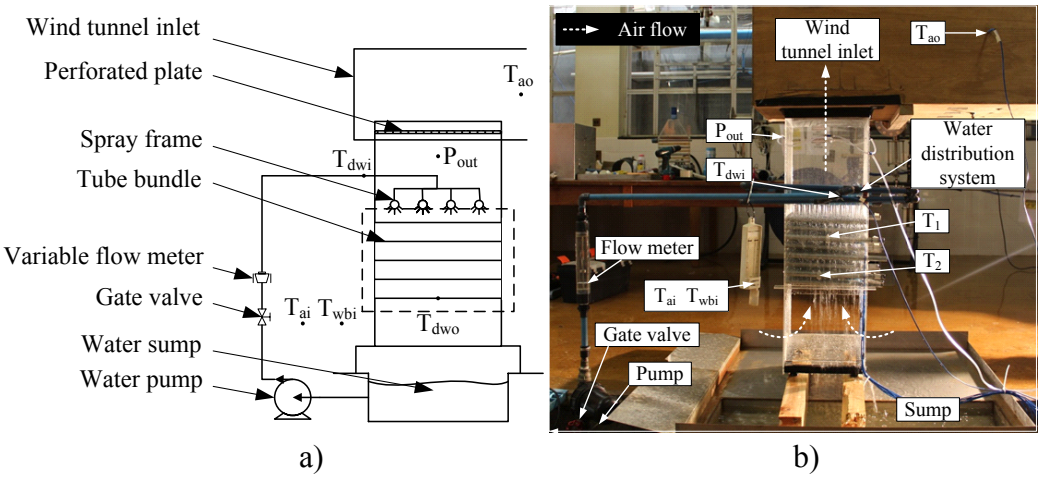

Figure 4.2: Test apparatus

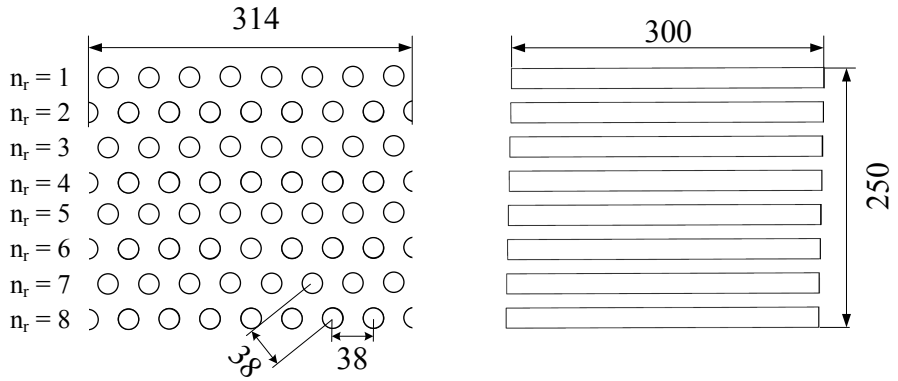

Figure 4.3: Bundle dimensions and layout geometry

From Figure 4.3, the tube bundle consists of 60 bare tubes with an outer tube diameter, d_o = 19 mm. The bundle has a triangular tube layout of $2d_o$, with 8 tube rows and 8 tubes per row. The bundle measures 314 mm wide, 250 mm high and 300 mm long. The bundle is at a one degree slope (from left to right in Figure 4.2b) to coincide with the slope of the bundle from Anderson (2014).

Wooden dowels are added to the sides of the bundle structure for the rows containing 7 tubes per row (n_r = 2, 4, 6 and 8). The wooden dowels ensures a uniform air flow resistance around the bundle. For experiment 3, rows are consecutively removed from the bundle in order to characterise the pressure drop as a function of the number of tube rows.

4.3.1 Operation

With reference to Figure 4.2 (b), water is pumped from a sump by a centrifugal pump, at a given flow rate which is controlled with an in-line gate valve, and

distributed over the bare tube bundle by the water distribution system (WDS). Water trickled down through the bundle under gravity and returned to the sump from where it is recirculated.

Counter-flow is achieved by inducing an air flow upwards across the bare tube bundle with the radial fan in the wind tunnel. The air flow is controlled by adjusting the fan speed with a variable speed drive (VSD) connected to the power supply of the radial fan.

4.4 Experiment description

The following three experiments are conducted using the experimental apparatus:

1. Investigation of the critical air flow and bundle wetting.
2. Thermocouple attachment methods and placement.
3. Effect of the number of tube rows on the air-side pressure drop across a bare tube bundle under wet and dry operation.

For the remainder of this chapter the experiments will be referred to as experiments 1, 2 and 3.

Experiment 1 stems from observations made by Anderson (2014). He found a sharp rise in the air-side pressure drop across the bundle above a critical air flow rate of G_{av} = 2.8 kg/sm^2. The effect of different deluge water flow rates on the critical air flow value is therefore investigated.

Experiment 2 is conducted to investigate two attachment methods for thermocouples on the bare tubes to determine if the thermocouples remain wet for different deluge water flow rates. Anderson (2014) does not specify measurement certainty pertaining to the deluge water temperature throughout the bundle which was evident in the data from Figure 3.5 (a) and neglects to specify if his trough concept, which retains water to keep the thermocouple measuring tip wet, remains stationary during tests – which can greatly affect the measured water temperature. The trough concept of Anderson was presented in Figure 2.4 (b).

Experiment 3 evaluats the air-side pressure drop over the bare tube bundle in order to develop pressure drop correlations that can be used to predict the air-side pressure drop for wet and dry operation. In addition, the pressure drop correlation has to account for the number of tube rows present in the bundle. Only Nitsu *et al*. (1969) presents a pressure drop correlation for a counter-flow bare tube bundle under wet operation, but Anderson (2014) shows Nitsu *et al*. under predicts the measured pressure drop from his experimental results. It is therefore necessary to have more accurate correlations for accurate analysis of the performance of the HDWCS.

4.5 Apparatus modification for experiment 3

To ensure maximum repeatability of experimental results, a change in air-side pressure drop should only be due to the controlled variables (air flow and water flow rates and number of tube rows present in the bundle).

Kröger (2004) shows that the air inlet loss coefficient of a bundle housing structure is dependent on the air-side bundle loss coefficient. As tube rows are removed from the bundle, the air-side bundle loss coefficient is expected to decrease. With a change in the air-side flow resistance across the bundle, the air flow pattern through the side inlets will change, causing a change in the inlet loss coefficient (change in pressure loss due to change in air flow direction). To prevent any changes in the air inlet flow patterns when tube rows are removed, a one dimensional inlet is developed. Figure 4.4 presents the experimental apparatus with the side inlets in Figure 4.4 (a) and a uniform one dimensional air inlet in Figure 4.4 (b).

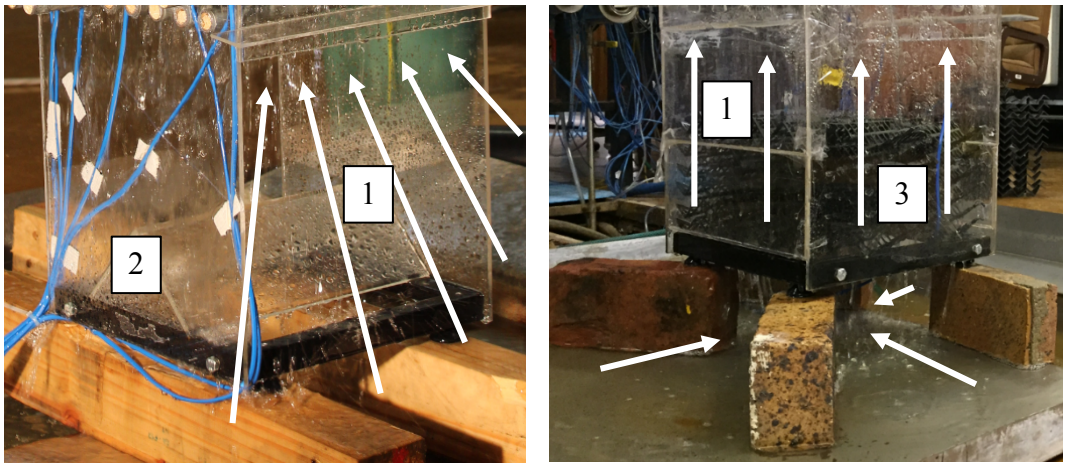

(a) (b)

Figure 4.4: Air inlet modification with (a) side inlets and (b) uniform inlet

The one dimensional inlet is created by closing the bundle side inlets (1), removing the triangular support (2) in the bottom and adding a flow resistance (3) to evenly distribute the air flow upstream from the bundle.

4.6 Measuring equipment and techniques.

4.6.1 Temperature

For experiment 1 and 2, the water temperature is measured through the bundle in order to determine if the thermocouples remains wet. For experiment 3, only the inlet and outlet water temperatures are measured.

The water and air temperatures are measured with 100 mm long, 1.6 mm thick type-T thermocouples, manufactured by Temperature Controls (Pty) Ltd. The temperature readings are recorded with a Keysight® LXI data acquisition module

which uses software from Agilent Bench link to process the instrument signals into measurements. Appendix C presents the calibration procedure for the thermocouples.

The thermocouples are attached to the bare tubes with zip ties. Zip ties are economically a better alternative to manufacturing brackets. The zip ties fixes the thermocouples to the tubes, keeping the measuring tips in place and ensuring they remain stationary during tests.

Two attachment methods are investigated. The first method entails four zip ties – one to tie down the thermocouple itself and three for the measuring tip. The second method uses three zip ties – one for the thermocouple and two for the measuring tip. More than one zip tie is required to keep the measuring tip close to, but not touching, the tube surface. Figure 4.5 shows the thermocouples attached to the tubes, with Figure 4.5 (a) presenting the first attachment method and Figure 4.5 (b) the second method.

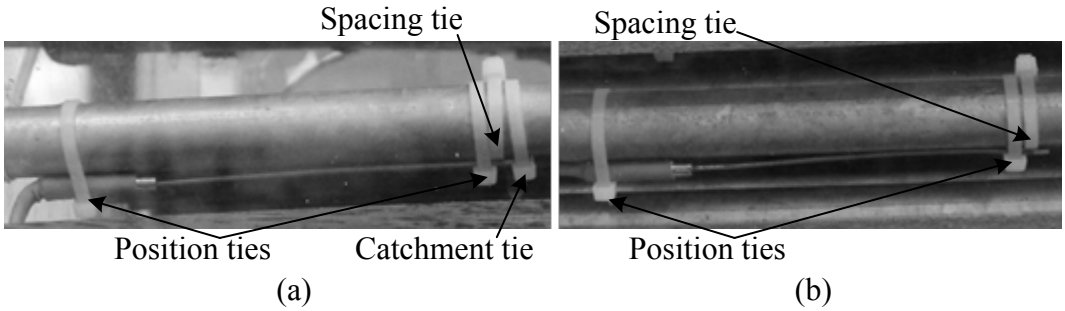

Figure 4.5: Thermocouple attachments

With the first attachment method, the fourth zip tie head acted as a water catchment underneath the measuring tip. This catchment, together with the surface tension of the deluge water, would ensure the tip remained wet. The second method left the measuring tip open with no catchment underneath. With these two methods it was possible to determine if a fourth zip tie could increase measuring certainty. Figure 4.6 displays the different thermocouple positions, where water and air temperature were measured for the different experiments.

Figure 4.6 (a) displays the thermocouple positions for experiments 1 and 2. Thermocouples T_1 to T_3 were placed at the sides of the bundle to ease visual evaluation of the water film flow over the thermocouples. Thermocouples T_4 to T_6 were placed horizontally in row six to measure horizontal variation in water temperature.

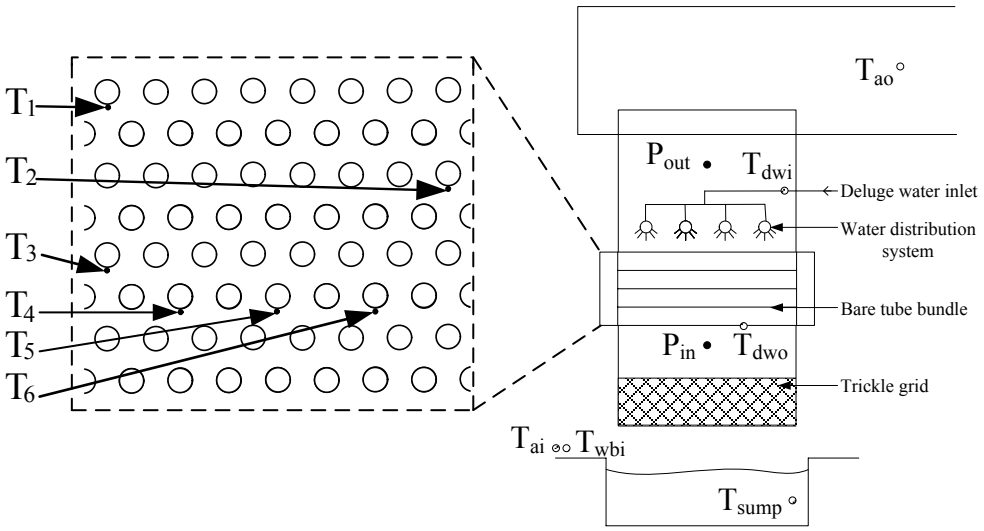

Front bundle view (a)

Side bundle view (b)

Figure 4.6: Thermocouple positions for experiments from the (a) front and (b) side.

Figure 4.6 (b) displays the thermocouple positions and pressure measuring positions for experiment 3. Since tube rows are removed from the bare tube bundle during experiment 3, the water temperature through the bundle is not measured. The dry and wet bulb ambient air temperatures are measured at the air inlet. The outlet air temperature is measured in the wind tunnel inlet.

4.6.2 Air mass flow rate

In order to measure the air mass flow rate through the apparatus, the static pressure drop across an elliptical nozzle inside the wind tunnel (7 from Figure 4.1) is measured. This static pressure drop, together with known air temperature and nozzle diameter, enables the calculation of the air mass flow rate through the system. The air mass flow rate through the nozzle is calculated from Kröger (2004),

$$m_{avm} = C_n A_n \sqrt{2\rho_n \Delta p_n} \tag{4.6.1}$$

where

C_n Discharge coefficient

A_n Nozzle cross section area

ρ_n Air density

Δp_n Static pressure drop

The discharge coefficient (C_n) depends on the Reynolds number of the air in the nozzle. Kröger (2004) gives relations for the discharge coefficient over different ranges of Reynolds number. For 30 000 < Re_n < 100 000 the discharge coefficient is given by,

$$C_n = 0.954803 + 6.37817 \times 10^{-7} Re_n - 4.65394 \times 10^{-12} Re_n^2 + 1.33514 \times 10^{-17} Re_n^3 \quad (4.6.2)$$

where Re_n is determined as,

$$Re_n = \frac{\rho_n v d_n}{\mu_n} \quad (4.6.3)$$

For 100 000< Re_n < 350 000, the discharge coefficient is calculated from,

$$C_n = 0.9758 + 1.08 \times 10^{-7} Re_n - 1.6 \times 10^{-13} Re_n^2 \quad (4.6.4)$$

and for Re_n > 350 000, the discharge coefficient is assumed as,

$$C_n = 0.994 \quad (4.6.5)$$

Two nozzle diameters (d_n) are implemented to measure the air mass flow rate through the system. The two diameters are used to keep the pressure drop across the nozzle in reasonable ranges for the calibrated pressure transducers. For lower air flow rates, air is directed through a nozzle with an internal diameter of 75 mm. For higher air flow rates, a nozzle with an internal diameter of 150 mm is used. The nozzle cross sectional area is calculated as,

$$A_n = \pi \frac{d_n^2}{4} \quad (4.6.6)$$

Air density is a function of the air temperature, measured at the wind tunnel inlet. With the temperature known, the density is calculated from fluid property equations which are presented in Appendix A.

4.6.3 Bundle air-side pressure drop

To characterise the air-side pressure drop over the bundle, the bundle needs to be isolated from the WDS. The pressure taps measuring the air pressure downstream from the bare tube bundle has to remain dry. This is achieved by placing the pressure taps above the WDS (P_{out} in Figure 4.6b). Care is taken to ensure that pressure taps remained normal to the direction of air flow to accurately measure static pressure. For the upstream pressure taps in experiment 3, an H-tap is used beneath the bottom row (under n_r = 1) by attaching it to a tube, in the centre of the bottom row. In order to isolate the pressure drop over the bare tube bundle (Δp_b) from the system pressure drop (Δp_{sys}), the air-side pressure drop over the WDS has to be characterised separately.

The air-side pressure drop over the WDS (Δp_{wds}) is correlated as a function of the air mass velocity and subtracted from Δp_{sys}, measured during experiments. Figure 4.7 displays how the pressure drop across the bare tube bundle is isolated from the water distribution system.

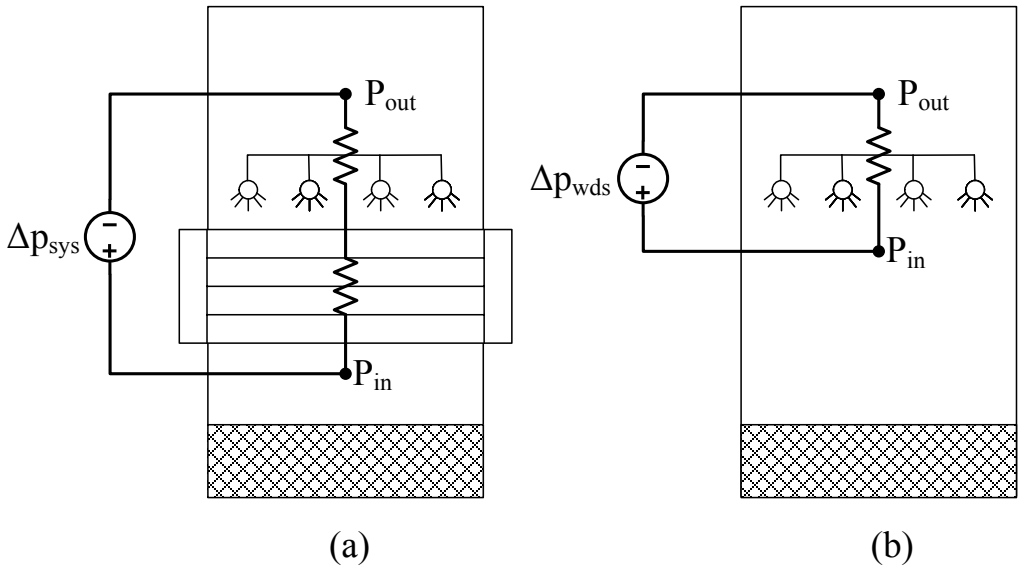

Figure 4.7: Measuring (a) system pressure drop and (b) water distribution system (WDS) pressure drop

The pressure drop over the bundle can be mathematically expressed as,

$$\Delta p_b = \Delta p_{sys} - \Delta p_{wds} \tag{4.6.7}$$

where the pressure drop over the water distribution system is calculated from a correlation developed from experimental data (refer to Subsection 4.8.1).

All air-side pressure drops are measured with Endress & Hauser ® pressure transducers. The calibration procedure for these pressure transducers is presented in Appendix C. Atmospheric pressure is recorded from a mercury barometer, installed in the heat transfer laboratory.

4.7 Experimental procedure

Before any experiments are conducted, the experimental apparatus and wind tunnel inlet are examined for openings that would allow for atmospheric air to enter the system at any locations other than the apparatus inlet. Any such leakage openings are sealed. The sump water level is checked and filled if necessary. The pump water filter is cleaned before each experiment. Once the test environment is declared safe, the data acquisition system is switched on and allowed to warm up in order to minimise measuring errors and pressure transducers are zeroed.

In essence, all experiments are conducted in a similar fashion. The experimental procedure for experiment 1 is presented with additions or changes added where the experimental procedures of experiments 2 or 3 deviated from that of experiment 1. The experimental procedures are carried out in the following sequence:

1. All sensors are set to recording mode.
2. The gate valve, controlling the deluge water flow rate, is slightly opened before the water pump is switched on. The gate valve is initially set to the lowest flow rate of 5 *l*/min or $\Gamma_{dw}/d_o = 0.47$ kg/sm^2.
3. The smaller nozzle in the wind tunnel which measured the air mass flow rate is opened.
4. As the change in the water temperature decreases over time through the bundle, and nears steady state, the radial fan is switched on and set to the minimum air flow velocity by adjusting the VSD to output 15 Hz to the radial fan.
5. Time is allowed for all temperatures and pressure measurements to reach a steady state. Temperature steady state is assumed when the change in consecutive measurements is smaller than 0.2 ºC, which corresponds to the measuring resolution of the thermocouple. The thermocouple temperatures are recorded for a minimum of 2 minutes at 10 second intervals. The average of these values are taken as the measured temperature for the current water and air flow rate setting.
6. The pressure transducers displayed 2 second averaged readings. The pressure drop across the apparatus and nozzle is taken as the mean value from a maximum and minimum value, captured over a 10 second period.
7. The water flow across the bundle is visually documented with a digital camera, capturing the water flow patterns from the front and sides of the bundle. Flow over the thermocouple measuring tips is additionally documented for experiment 2.
8. Once visual, temperature and pressure data are collected, the air flow rate over the bundle is increased by increasing the AC output frequency on the VSD by 3 Hz.
9. Steps 5 to 8 are repeated until the pressure drop over the smaller nozzle in the wind tunnel approached 500 Pa. When a pressure drop reading close to 500 Pa is observed over the smaller nozzle, the frequency on the VSD is decreased to 12 Hz, the small nozzle closed and the larger nozzle opened. This allows for a smooth transition in air flow rate across the bundle.
10. Steps 5 to 8 are again repeated, but the frequency on the VSD is adjusted by 2 Hz, instead of 3 Hz. This is done to compensate for the larger diameter nozzle.
11. As the air mass velocity across the bundle approaches 2.8 kg/sm^2 the VSD frequency is subsequently increased by 1 Hz at a time to allow the onset of critical flow to be accurately determined for the current water flow rate setting.
12. Once critical flow establishes, significant drop entrainment ensues. Swift documentation of the flow is required in order to minimise water leakage into the wind tunnel. Due to severe air and water turbulence across the bundle and the risk of water leakage, ample time for the temperatures to reach steady state

cannot be established. The pressure drop across the bundle is recorded similarly to Step 7 except it is over a time period of 5 seconds instead of 10.

13. After the pressure measurements are recorded, the data acquisition module is stopped and the data saved.
14. As the documentation is completed from Step 12, the VSD frequency is lowered to 5 Hz, the large nozzle closed and the smaller one opened inside the wind tunnel. The water flow rate is increased by 5 *l*/min to the next flow rate.
15. Steps 4 to 14 are repeated for water flow rates 10, 15 and 20 *l*/min. This translated into deluge water mass velocities (Γ_{dw}/d_o) of 0.95, 1.42 and 1.89 kg/sm^2.
16. For experiment 3, Steps 1 to 15 are repeated for bundles consisting of 8, 6, 4 and 2 bare tube rows, with the following exceptions:
    - The flow across the bundle is not visually documented.
    - From the results of experiment 1, the maximum air flow rate is chosen as 3 kg/sm^2 to exclude critical flow.
    - Dry operation tests are additionally conducted before wet operation under the same air flow rates.
17. For experiment 3, after each set of tests for a number of bare tube rows is completed, two consecutive tube rows are removed from the bundle housing structure. The tube holes in the housing structure are sealed off to keep atmospheric air from entering the test apparatus. The wood dowels, added to the sides of the bundle are removed in conjunction with their respective rows.

Atmospheric pressure inside the test facility is recorded on an hourly basis throughout the experimental procedure and assumed constant over a chosen water flow rate.

4.8 Results

4.8.1 Air-side pressure drop over the water distribution system

Before presenting the results for each experiment, the pressure drop across the WDS is determined in order to isolate the pressure drop measurements across the bare tube bundle from that measured over the system.

Figure 4.8 presents the pressure drop over the water distribution system under dry and wet operation for a water flow rate of Γ_{dw}/d_o = 0.95 kg/sm^2. A parabolic curve fit correlated the air-side pressure drop as a function of the air mass velocity.

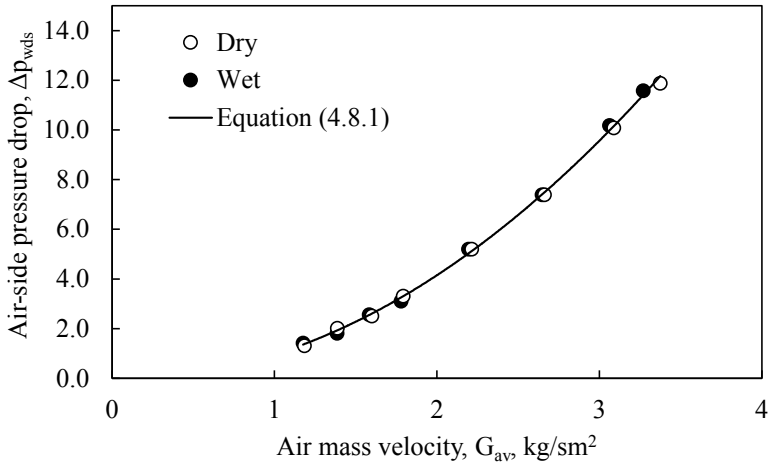

Figure 4.8: Pressure drop across water distribution system

The pressure drop across the water distribution system is not affected by the water flow rate and remained unchanged for wet and dry operation and is correlated as,

$$\Delta p_{wds} = 1.1135 G_{av}^2 - 0.1522 G_{av} \qquad (4.8.1)$$

with an absolute maximum error of 4.8 % and an average error of 2.3 % between the measured and correlated pressure drop values. The correlation for the WDS is valid over an air mass velocity range of $1.0 < G_{av} < 3.27$ kg/sm^2.

The air-side pressure drop across the bare tube bundle is isolated by employing equation (4.6.1) with Δp_{wds} as defined in equation (4.8.1).

4.8.2 Experiment 1

Experiment 1 investigates the critical air flow rates across the bare tube bundle and bundle wetting under different water and air flow rates.

Critical air flow investigation

Critical air flow is usually observed in the top tube row. In order to fully describe the critical air flow phenomenon, the development of the water film across the bare tube bundle as the air flow rate is increased will be described. Figure 4.9 presents the film development for a deluge water flow rate of $\Gamma_{dw} = 1.89$ kg/sm^2 as the air flow rate was sequentially increased. A schematic of the water flow from each photograph in Figure 4.9 is added to clarify what was visually observed.

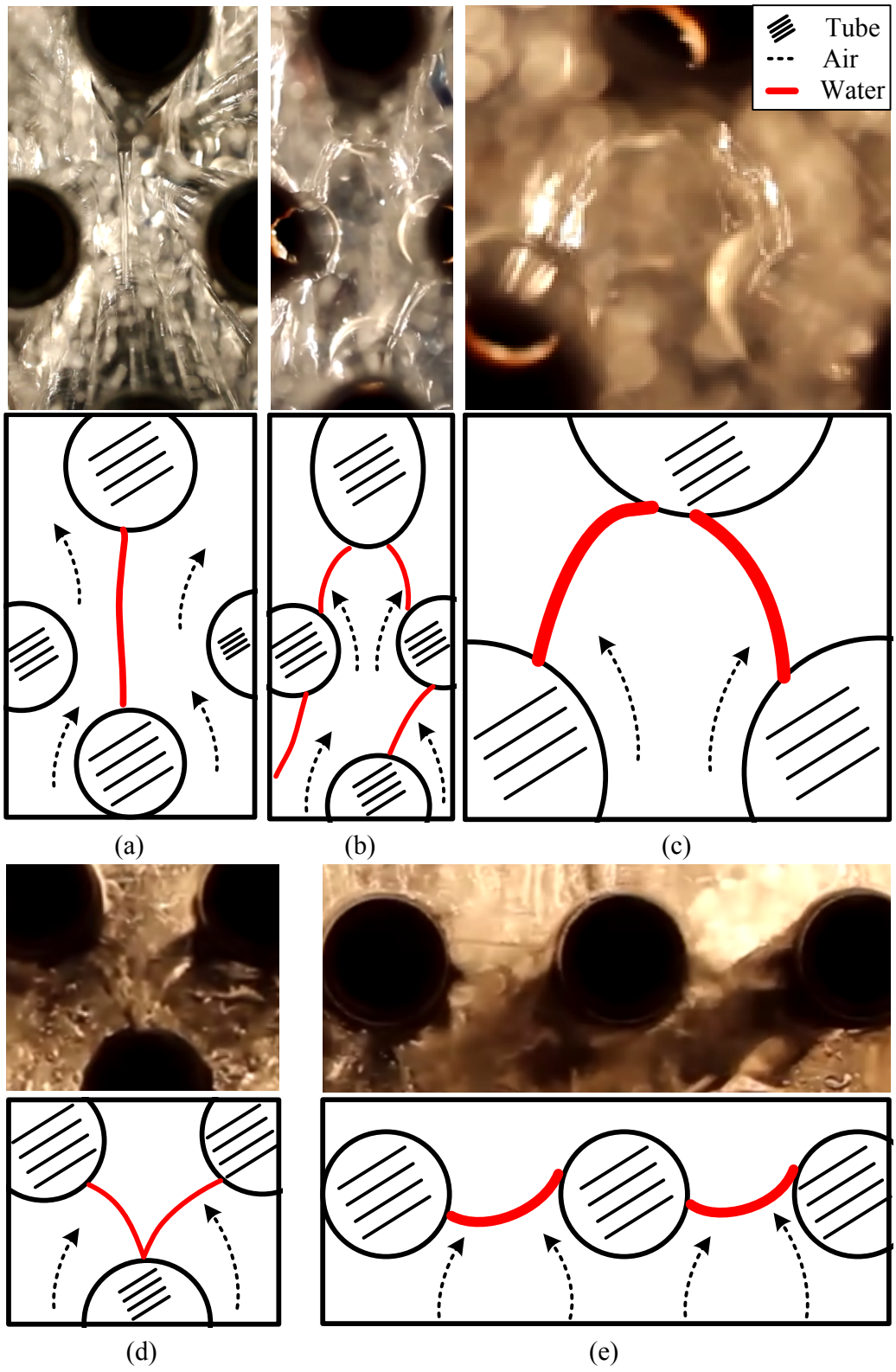

Figure 4.9: Deluge water film development for Γ_{dw} / d_o = 1.42 kg/sm^2. For an air flow rate of (a) G_{av} = 0.95 kg/sm^2, (b) G_{av} = 1.8 kg/sm^2, (c) G_{av} = 2.0 kg/sm^2, (d) G_{av} = 2.76 kg/sm^2 and (e) G_{av} = 3.02 kg/sm^2

Figure 4.9(a) displays a column of water flow typically observed under low air flow rates ($G_{av} < 1$ kg/sm^2). Column flow (continuous water stream) was observed for a water flow rate above $\Gamma_{dw}/d_o = 0.47$ kg/sm^2.

As the air flow increases, it arches the water columns upwards, redistributing water to closest neighbour tubes as in Figure 4.9(b) and Figure 4.9(c). As the air flow increases further, water arches merge to form webs as in Figure 4.9(d). These webs grow thicker and become suspended midway between tubes forming a fluid bed as in Figure 4.9(e). With a further increases in air flow, critical flow is established whereby the webs were pulled upwards passed the top tube row where webs broke up, water fell back down, and the web forming process is repeated.

Figure 4.10 presents the onset of critical air flow as a function of the deluge water mass velocity. This critical air mass velocity is correlated as a parabolic function of the deluge water mass velocity by,

$$G_{av(crit)} = -0.1351\left(\frac{\Gamma_{dw}}{d_o}\right)^2 + 0.2386\left(\frac{\Gamma_{dw}}{d_o}\right) + 3.2245 \qquad (4.8.2)$$

Equation (4.8.2) is valid for $0.47 < \Gamma_{dw}/d_o < 1.89$ kg/sm^2.

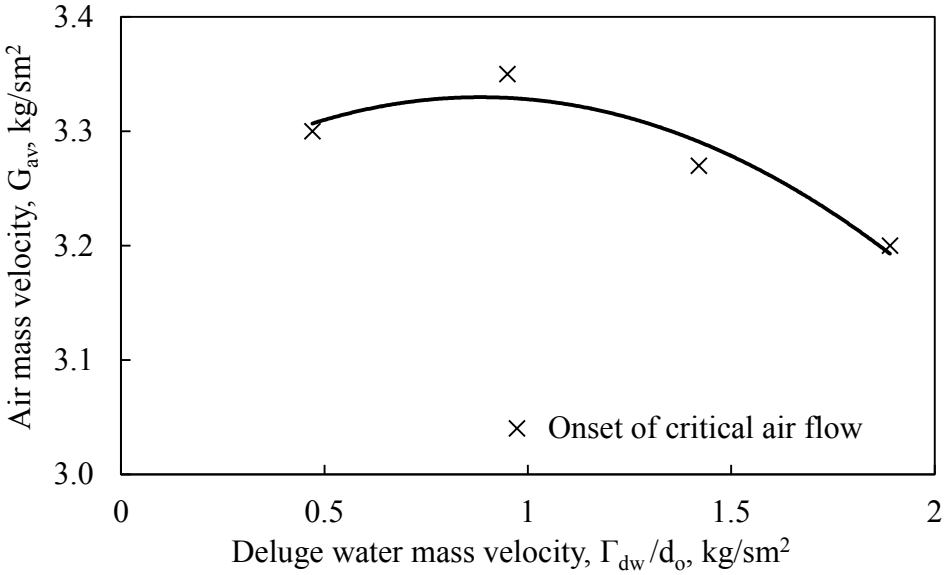

Figure 4.10: Onset of critical air flow for different water mass velocities

From Figure 4.10, for a water flow rate of $\Gamma_{dw}/d_o = 0.47$ kg/sm^2, with a low water flow rate, column flow does not establish at low air flow rates and subsequently no web and fluid bed formation is present. Instead, critical air flow is characterized by significant droplet entrainment in the air stream.

The onset of critical air flow decreases for an increase in water flow rate for water flow rates larger $\Gamma_{dw}/d_o = 0.95$ kg/sm^2. At $\Gamma_{dw}/d_o = 0.95$ kg/sm^2 column water flow initiates, which allows for the formation of webs between tubes at high air flow

rates. As the deluge water flow rate increases, the web thickness together with number webs formed between tubes in the top row increases. With the increase in webs, the gaps for air to travel through the top row decreases, resulting in further pressure losses across the bare tube bundle under critical air flow.

The fluid bed leads to temporary water retention inside the bundle as the majority of water followed the tube slope to the lower, back side of the bundle housing instead of falling through the bundle back into the sump. Figure 4.11 displays the air-side pressure drop over the 8 tube row bundle for different water flow rates over a range of air flow rates.

For high air flow rates (G_{av} > 3 kg/sm^2), a significant rise in air-side pressure drop is measured, confirming the increased pressure drop under critical flow as observed by Anderson (2014).

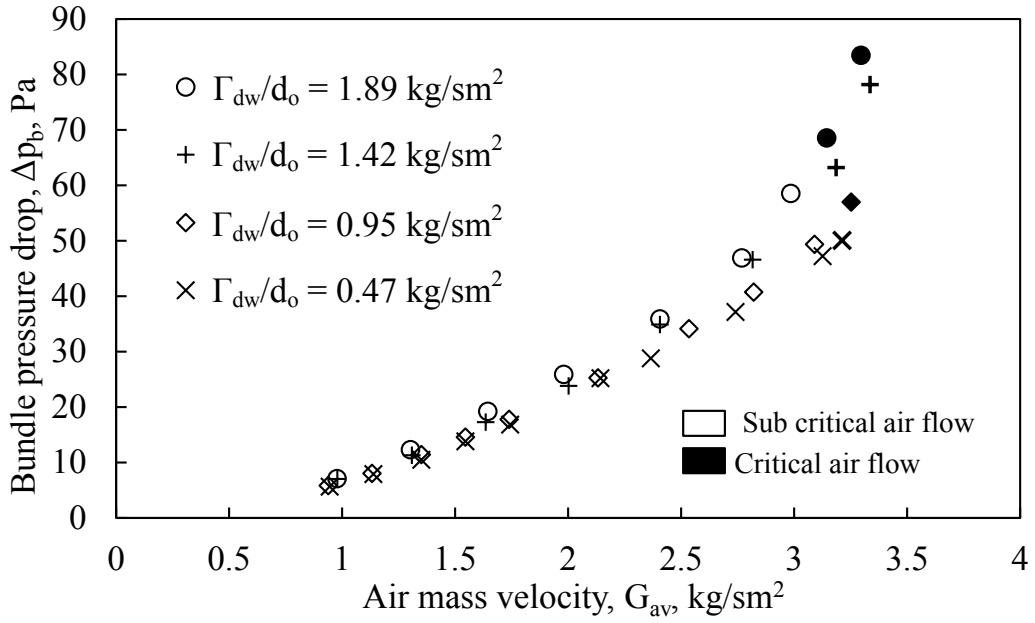

Figure 4.11: Pressure drop across bundle for different water flow rates

Bundle wetting investigation

Bundle wetting can be described by the fraction of total tube surface area wetted, under different air and water flow rate settings. The wetted area fraction is correlated as a parabolic function of the air mass velocity coupled with linear function of the deluge water mass velocity. The wetted area fraction is given by,

$$\frac{A_{wet}}{A_{tot}} = f_1 {G_{av}}^2 + f_2 G_{av} + 0.85 \qquad (4.8.3)$$

where

$$f_1 = 0.02293\left(\frac{\Gamma_{dw}}{d_o}\right) - 0.048389$$

$$f_2 = -0.021998\left(\frac{\Gamma_{dw}}{d_o}\right) + 0.041548$$

and is valid over $0.9 < G_{av} < 3.3$ kg/sm^2, and $0.47 < \Gamma_{dw}/d_o < 1.89$ kg/sm^2. The deviation between predicted data and measured data is presented in Figure 4.12. From Figure 4.12 the wetted tube area predicted by equation (4.8.3) is in good agreement with the measured values. Figure 4.13 presents an area ratio of the wetted area over the total tube area as a function of the air flow rate for different water flow rates.

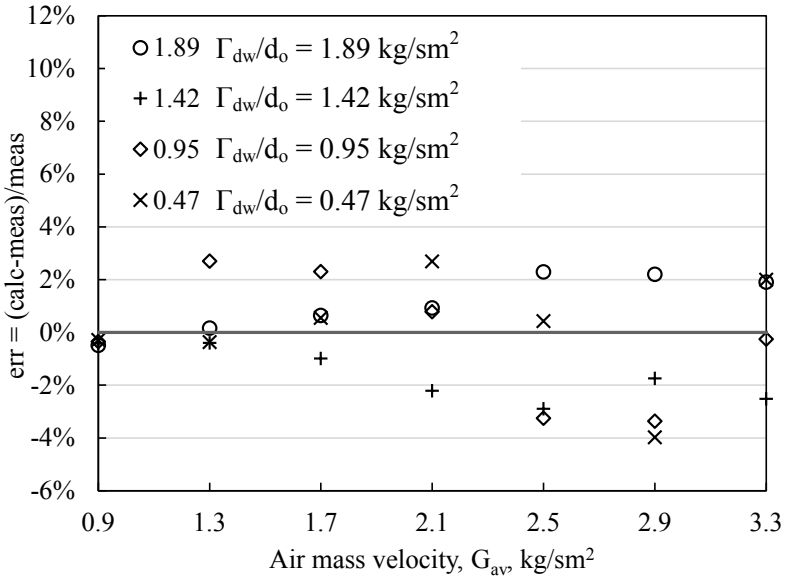

Figure 4.12: Deviation between measured and calculated wetted tube area.

The wetted tube area increased with an increase in the water flow rate, but decreased for an increase in the air flow rate. Critical air flow considerably reduced the wetted area for lower water flow rates (Γ_{dw}/d_o = 0.47 kg/sm^2 and Γ_{dw}/d_o = 0.95 kg/sm^2) and had a less prominent effect on the wetted area for higher water flow rates (Γ_{dw}/d_o = 1.42 kg/sm^2 and Γ_{dw}/d_o = 1.89 kg/sm^2). Dry-out areas were observed for low water flow rates coupled with high air flow rates.

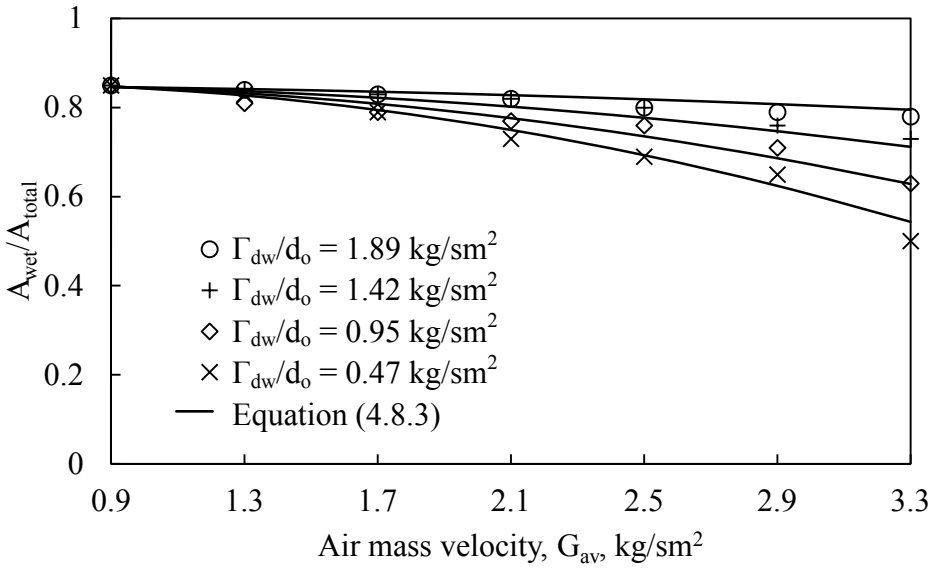

Figure 4.13: Bundle wetting for different air and water flow rates

Figure 4.14 shows how the water distribution, as viewed from the front, differed across the bundle under low and high air flow rates for a constant water flow rate. A water flow rate of Γ_{dw}/d_o = 1.42 kg/sm^2 is presented together with an air flow rate of G_{av} = 0.9 kg/sm^2 in Figure 4.14(a) and an air flow rate of G_{av} = 2.8 kg/sm^2 in Figure 4.14(b).

Little to no disturbance of the water columns were observed when a low air flow rate passed through the bundle. At a higher air flow rate, great air-water interaction was observed which led to good water distribution and wetting across the bare tube bundle.

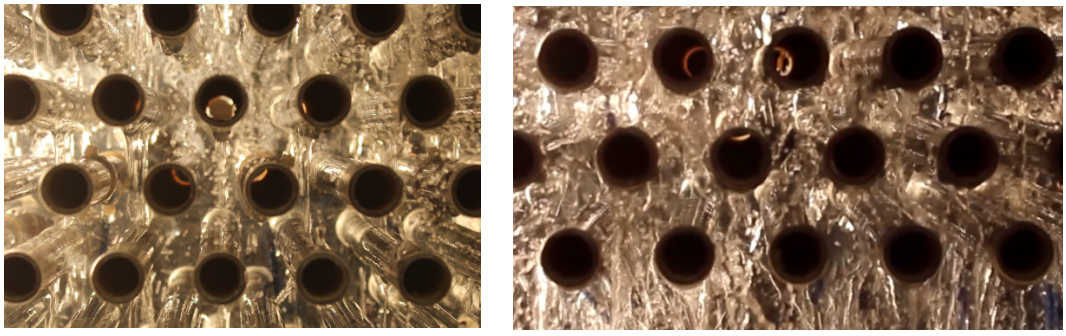

(a) (b)

Figure 4.14: Water distribution under (a) low air flow and (b) high air flow

The increased water-air interaction increased the air-side pressure drop significantly which translates into more fan power and thus more energy required for operation. Drop entrainment in the air stream will increase the amount of make-up water required and thus increase life cycle costs.

From the wetting investigation it is evident that critical air flow can increase the risk of dry-out inside the bundle, especially in lower tube rows. Water webs at the top of the bundle, suspended by air during the formation of a fluid bed, resulted in water drifting with the tube slope towards the back of the bundle and down the housing structure instead of through the bundle and back into the sump underneath the bundle. This had to effect that a section of the bundle was at risk of dry-out.

4.8.3 Experiment 2

Experiment 2 investigates two methods of attaching the thermocouples to the tubes in the bare tube bundle to ensure complete wetting of the measuring tip and decrease the uncertainty in deluge water temperature measurements throughout the bundle.

The thermocouples are attached by two methods as shown in Figure 4.5. The water flow over the measuring tip was documented at different water and air flow rate settings. Figure 4.15 shows the flow over the thermocouples for a water flow rate of $\Gamma_{dw}/d_o = 0.95$ kg/sm^2 and an air flow rate of $G_{av} = 2.3$ kg/sm^2 for both attachment methods.

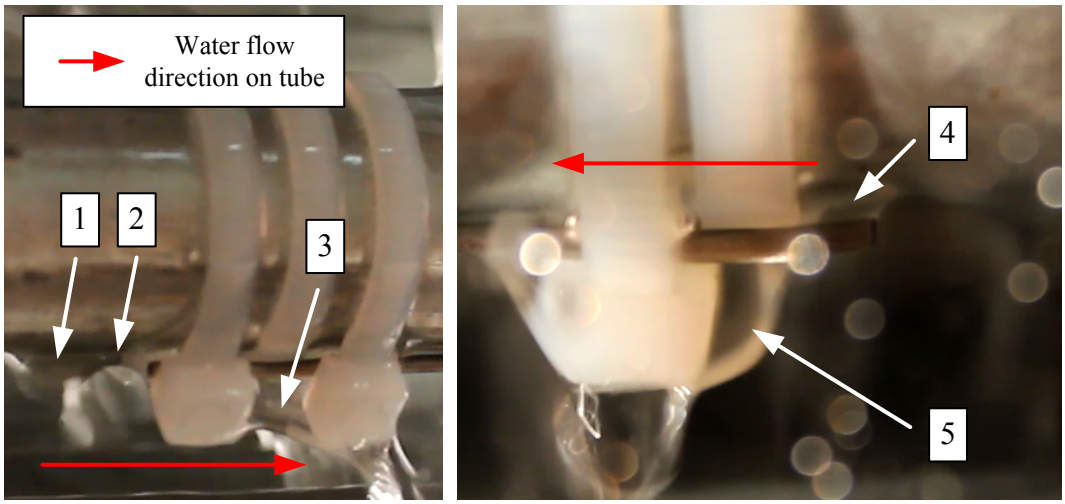

(a) (b)

Figure 4.15: Flow around thermocouples with (a) 1st attachment method and (b) 2nd attachment method.

With reference to Figure 4.15(a): a drop is seen to be forming before the thermocouple at (1). This drop is pulled over the measuring tip at (2), which subsequently remains wet due to the surface tension forces between the zip tie and the tube surface. The water is then expelled between the zip ties at (3).

At lower water flow rates, smaller drops form at (1) and the water droplet brakes off closer to the first zip tie at (3). At the high water flow rates, water will continuously move over the measuring tip and in some cases a column is formed between the zip ties at (3).

With reference to Figure 4.15(b): a neck forms at (4) and due to surface tension, a very thin water film keeps the measuring tip wet. A droplet would form at (5) and break off at the cable-tie to the left. At a lower water low rate, the droplet forming at (5) would be smaller and break off earlier compared to that in Figure 4.15(b).

Critical air flow together with low water flow rates posed the biggest risk for dry thermocouples measuring tips. As stated earlier, under critical air flow, water was diverted to the back of the bundle and less water fell through the bundle. This increases the risk for the thermocouple measuring tips to become dry.

Figure 4.16 presents the measured water temperatures through the bare tube bundle for a water flow rate of Γ_{dw}/d_o = 1.42 kg/sm^2 at an air flow rate of G_{av} = 2.3 kg/sm^2. The thermocouple positions through the bundle are presented in Figure 4.6 (a).

From Figure 4.16, the water temperature decreased as the water fell through the bundle. T_1 was attached to the top row and measured the highest water temperature. This was followed by T_2 and T_3.

T_1 was attached with the first attachment method (presented in Figure 4.5a) and displayed the best measurement certainty with a 0.13 ºC deviation. T_2 and T_3 were attached with the second attachment method and showed a 0.33 ºC and 0.32 ºC deviation respectively.

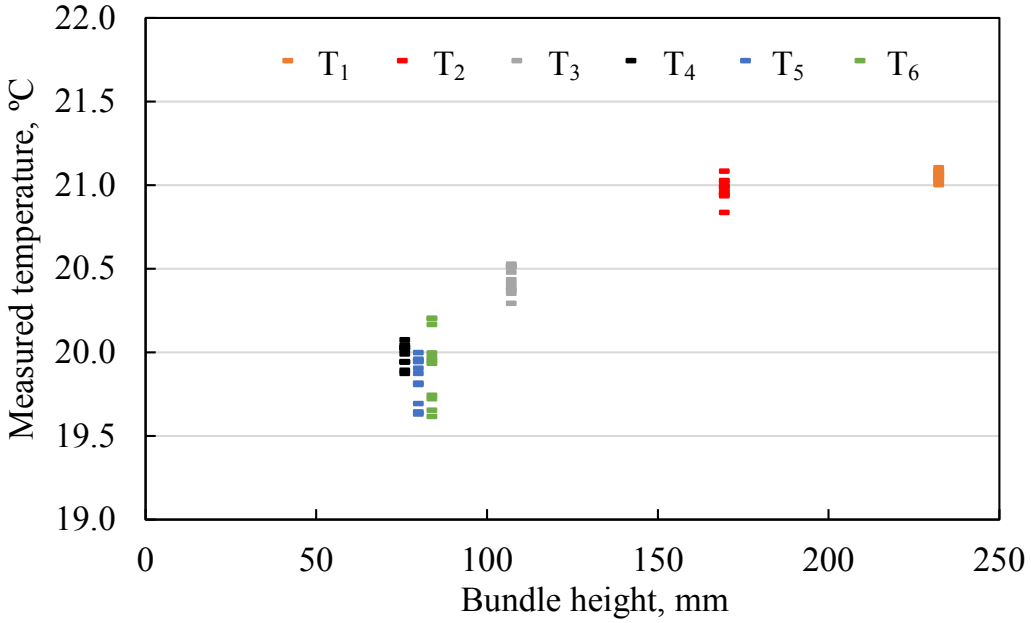

Figure 4.16: Measured temperatures with average values

Thermocouples T_5 and T_4 showed measuring deviations of 0.4 ºC and 0.23 ºC respectively, followed by T_6, which showed the largest measuring deviation of 1.5 ºC. Thermocouples T_4 to T_6 were placed horizontally in the lower part of the bundle and attached by the first attachment method. These thermocouples were the

most susceptible to dry-out due to (1) their position in the lower part of the bundle, where dry-out is most likely to occur at high air flow rates, and (2) they were not in-line with top tube row, which directly received water from the water distribution system.

Thermocouples T_4, T_5 and T_6 show good agreement as their average values are within 0.3 ºC and they are located at the same height next to each other but experienced dry-out for a water flow rate of Γ_{dw}/d_o = 0.47 kg/sm^2 under critical air flow.

Based on the results shown in Figure 4.14, it is recommended that the first attachment method be incorporated when measuring the deluge water temperature profile through a bare tube bundle. Although this requires more zip ties, it ensures that the thermocouple measuring tip remains wet and the temperature measured is reflective of the water temperature flowing over the tubes.

4.8.4 Experiment 3

Experiment 3 investigates the air-side pressure drop over the bare tube bundle under wet and dry operation over a range of water and air flow rate settings for a number of tube rows present in the bundle.

The bundle initially consists out of 8 tube rows with either 8 or 7 tubes per row. The air flow rate is varied between G_{av} = 1.0 kg/sm^2 and G_{av} = 3.0 kg/sm^2 for each water flow rate. A dry test is done before wet tests to investigate the influence of the water present in the bundle on the air-side pressure drop. The water flow rate is varied between of Γ_{dw}/d_o = 0.47 kg/sm^2 and Γ_{dw}/d_o = 1.89 kg/sm^2. The experiment is repeated for a bare tube bundle consisting out of 8, 6, 4 and 2 tube rows.

Care is taken to avoid critical air flow, as this will influence the pressure drop stability over the bundle and decrease repeatability of the experiment due to the unstable nature of critical air flow through the bundle.

As stated in the experimental procedure in Section 4.7, air flow and water flow rates together with the number of tubes present in the bundle were the independent variables for experiment 3. By controlling these variables, the air-side pressure drop across the bare tube bundle is measured and correlated as a compound power function of these independent variables.

The correlations presented for the pressure drop are generated by multiple linear regression analysis. The air-side pressure drop correlation across the bare tube bundle under wet operation is given as,

$$\Delta p_{b(w)} = 1.13921\, G_{av}^{1.80216} n_r^{0.83805} \left(\frac{\Gamma_{dw}}{d_o}\right)^{0.18857} \tag{4.8.4}$$

Figure 4.17 presents the air-side pressure drop as a function of the air mass velocity, deluge water mass velocity and number of tube rows present in the bundle.

Equation (4.8.4) is shown to predict the measured pressure drop to an acceptable degree in Figure 4.18 with the majority of the air-side pressure loss measurements to within ±10 % of their actual value. Only 4 out of 139 measurements fell outside this range.

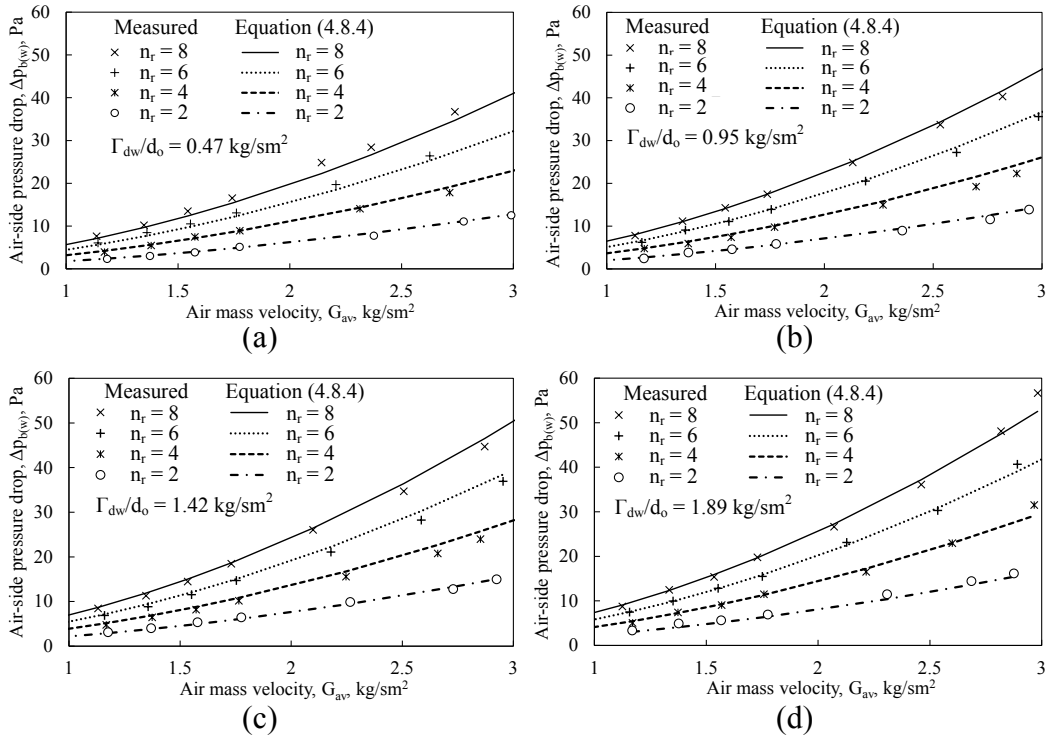

Figure 4.17: Air-side pressure drop for wet operation.

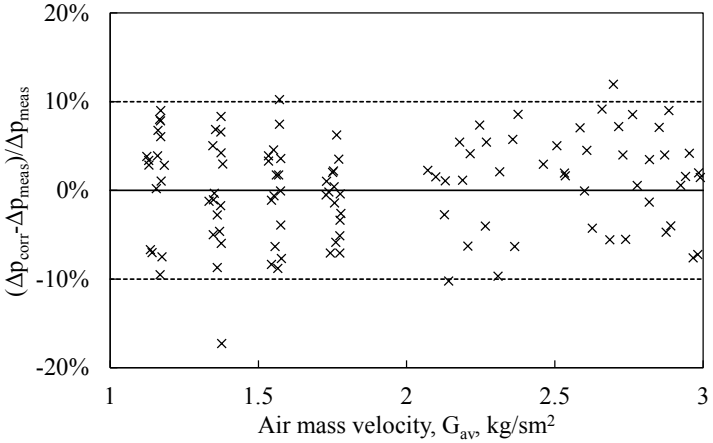

Figure 4.18: Prediction accuracy for wet operation pressure drop

For the dry operation, the air-side pressure drop across the bundle is correlated in a similar fashion to wet operation and is given by,

$$\Delta p_{b(d)} = 0.77394\, G_{av}^{1.83830} n_r^{0.95061} \qquad (4.8.5)$$

Figure 4.19(a) presents the pressure drop for dry operation as a function of the air mass velocity for a different number of tube rows present in the bundle. Figure 4.19(b) presents the accuracy with which equation (4.8.5) predicted the measured value, to within ± 5 % for the majority of measured points. Two of the 23 measured pressure drops fell outside the ± 5 % predicted range

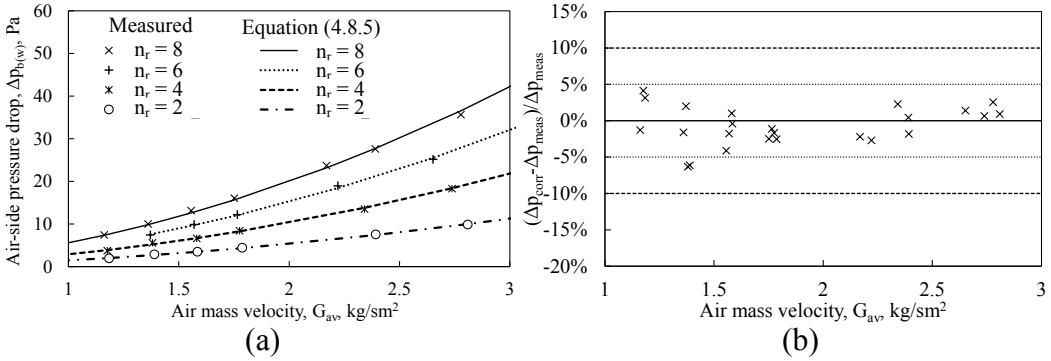

Figure 4.19: Air-side pressure drop for dry operation

From equations (4.8.4) and (4.8.5), it is evident that the pressure drop across the bare tube bundle is mostly influenced by the air flow rate followed by the number of tube rows (from their respective power magnitudes). Under wet operation, water flow rate has a relatively small effect on the pressure drop across the bundle.

The air-side pressure drop for wet operation, calculated with equation (4.8.4) and for dry operation, calculated with equation (4.8.5) are compared in Figure 4.20 for a bundle with eight tube rows.

From Figure 4.20 one can see the effect wet operation has on the air-side pressure drop across the bare tube bundle compared to dry operation. Further, by increasing the water flow rate, a noticeable but small increase in the pressure drop is observed. Figure 4.21 compares the correlations for air-side pressure drop under wet and dry operation to that from literature.

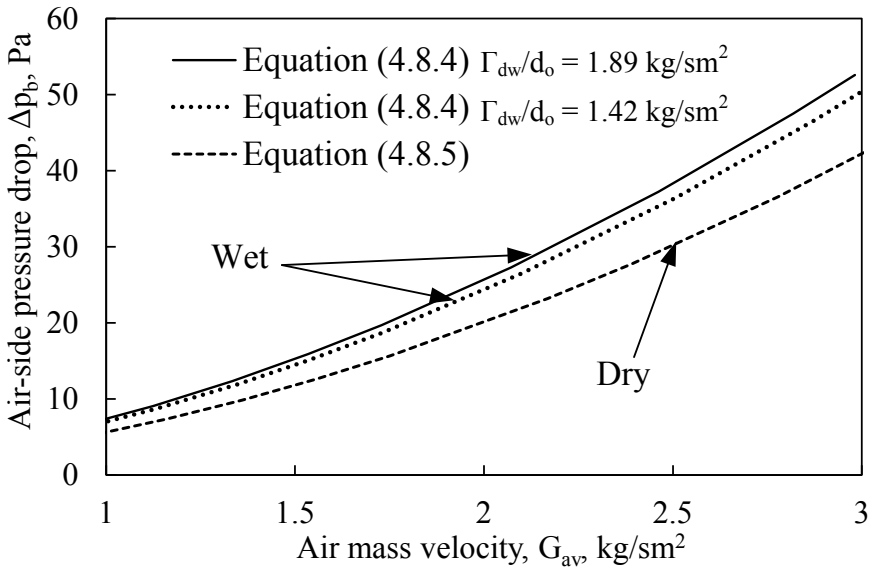

Figure 4.20: Air-side pressure drop comparison between wet and dry operation

Reuter and Anderson (2016) over predicted the air-side pressure drop under wet operation and under predicted it under dry operation. Gaddis and Gnielinski (1985) under predicted the air-side pressure drop under dry operation.

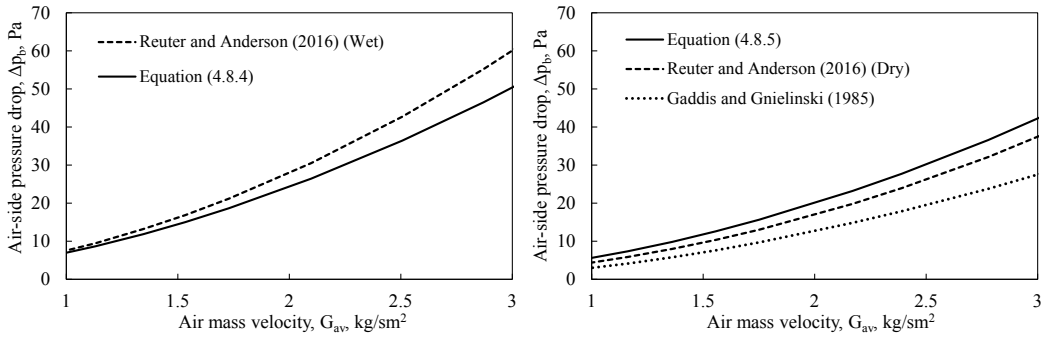

(a) (b)

Figure 4.21: Pressure drop comparison with literature for (a) wet operation and (b) dry operation

4.9 Discussion of results and recommendations.

Experiment 1 shows that critical air flow is established around an air mass velocity of G_{av} = 3.2 kg/sm^2 regardless of the water flow rate, which is higher compared to G_{av} = 2.8 kg/sm^2 made by Anderson (2014). Dry-out inside the bundle is observed for a water flow rate of Γ_{dw}/d_o = 0.47 kg/sm^2 under critical air flow conditions.

In general, critical air flow leads to a reduction in total bundle wetting as presented in Figure 4.13, although better mixing is observed in the upper part of the bundle.

From these observations, it is proposed that an air mass velocity of no higher than G_{av} = 3.0 kg/sm^2 be employed for a bare tube bundle under wet operation to avoid critical air flow. Care should be exercised when the bundle is installed at a slope as this could lead to dry-out areas which will negatively influence the heat transfer performance.

From experiment 2 it is found that attaching the thermocouple with four zip ties (first attachment method), ensures the measuring tip remains wet during tests. It is advised that if a bundle with a slope to one side is tested, the thermocouples be placed as close as possible to the back of the bundle housing to minimise the risk of measuring tip dry-out.

Experiment 3 investigates the air-side pressure drop across the bare tube bundle. From equations (4.8.4) and (4.8.5), it can be concluded that the air flow rate primarily determines the air-side pressure drop followed by the number of tube rows present inside the bundle and the water flow rate for wet operation.

From these three experiments it is concluded that one should refrain from operating at low water flow rates coupled with high air flow rates. To maximise the wetted tube area, a water flow rate of Γ_{dw}/d_o = 1.89 kg/sm^2 is recommended, together with an air flow rate, lower than G_{av} = 3.0 kg/sm^2. Air flow rates above G_{av} = 3.0 kg/sm^2 would lead to dry-out areas inside the bundle, excessive pressure drops across the bundle and increased life cycle costs arising from increased water usage and increased required fan power.

In a real life application of a bare tube cooler, hot process fluid will be cooled with deluge water and the ambient air. The tube surfaces will be hotter than they were during these experiments and dry-out through the bundle would be more frequent.

In order to heat the tube surface, process distribution headers would be required to transport hot water from one tube row to the next and as such, visually obstruct investigation of the deluge water film over the tubes. In order to investigate the film flow of the deluge water through the bare tube bundle, hot process fluid, flowing through the tubes were sacrificed.

The pressure drop across the bundle is insensitive to water flow rates and as such, little change is expected in the pressure drop due to the change in water properties if the tubes were to be heated.

5. PERFORMANCE MODELLING OF THE HYBRID (DRY/WET) COOLING SYSTEM

5.1 Introduction

This chapter presents the performance model for the hybrid (dry/wet) cooling system (HDWCS). A parametric investigation is presented where the size of the bare tube bundle is optimized to serve as a performance booster. Further, performance charts are developed to present the potential gain in heat transfer rate under different air conditions for a range of ambient dry bulb temperatures. This chapter concludes with recommendations on the bare tube bundle dimensions for optimal heat transfer performance.

5.2 System description and design

5.2.1 Description

The HDWCS is a two stage hybrid air-cooling system, as introduced in Chapter 1. The first stage consists of two dry finned tube bundles and the second stage consists of one hybrid bare tube bundle.

The HDWCS is a series process flow, parallel air flow system. The process medium flows sequentially through the cooling system, entering the system at the first stage and leaving at the second stage, while ambient air is drawn over both stages by axial draft fans, located on top of the HDWCS.

5.2.2 Design and operation

The design of the HDWCS is based on a conventional air-cooled, finned tube cooling system that consists of two finned tube bundles arranged in a V-shape.

V-shaped finned tube bundles are mostly used in fluid compression (air conditioning and refrigeration) systems to condense the working fluid before it is passed through an expansion valve. External fins increase the heat transfer rate by providing additional external heat transfer surface area.

Dry cooled systems become very inefficient when the temperature difference between ambient dry bulb air and the working fluid approaches zero. By combining an air-cooled and evaporative cooler into a hybrid cooling system, it is possible to draw on the advantages of both dry and wet cooling systems. This is achieved by employing dry cooling during cold periods and evaporative cooling during hot periods, thus minimizing water usage relative to all-wet systems and increasing heat transfer performance relative to all-dry systems when required.

The HDWCS was divided into a two stage cooling system. The first stage, with two finned tube bundles, remains dry while the second stage, with a bare tube bundle, can operate either dry or wet. The bare tube bundle is less prone to bio-fouling and corrosion. Figure 5.1 presents an isometric section view of the HDWCS.

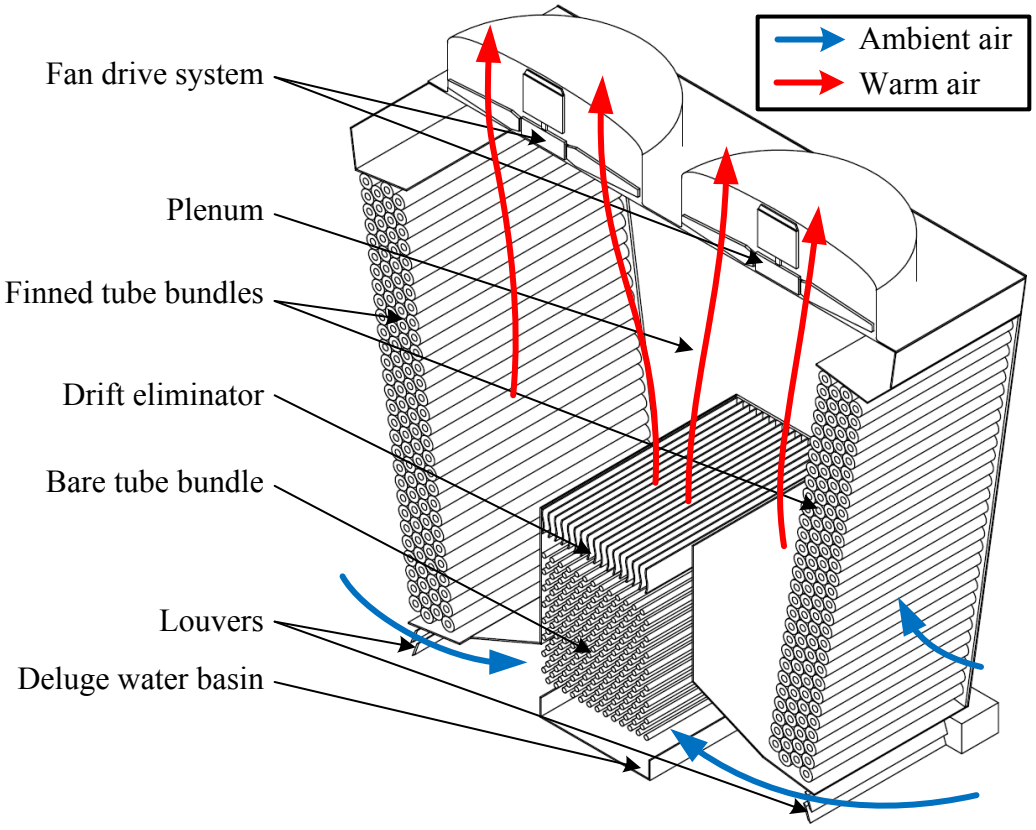

Figure 5.1: Isometric section view of the HDWCS

The layout of the system is chosen as presented in Figure 5.1 to minimise plume formation during wet operation and to ease retro fitment of conventional air-cooled systems with a hybrid bare tube bundle. For piping connections see Figure 1.6.

Plume abatement under wet operation is achieved by mixing the hot, dry air expelled from the first stage with the saturated air expelled from the second stage. These air streams mix in the plenum chamber before travelling through the axial fans into the surrounding environment.

To achieve sufficient air flow through the second stage, louvers are fitted below the finned tube bundles. The louvers can control the amount of air entering the second stage by acting as a variable air flow resistance in order to avoid critical air flow during wet operation.

Air is drawn in parallel over the first and second stages. Sensible heat is transferred by convection from the first stage to the air as well from the second stage when under dry operation. Under wet operation, heat is transferred from the bare tube bundle to the air stream by mass and heat transfer.

5.3 Numerical model

The theory and formulas concerning the dry and wet operation of the HDWCS were presented in Chapter 3. In the following subsections, this information is used to calculate the performance of the HDWCS under dry and wet operation for a set of given parameters.

The air-side heat transfer coefficients for dry operation, and the mass and heat transfer coefficients for wet operation, were employed in their respective sections of the model as set out in Chapter 3. The integral model was employed to calculate the heat transfer performance for the bare tube bundle.

5.3.1 Input parameters

The numerical model calculates the outlet conditions for each stage based on the input data from Table 5.1

Table 5.1: Input data

Description	Symbol	Value	Unit
Process medium inlet temperature	T_{pi}	38	ºC
Ambient air dry bulb temperature	T_{ai}	32	ºC
Relative humidity	RH	60	%
Atmospheric pressure	P_{atm}	101325	Pa
Process medium mass flow rate	m_p	85.2	kg/s
Deluge water mass velocity	Γ_{dw}/d_o	1.89	kg/sm^2
Air mass velocity over finned tube bundle (HDWCS under dry operation)	$G_{av\,fin(dry)}$	2.5	kg/sm^2

The process medium inlet conditions were chosen similar to that of a conventional air-cooled heat exchanger. The ambient conditions are representative of a typical summer's day. The deluge water flow rate is that determined from the experimental results presented in Chapter 4. The air mass velocity over the finned bundle was chosen to deliver an acceptable pressure drop across the first stage for 810 mm axial fans.

5.3.2 Calculation Procedure

The model calculation procedure follows the process medium travel path, first calculating the heat transfer rate in the first stage followed by that in the second stage. The air mass flow rate through the second stage is adjusted to deliver the

same air-side pressure drop as calculated over the first stage, which is necessary for a parallel air flow system. If the pressure drop over each stage is not equal, air flow will accelerate through the stage with the lowest pressure drop which will cause the pressure drop, for that stage, to increase. An equilibrium point will eventually form where the pressure drop over each stage is equal.

When the HDWCS operates wet, the combined first and second stage air flow rate is calculated based on the flow power for dry operation. Figure 5.2 presents the calculation procedure to solve the system fan power for wet and dry operation.

5.3.3 Dry operation

First stage

Hot process fluid enters the HDWCS at the finned tube bundles with the inlet temperature (T_{pi}) given in Table 5.1. Employing internal and air-side heat transfer coefficients (equations 2.3.5 and 2.3.7) and requiring that the heat lost by the process medium be equal that received by the air stream, the heat transfer rate, outlet process medium temperature and outlet air temperature are calculated for the first stage with equations (3.5.1), (3.5.2), (3.5.5), (3.5.6) and (3.6.1).

Ambient air is drawn through the finned tube bundles at the given air mass velocity (G_{av}) from Table 5.1 for dry operation. Using the pressure drop correlation (equation 2.3.8), the pressure drop over the first stage is calculated and the dry operation pressure drop for the system is established.

Second stage

The process medium enters the second stage with the temperature calculated for the outlet of the first stage. It is assumed no heat is lost to the environment between the two stages. Employing equations (2.3.5) and (2.3.9) for the internal and air-side heat transfer coefficients, the outlet process medium and outlet air temperatures together with the heat transfer rate for the second stage are calculated with equations (3.5.1) to (3.5.6).

The system pressure drop for dry operation is established by the first stage with the given air mass velocity from Table 5.1. Employing equations (2.3.10) and (3.2.14), and setting the air-side pressure drop for the bare bundle equal to that over the first stage, the air flow rate through the second stage is solved iteratively (starting with an air mass velocity similar to that for the first stage).

From the air flow rate, solved through each stage, the total air flow rate and flow power is calculated for the HDWCS under dry operation.

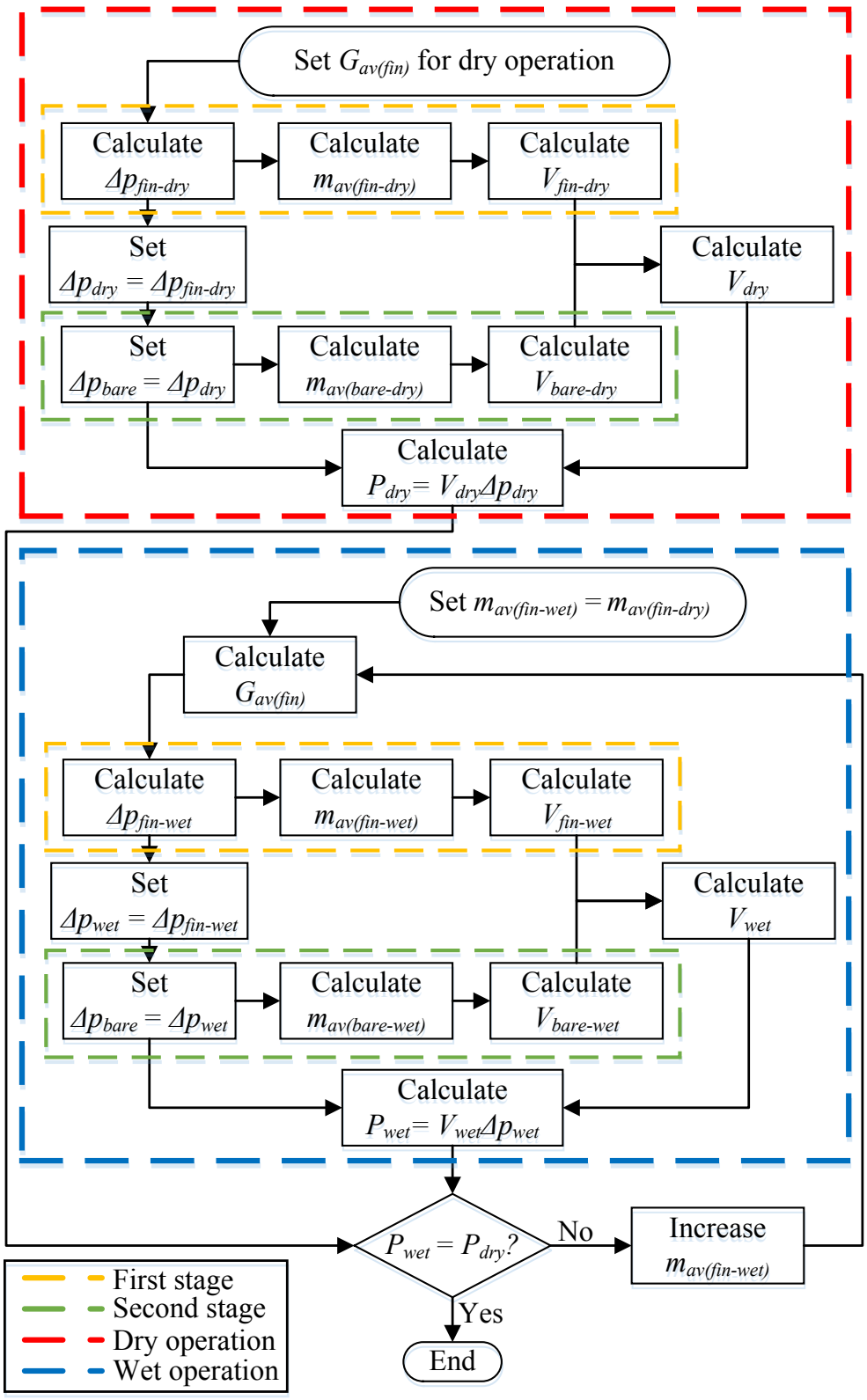

Figure 5.2: Calculation procedure for system fan power under dry and wet operation.

5.3.4 Wet operation

First stage

The first stage of the HDWCS always operates dry, but at a different operating point due to the change in the loss coefficient for the second stage under wet operation. The heat transfer and outlet temperatures of the working fluids in the first stage are calculated as described in Subsection 5.3.3 since the first stage remains dry.

An iterative procedure is followed by initially setting the air flow rate for through the first stage equal to that solved for dry operation, thereby establishing an initial system pressure drop under wet operation.

The pressure drop over the second stage, under wet operation, is calculated and compared to that calculated over the first stage. The air flow rate through the second stage is subsequently adjusted with the difference in pressure loss.

With equal pressure drops over the first and second stages, the volumetric air flow and flow power is calculated. These are compared to that calculated for the dry operation, and the initial air flow rate through the first stage is subsequently adjusted and the process is repeated until the wet and dry flow powers converge.

Second stage

Under wet operation, the bare tube bundle is deluged with water which enhances the heat transfer rate. Mass and heat transfer coefficients (equations 2.3.11 and 2.3.12) for wet operation are employed together with the general heat exchanger equation (3.2.9) in order to solve the heat transfer rate, process medium outlet temperature and mean deluge water temperature.

The air-side pressure drop over the bare tube bundle increased under wet operation due to the presence of water decreasing the area for air to move through. In addition to this, more water droplets interact with the air causing a further increase in pressure drop. The pressure drop over the second stage under wet operation is calculated from the correlation suggested by Reuter and Anderson (2016) (equation 2.3.15). The system pressure drop and flow power under wet operation is calculated as discussed in the previous subsection.

5.3.5 Conventional air-cooled system

The conventional air-cooled system is assumed to preside over the same finned tube bundles present in the HDWCS. The heat transfer rate, process medium outlet temperature and air temperatures are calculated in the same fashion as for the first stage of the HDWCS.

Figure 5.3 presents the calculation procedure for a conventional air-cooled system based on the flow power calculated from the HDWCS in Sections 5.3.3 and 5.3.4.

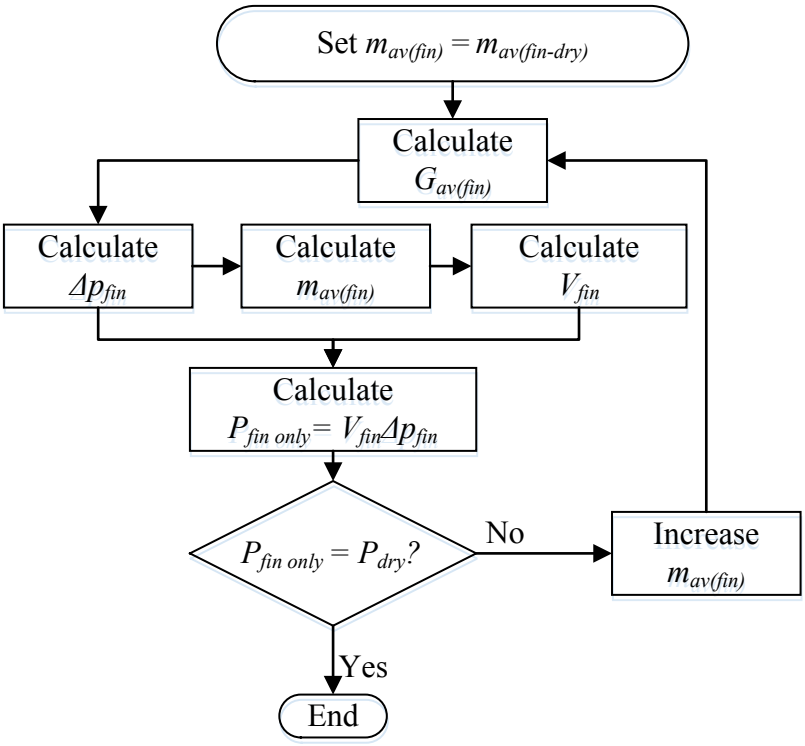

Figure 5.3: Calculation procedure for a conventional air-cooled system

5.4 Parametric study

A parametric study is undertaken in order to determine the optimal bare tube bundle size for it to act as a performance booster during unfavourable ambient conditions for a dry cooling system. The smaller the bare tube bundle, the wider the possibility for retro-fitting becomes. The aim of this parametric study is to determine the smallest bare tube bundle size with a tube diameter of d_o = 19 mm and a triangular pitch of $2d_o$ to deliver more than a 150% boost at an air relative humidity (RH) of 50%.

5.4.1 Base design case

The finned tube bundle dimensions remains the same for all cases during this investigation. The finned tube bundles geometric data is set out in Table 5.2. The initial design case consisted of a single pass bare tube bundle with 16 tube rows with 13 tubes per row. This resulted in a square, 500 mm by 500 mm bundle (width by height). The remaining bare tube bundle dimensions are given in Table 5.3.

Table 5.2: Finned tube bundle geometric data

Description	Symbol	Value	Unit
Fin parameters			
Thermal conductivity	k_f	204	W/mK
Fin diameter	d_f	57.2	mm
Fin root diameter	d_r	27.6	mm
Fin tip thickness	t_{ft}	0.25	mm
Fin thickness (mean)	t_f	0.5	mm
Fin root thickness	t_{fr}	0.75	mm
Fin pitch	P_f	2.8	mm
Finned tube bundle parameters			
Bundle width	W_f	0.2	m
Bundle length	L_f	10	m
Bundle height	L_{fi}	2.4	m
Thermal conductivity	k_t	50	W/mK
Tube outside diameter	d_o	25.4	mm
Tube inside diameter	d_i	21.6	mm
Mean thermal contact resistance	R_c	$4x10^{-4}$	m^2K/W
Number of tube rows	n_r	6	
Number of tubes per row	n_{tr}	41	
Number of passes	n_p	6	
Transverse tube pitch	P_t	58	mm
Longitudinal tube pitch	P_l	50.22	mm
Effective tube length (per pass)	L_t	10	m

Table 5.3: Bare tube bundle geometric data

Description	Symbol	Value	Unit
Bundle Length	L_b	10	m
Tube thermal conductivity	k_t	45	W/mK
Effective length of tube	L_t	10	m
Transverse tube pitch	P_t	38.0	mm
Lateral tube pitch	P_l	32	mm
Outer tube diameter	d_o	19.1	mm
Tube wall thickness	t_t	1.6	mm

5.4.2 Parameter identification

The bare tube bundle dimensions are limited by the space available between the finned tube bundles. Based on a design currently used in industry, the maximum width of the bare tube bundle is set at 800 mm to minimise the bare tube bundle's influence on air exiting the finned tube bundles. No explicit limit is placed on the

maximum height of the bare tube bundle, but Anderson (2014) notes that bundles with more than 25 tube rows lead to excessive air-side pressure losses. Thus the bundle width is limited to 800 mm and the height to 25 tube rows.

Firstly, the number of tube rows are investigated. The number of tube rows are sequentially increased from 16 to 25 tube rows (height of between 610 mm and 842 mm) for a width of 13 tubes per row (500 mm). By increasing the number of tube rows, the air-side pressure drop increases as observed from the experimental results in Chapter 4. The effect of changing the number of tube rows on heat transfer rate is presented in Figure 5.4. The y-axis for Figure 5.4 and Figure 5.5 compares the heat transfer rate, at a constant flow power, for the HDWCS to a conventional air-cooled system with finned tube bundles only.

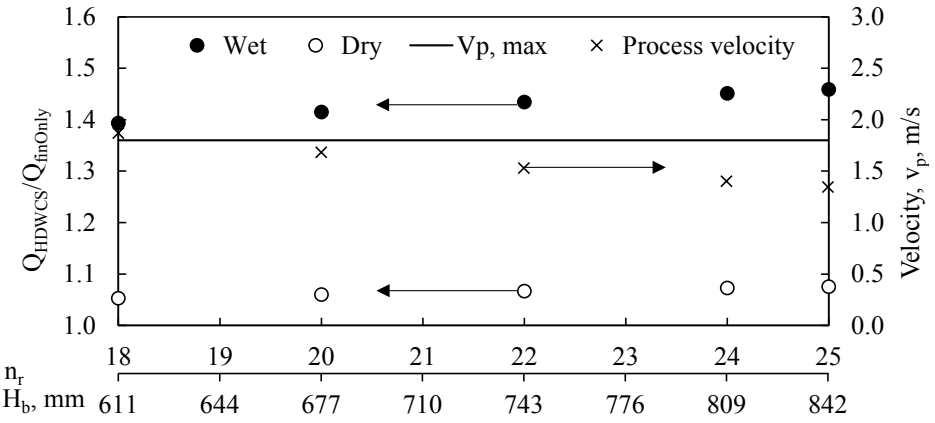

Figure 5.4: Heat transfer ratio as a function of the bundle height (H_b)

Secondly, the width of the bundle is investigated by sequentially increasing the number of tubes per row from 13 to 26 tubes (change in width from 500 mm to 1 m) for a bare tube bundle of 16 tube rows. This leads to an increase in air flow without affecting the air-side pressure drop over the bundle. The effect of changing the number of tubes per row on heat transfer rate is presented in Figure 5.5.

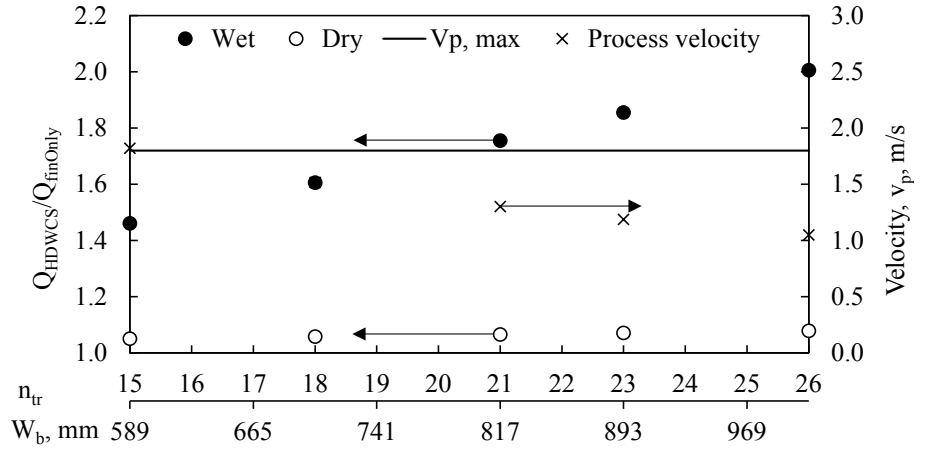

Figure 5.5: Heat transfer ratio as a function of the bundle width (W_b)

Kröger (2004) suggests the velocity of the process medium through the bare tube bundle remain between 1.5 m/s and 1.8 m/s. This is to avoid low heat transfer rates at low velocities (due to a low Reynolds number) and vibrations due to high turbulence at high velocities. The initial case does not meet this criteria, with 16 tube rows producing a process medium velocity of 2.1 m/s, higher than 1.8 m/s.

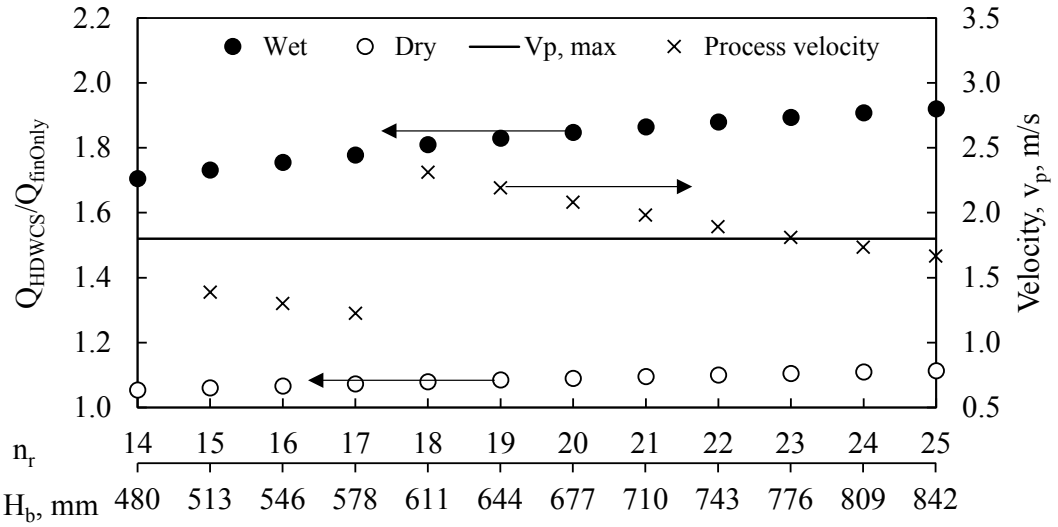

Figure 5.6: Heat transfer ratio for a bundle width of 21 tubes per row

Figure 5.6 presents the heat transfer rate for a bundle of 21 tubes per row (width of 817 mm). The width is chosen as the maximum allowable width predetermined due to the space available between the finned tube bundles. The greater the width, the lower the pressure drop (due to less tube rows) for a set air flow rate and the better the heat transfer performance for the system.

The height of 24 tube rows produces a two pass (hence the sudden increase in the process medium velocity in Figure 5.6), square bundle with process velocity just below 1.8 m/s (1.74 m/s). The extra pass allows for more heat transfer to take place at a high internal velocity, resulting in a lower outlet process medium temperature. An added advantage of a bundle with an even number of passes is that the process fluid leaves the bundle at the same side it enters.

Table 5.4 presents the total heat transfer rate for the HDWCS, together with the heat transfer rate in the bare tube bundle and change in process temperature across the HDWCS. All values are for a system that is 10 m in length.

Table 5.4: Heat transfer performance for HDWCS

Description	Unit	Initial Case	Selected case
Bare bundle height	mm	540	810
No. of tube rows	-	16	24
Bare bundle width	mm	500	800
No. of tubes per row	-	13	21
No. of passes	-	1	2
Performance (wet operation)			
HDWCS HT rate	kW	643.1	914.3
Conventional HT rate	kW	467.3	479.6
$\Delta T_{p\ (HDWCS)}$	ºC	1.807	2.571
HT rate in bare tube bundle	kW	194.6	462.2
Bare bundle HT / Total HT	%	30%	51%
Pressure drop	Pa	104	107
Flow power (VΔp)	kW	10.6	13.2
Process medium velocity	m/s	2.1	1.74

5.5 Performance curves

Figure 5.7 present the expected performance in terms of process medium outlet temperatures under different operating conditions.

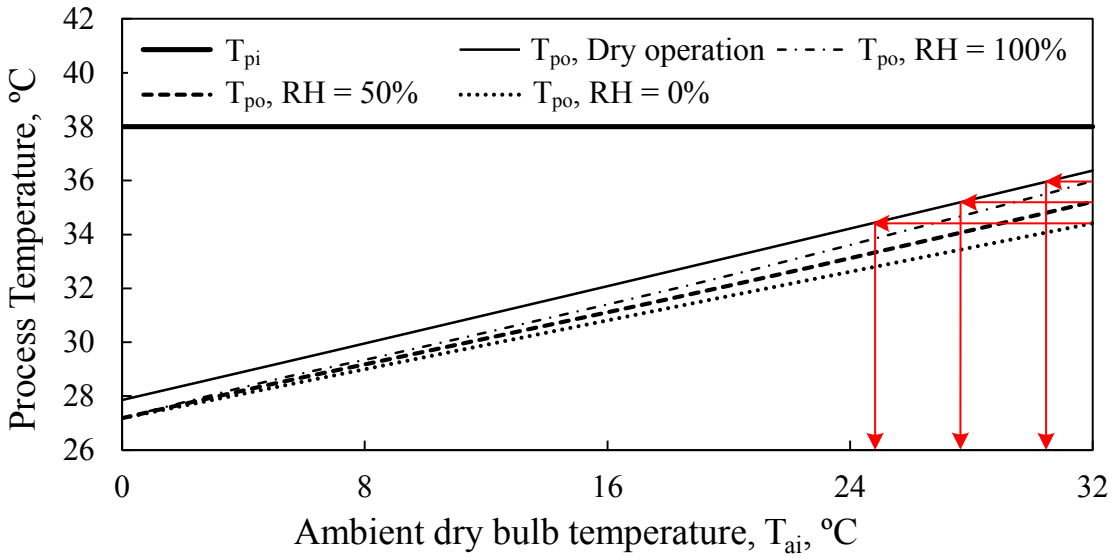

Figure 5.7: Process medium outlet temperature as a function of the ambient air temperature

The performance curves are based on an inlet process medium temperature of 38 ºC with the ambient dry bulb temperature ranging from 0 ºC to 32 ºC. The performance curves are repeated for air relative humidities (*RH*) of 0 % (dry air), 50 % and 100 % (fully saturated air).

From Figure 5.7, wet operation leads to increasing the range of operation. When operating in dry air (*RH* = 0 %), the wet performance at T_{ai} = 32 ºC delivers that of dry performance at T_{ai} = 24.8 ºC a gain of 7.2 ºC in range. For ambient conditions of *RH* = 50 %, wet performance at T_{ai} = 32 °C is equivalent to that of dry performance at T_{ai} = 27.7 ºC (gain of 4.32 ºC). Under saturated air conditions, wet performance at T_{ai} = 32 ºC is equivalent to that of dry performance at T_{ai} = 30.7 ºC, a mere gain of 1.3 C. Wet performance can thus increase the operation range by between 7.2 ºC and 1.3 ºC at T_{ai} = 32 ºC, depending on the relative humidity of the ambient air. Figure 5.8 presents the change in process medium temperature for the same performance curves presented in Figure 5.7.

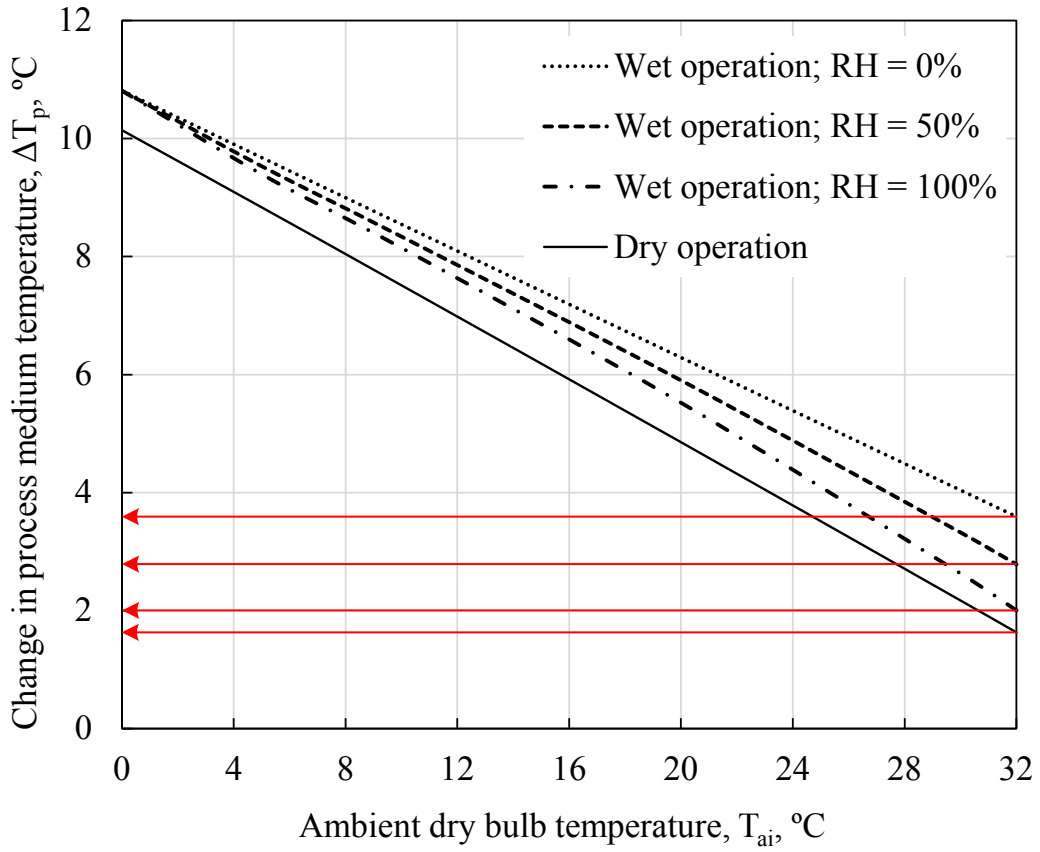

Figure 5.8: Change in process medium temperature

From Figure 5.8, dry performance delivers a change in process medium temperature, ΔT_p = 1.62 ºC at T_{ai} = 32 ºC. Under wet operation, a ΔT_p = 2 ºC for *RH* = 100 %, ΔT_p = 2.8 ºC for *RH* = 50 % and a ΔT_p = 3.6 ºC for dry ambient air at T_{ai} = 32 ºC is predicted. This proves that under wet operation a gain in heat transfer

performance of between 23.4 % (RH = 100 %) and 122 % (Dry air) is predicted with the bare tube bundle dimensions determined from the parametric study.

Wet operation under saturated air conditions, delivers a better performance than dry operation due to the wet operation heat transfer coefficient being higher than that under dry operation. Sensible heat transfer still takes place between the water and the air under saturated air conditions.

For low ambient dry bulb temperatures (T_{ai} < 5 ºC) the relative humidity of the air has an insignificant effect on the change in process medium temperature. This could be due to the small change in wet bulb temperature for the change in relative air humidity at low ambient dry bulb temperatures.

For high ambient dry bulb temperatures (T_{ai} > 24 ºC) the relative humidity has a significant effect on the change in process medium temperature which is due to the increasing difference in the wet bulb temperature as the ambient dry bulb temperature becomes higher. In general, the change in process medium temperature, under wet operation, can be calculated as a function of the ambient dry bulb temperature and relative air humidity, given by equation (5.5.1) as,

$$\Delta T_{p(wet)} = f(RH)T_{ai} + 10.821 \tag{5.5.1}$$

where T_{ai} is in degrees Celsius. The parameter, f(RH) can be calculated from equation (5.5.2) as,

$$f(RH) = 0.04761RH - 0.2258 \tag{5.5.2}$$

with RH, the relative humidity of air in percentage.

Dry operation produces a linear relationship between the change in temperature and ambient dry bulb temperature, indicating that the relative humidity had a negligible effect on the performance of the HDWCS under dry operation. No water is added to the air stream which leads to no change in the water content of the air across the HDWCS and as such the dry operation is unaffected by the relative air humidity. The change in process medium temperature, under dry operation is a linear function of the ambient dry bulb temperature given by equation (5.5.3) as,

$$\Delta T_{p(dry)} = -0.2662T_{ai} + 10.1612 \tag{5.5.3}$$

Figure 5.9 presents the number of conventional air-cooled systems required to attain the same performance as the HDWCS under wet operation. This figure presents the gains in wet performance compared to a conventional air-cooled system as a function of the ambient air temperature for different relative air humidities.

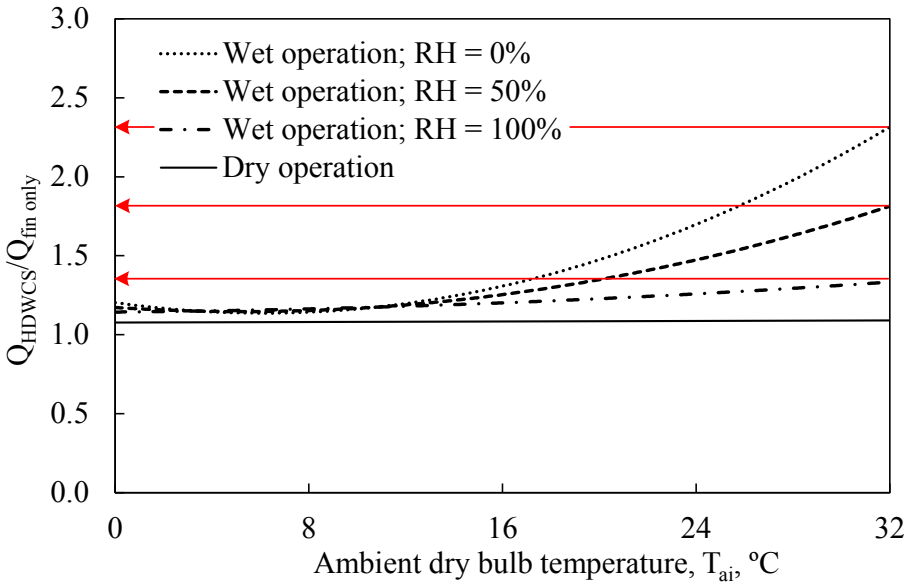

Figure 5.9: Increase in performance compared to a conventional air-cooled cooling system

From Figure 5.9 the impact of the bare tube bundle as a performance booster is noted. Dry air conditions (RH = 0 %) produces a favourable operating condition for the HDWCS under wet operation, with the HDWCS delivering a 140 % gain in performance at T_{ai} = 32 ºC, making the HDWCS more than double as effective for high ambient dry bulb temperatures. For RH = 50 % the bare tube bundle can boost performance by 80 % and at RH = 100 %, the HDWCS delivers a 35% gain.

The HDWCS under dry operation delivers a small increase in performance mainly due to the additional heat transfer area of the bare tube bundle. All numbers above are compared to a conventional air-cooled system with only finned tube bundles (of the same dimensions as those in the HDWCS and at the same flow power).

5.6 Discussion and recommendations

The parametric study shows that adding additional tubes per row has a more significant impact on the performance of the bare tube bundle compared to the addition of tube rows.

More tubes per row translates into a larger frontal area for the bare tube bundle which in turn allows for a larger air flow volume through the bare tube bundle with no increase in air-side pressure drop. The bare tube bundles with dimensions

determined by the parameter study allows for an additional tube pass at the optimal process medium velocity.

The performance curves presents the gain in performance due to the HDWCS operating wet. Although it is not possible to deliver a process medium outlet temperature lower than the ambient dry bulb temperature, the HDWCS delivers a significant boost in performance.

The HDWCS performs exceptionally well in dry air conditions when under wet operation. The large gain in performance with dry air conditions shows that the HDWCS can be an effective cooling system in arid regions with a limited supply of water. With air at a RH = 50 %, the HDWCS was still able to boost performance by 80 % compared to a conventional air-cooled system.

Increasing the tubes per row will have no effect on the air-side pressure drop over the bare tube bundle while increasing the air flow volume through it. With more tubes per row, less tube rows will be required and thus the pressure drop over the bare tube bundle decreases.

6. CONCLUSION

6.1 Introduction

This chapter evaluates the success of this study by evaluating the objectives as set out in Chapter 1. A summary of the purpose of this document is presented together with the findings from each chapter and how successfully each objective is achieved.

Further, discussions are presented based on the findings from the numerical modelling and experimental observations before recommendations towards future work are presented.

6.2 Motivation

This study is a continuation of research done at Stellenbosch University on the topic of hybrid (dry/wet) cooling to find more environmentally friendly solutions for cooling with reduced life-cycle costs.

The HDWCS, described in Chapter 5, satisfies this need by using less water compared to wet only cooling systems and is less susceptible to performance penalties during high ambient temperatures as currently experienced by dry only cooling systems.

This study was carried out by initially gaining background knowledge from a literature review, modelling the finned and bare tube bundle sections numerically, investigating bare tube bundle uncertainties experimentally and performing a parametric study to determine the optimal bare tube bundle dimensions to operate as an efficient performance booster when dry cooling would not suffice.

6.3 Section evaluation

This evaluation presents how this study achieved the objectives as set out in Chapter 1 by presenting a summary of each chapter.

Chapter 1 introduced the HDWCS, by presenting background on the subject of evaporative and dry cooling systems in combined or hybrid form. This placed the HDWCS in context to previous research done on hybrid cooling. Further, the scope, motivation and objectives of this study were established.

In order to gain adequate knowledge on the subject of hybrid cooling, a literature review was completed and presented in Chapter 2. This entailed literature on current novel cooling systems with specific focus on evaporative and hybrid cooling systems. Performance models and characteristics on finned and bare tube bundles, under dry and wet operation were presented, together with literature supporting the selected mass transfer, heat transfer and air-side pressure loss coefficient correlations. Further, findings from various authors were presented to motivate

experimental investigations for this study (Mizushina *et al.* (1967), Dreyer (1988), Ribatski and Jacobi (2005) and Anderson (2014)). It was evident that more research into multi stage hybrid water coolers is required.

To predict the performance of the HDWCS, a numerical model was developed and the relevant theory presented in Chapter 3. In addition to this, an integral and row discretised model for the bare tube bundle were developed to investigate the effect of analysing the bare tube bundle on different levels.

The integral model was based on inlet and outlet properties of the bundle as a whole while the row discretised model analysed the bare tube bundle on a row by row level. It was found that mass and heat transfer coefficients correlated from experimental data by employing the integral model cannot be used in a row discretised model to predict the heat transfer performance. The integral model is simpler, less time consuming and gave reasonably accurate results. Thus the integral model served as an adequate model for predicting the heat transfer performance of the bare tube bundle under wet operation.

Anderson (2014) observed a significant increase in air-side pressure drop under critical air flow rates from his experimental work and as such, the air-side of the bare tube bundle under wet operation was investigated experimentally in Chapter 4. An experimental apparatus, representative of the bare tube bundle designed by Anderson (2014), was constructed and tested under isothermal conditions.

The first experiment investigated the effect of critical air flow on air-side pressure drop at different deluge water flow rates. It was found that in order to avoid critical air flow through the bundle under wet operation, an air mass velocity of $G_{av} = 3$ kg/sm^2 should not be exceeded. In order to avoid dry-out areas through the bundle, a minimum deluge water mass velocity of $\Gamma_{dw} / d_o = 1.89$ kg/sm^2 should be adhered to.

The second experiment investigated two attachment methods for the thermocouples, placed throughout the bundle, to measure the deluge water temperature. It was found that by using 4 zip ties to attach the thermocouple resulted in a higher measuring certainty concerning the accuracy of the deluge water temperature (due to the catchment created with the zip tie head). If a bare tube bundle, inclined at an angle is tested, the thermocouples throughout the bundle should be placed as far down the tubes as possible to avoid measuring tip dry-out.

The third experiment investigated the effect of different numbers of tube rows present in the bundle on the air-side pressure drop across the bundle under wet and dry operation. The measured data was used to correlate the air-side pressure drop (1) as a function of the air mass velocity, deluge water mass velocity and number of tubes rows for wet operation and (2) as a function of the air mass velocity and number of tube rows for dry operation. It was found that the pressure drop under wet operation was higher compared to dry operation. Reuter and Anderson (2016) over predicted the air-side pressure drop for wet operation and under predicted it

for dry operation. The bare tube bundle on which the correlations of Reuter and Anderson (2016) is based, has 25 tube rows and stretches 1.5 m in width. Scaling effects could be possible reasons for the differences in predicted and measured air-side pressure drops.

Chapter 5 presented the HDWCS together with a parametric study and performance characteristics. From the parametric study it was found that the bare tube bundle should be as wide as possible rather than consist of many tube rows. By doing so, increased performance is expected as a maximum air flow rate can be achieved together with minimum air-side pressure drop across the bundle.

A bare tube bundle of 21 tubes per row resulted in a width of 817 mm and 24 tube rows resulted in a height of 801 mm delivering a square, two-pass bare tube bundle in which the process medium travelled at an optimal velocity of 1.74 m/s inside the tubes.

The performance curves presented the expected gains in heat transfer performance that could be achieved by the HDWCS under wet operation. The selected bare tube bundle could deliver a maximum gain of 140 % in dry ambient air conditions during hot days compared to a conventional air-cooled system, consisting only of finned tube bundles similar to that in the HDWCS. During saturated ambient air conditions, the HDWCS still delivered a 35 % gain compared to the conventional air-cooled system. It is thus evident that the HDWCS could serve as a competitive alternative to conventional air-cooled systems.

6.4 Recommendations

Based on the findings of this study the following recommendations pertaining to future work are made:

1. Performance of a two stage system with dedicated fans for each stage should be considered. Keeping the air flow through each stage separate, their air flow rates can be better controlled and would provide the HDWCS with more performance flexibility.
2. A computational flow dynamics (CFD) analyses should be carried out. A CFD analysis should provide invaluable insight into the air flow patterns through both stages under different air conditions (flow rate and saturation levels).
3. More investigation is required into the evaporation rate of deluge water. As this study focused on visual investigation of the air-side of the bare tube bundle, no process water was passed through the bare tubes as headers would have obstructed visual inspection of the deluge water film flow. By accurately determining the evaporation rate of water as a function of the system inputs, smaller water flow rates and better tube wetting methods can be investigated.
4. A full scale thermal test should be carried out on the bare tube bundle of Anderson (2014) with the temperature measuring methods investigated in this study applied to determine if these attachment methods increases the measuring certainty of deluge water temperature through the bare tube bundle. Apart from

confirming measurement certainty, the pressure loss correlation obtained from experimental work in this study can be extrapolated to the full scale bare tube bundle of Anderson (2014).

5. A two stage prototype could be constructed once a better understanding of the air flow patterns and evaporation rates are acquired. Experimental confirmation of modelled results should serve as ample motivation to introduce the HDWCS to industry.

7. REFERENCES

Ackers, M. S. (2012). *Performance and thermo-mechanical cost evaluation of API 661 air-cooled heat exchangers.* Stellenbosch: Stellenbosch University.

Anderson, N. R. (2014). *Evaluation of the performance characteristics of a hybrid (dry/wet) induced draft dephlegmator.* Stellenbosch: Stellenbosch University.

Cale, S. A. (1982). *Development of evaporative cooling packing Report EUR 7709 EN.* Luxemburg: Commission of European communities.

Dreyer, A. A. (1988). *Analysis of evaporative coolers and condensers.* Stellenbosch: Stellenbosch University.

Finlay, I. C., & Harris, D. (1984). Evaporative cooling of tube banks. *International journal of refrigeration, 7*(4), 214-224.

Gaddis, E. S., & Gnielinski, V. (1985). Pressure drop in cross flow across tube bundles. *International chemical engineering*, 1-15.

Ganguli, A., Tung, S. S., & Taborek, J. (1985). Parametric study of air-cooled heat exchanger finned tube geometry. *AIChE symposium series, 82*(245), 122-128.

Harby, K., Gebaly, D. R., Koura, N. S., & Hassan, M. S. (2016). Performance improvement of vapour compression cooling systems using evaporative condenser: An overview. *Renewable and Sustainable Energy Reviews, 58*, 347-360.

Hasan, A., & Sirén, K. (2002). Theoretical and computational analysis of closed wet cooling towers and its applications in cooling of buildings. *Energy and buildings*, 477-486.

Heyns, J. A. (2008). *Performance characteristics of an air-cooled steam condenser incorporating a hybrid (dry/wet) dephlegmator.* Stellenbosch: Stellenbosch University.

Khan, W. A., Yovanovich, J. R., & Culham, M. M. (2006). Convection heat transfer from tube banks in cross flow: An analytical approach. *International journal of heat and mass transfer*, 4831-4838.

Kröger, D. G. (2004). *Air-cooled heat exchangers and cooling towers.* Stellenbosch: Stellenbosch University.

Maulbetsch, J., & DiFilippo, M. (2012). *Advanced hybrid cooling systems: Technology review*. Palo Alto, California: ERPI.

Merkel, F. (1925, January). Verdunstungskühlung. *VDI-Zeitschrift, 70*(70), 123-128.

Mizushina, T., Ito, R., & Miyashita, H. (1967, October). Experimental study of an evaporative cooler. *International chemical engineering, 7*(4), 727-732.

Nitsu, Y., Naito, K., & Anzai, T. (1969). Studies on characteristics and design procedure of evaporative coolers. *Journal of SHASE Japan, 43*(7).

Oosthuizen, P. C. (1995). *Performance characteristics of hybrid cooling towers.* Stellenbosch: Stellenbosch University.

Owen, M. (2013). *Air-cooled condenser steam flow distributionand related dephlegmator design considerations.* Stellenbosch: Stellenbosch University.

Papaefthimiou, V. D., Rogdakis, E. D., Koronaki, I. P., & Zannis, T. C. (2012). Thermodynamic study of the effects of ambient air conditions on the thermal characteristics of a closed wet cooling tower. *Applied thermal engineering*, 199-207.

Parker, R. O., & Treybal, R. E. (1961). The heat and mass transfer characteristics of evaporative coolers. *Chemical engineering progress symposium series, 27*(32), 138-149.

Pethukov, B. S. (1970). Heat transfer and friction in turbulent pipe flow with variable physical properties. (J. P. Hartnett, & T. F. Irvine, Eds.) *Advances in heat transfer, 6*, pp. 503-564.

Popli, S., Hwang, Y., & Radermacher, R. (2014). Deluge evaporative cooling performance of wavy fin and tube-inclined heat exchangers. *ASHRAE Transcactions, 120*(2), 240-253.

Poppe, M., & Rögener, H. (1984). Evaporative cooling systems. *VDI-Wärmeatlas*, Section Mh.

Reuter, H. C., & Anderson, N. R. (2016). Performance evaluation of a bare tube air-cooled heat exchanger bundle in dry and wet mode. *17th IAHR International conference on cooling tower and heat exchanger* . Gold Coast, Queensland: Stellenbosch University.

Ribatski, G., & Jacobi, A. M. (2005). Falilng-film evaporation on horizontal tubes - a critical reveiw. *International journal of refrigeration, 28*, 635-653.

Schmidt, T. E. (1946). La production calorifique des surfaces munies dialettes. *Annexe du bulletin de L'Institut International du froid*, Annex G-5.

Thermofin. (2013). *Thermofin*. Retrieved June 21, 2015, from www.thermofin.de

Vakiloroaya, V., Samali, B., Fakhar, A., & Pishghadam, K. (2014). A review of different strategiesfor HVAC energy saving. *Energy Conversion and Management, 77*, 738-754.

Zheng, W. Y., Zhu, D. S., Zhou, G. Y., Wu, J. F., & Shi, Y. Y. (2012). Thermal performance analysis of closed wet cooling towers under bot unsaterated and supersaturated conditions. *International journal of heat and mass transfer*, 77803-7811.

Zukauskas, A. (1987). Heat transfer from tubes in cross flow. In S. Kakac, R. Shah, & W. Aung, *Handbook of single phase convective heat transfer* (pp. 6.1-6.45).

A. FLUID PROPERTIES

Fluid properties presented in Appendix A are adapted from Kroger (2004) and used in Appendix B. In all these equations, temperature in Kelvin (K = ºC +273.15).

A.1 The thermophysical properties of dry air from 220 K to 380 K at standard atmospheric pressure.

Density:

$$\rho_a = p_a/(287.08T),\ \text{kg/m}^3 \tag{A.1.1}$$

Specific heat:

$$c_{pa} = 1.045356\times10^{3} - 3.161783\times10^{-1}T + 7.083814\times10^{-4}T^{2} - 2.705209\times10^{-7}T^{3},\ \text{J/kgK} \tag{A.1.2}$$

Dynamic viscosity:

$$\mu_a = 2.287973\times10^{-6} + 6.259793\times10^{-8}T - 3.131956\times10^{-11}T^{2} + 8.15038\times10^{-15}T^{3},\ \text{kg/sm} \tag{A.1.3}$$

Thermal conductivity;

$$k_a = -4.937787\times10^{-4} + 1.018087\times10^{-4}T - 4.627937\times10^{-8}T^{2} + 1.250603\times10^{-11}T^{3},\ \text{W/mK} \tag{A.1.4}$$

A.2 The thermophysical properties of saturated water vapour from 273.15 K to 380 K.

Vapour pressure;

$$p_a = 10^z, \text{Pa} \tag{A.2.1}$$

$$z = 10.79586(1 - 273.16/T) + 5.02808\, log_{10}(273.16/T) + 1.50474 \times 10^{-4}\left\{1 - 10^{-8.29692[(T/273.16)-1]}\right\} + 4.2873 \times 10^{-4}\left[10^{4.76955(1-27316/T)} - 1\right] + 2.786118312$$

Specific heat:

$$c_{pv} = 1.3605 \times 10^3 + 2.31334T - 2.46784 \times 10^{-10}T^5 5.91332 \times 10^{-13}T^6, \text{J/kgK} \tag{A.2.2}$$

Dynamic viscosity:

$$\mu_v = 2.562435 \times 10^{-6} + 1.816683 \times 10^{-8}T + 2.579066 \times 10^{-11}T^2 - 1.067299 \times 10^{-14}T^3, \text{kg/sm} \tag{A.2.3}$$

Thermal conductivity:

$$k_v = 1.3046 \times 10^{-2} - 3.756191 \times 10^{-5}T + 2.217964 \times 10^{-7}T^2 - 1.111562 \times 10^{-10}T^3, \text{W/mK} \tag{A.2.4}$$

Vapour density:

$$\rho_v = -4.062329056 + 0.10277044\text{T} - 9.76300388 \times 10^{-4}\text{T}^2 + 4.475240785 \times 10^{-6}T^3 - 1.004596894 \times 10^{-8}T^4 8.9154895 \times 10^{-12}T^5, \text{kg/m}^3 \tag{A.2.5}$$

A.3 The thermophysical properties of mixtures of air and water vapour

Density:

$$\rho_{av} = \frac{(1+w)\left[1-\frac{w}{(w+0.62198)}\right]p_{abs}}{(287.08T)}, \text{kg air} - \text{vapour/m}^3 \quad \text{(A.3.1)}$$

Specific heat:

$$c_{pav} = \left(c_{pa} + wc_{pv}\right)/(1+w), \text{J/K kg air vapour} \quad \text{(A.3.2a)}$$

Or the specific heat of the air-vapour mixture per unit mass of dry air

$$c_{pma} = c_{pa} + wc_{pv}, \text{J/K kg dry air} \quad \text{(A.3.2b)}$$

Dynamic viscosity:

$$\mu_{av} = \frac{X_a\mu_a M_a^{0.33} + X_v\mu_v M_v^{0.33}}{X_a M_a^{0.5} + X_v M_v^{0.5}}, \text{kg/ms} \quad \text{(A.3.3)}$$

where M_a = 28.97 kg/mole, M_v = 18.016 kg/mole, X_a = 1/ (1+1.608w) and X_v = w/(w+0.622).

Thermal conductivity:

$$\mu_{av} = \frac{X_a k_a M_a^{0.33} + X_v k_v M_v^{0.33}}{X_a M_a^{0.33} + X_v M_v^{0.33}}, \text{W/mK} \quad \text{(A.3.4)}$$

Humidity ratio:

$$w = \left(\frac{2501.6 - 2.3263(T_{wb} - 273.15)}{2501.6 + 1.8577(T - 273.15) - 4.184(T_{wb} - 273.15)}\right) \times \left(\frac{0.62509p_{v(wb)}}{p_{abs} - 1.005p_{v(wb)}}\right) - \left(\frac{1.00416(T - T_{wb})}{2501.6 + 1.8577(T - 273.15) - 4.184(T_{wb} - 273.15)}\right), \text{kg/kg d. a.} \quad \text{(A.3.5)}$$

Enthalpy:

$$i_{av} = \frac{c_{pa}(T - 273.15) + w\left[i_{fgwo} + c_{pv}(T - 273.15)\right]}{1 + w} \text{ , J/kg air vapour} \quad \text{(A.3.6a)}$$

Or the enthalpy of the air-vapour mixture per unit mass of dry air

$$i_{ma} = c_{pa}(T - 273.15) + w\left[i_{fgwo} + c_{pv}(T - 273.15)\right] \text{ , J/kg dry air} \quad \text{(A.3.6b)}$$

A.4 The thermophysical properties of saturated water liquid from 273.15 K to 380 K

Density:

$$\rho_w = \left(1.49343 \times 10^{-3} - 3.7164 \times 10^{-6}T + 7.09782 \times 10^{-9}T^2 - 1.90321 \times 10^{-20}T^6\right)^{-1}, \text{kg/m}^3 \quad \text{(A.4.1)}$$

Specific heat:

$$c_{pw} = 8.15599 \times 10^3 - 2.80627 \times 10T + 5.11283 \times 10^{-2}T^2 - 2.17583 \times 10^{-13}T^6, \text{J/kgK} \quad \text{(A.4.2)}$$

Dynamic viscosity:

$$\mu_w = 2.414 \times 10^{-5} \times 10^{247.8/(T-140)}, \text{kg/sm} \quad \text{(A.4.3)}$$

Thermal conductivity:

$$k_w = -6.14255 \times 10^{-1} + 6.9962 \times 10^{-3}T - 1.01075 \times 10^{-5}T^2 + 4.74737 \times 10^{-11}T^4, \text{W/mK} \quad \text{(A.4.4)}$$

B. SAMPLE CALCULATION FOR HYBRID (DRY/WET) COOLING SYSTEM (HDWCS).

B.1 System parameters

Figure B.1 presents a schematic of the one symmetric half of the HDWCS with bundle dimensions and air flow. Thick arrows show how air passes through the system.

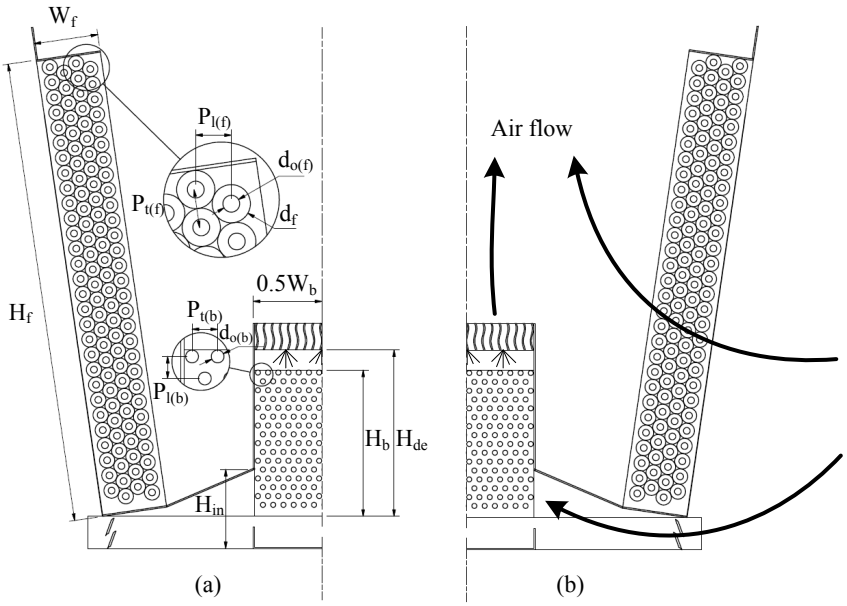

Figure B.1: Schematic of the HDWCS with (a) dimensions and (b) air flow paths

Finned tube bundle specifications are listed in Table B.1

Table B.1: Finned tube bundle specifications

Description	Symbol	Value	Unit
Fin parameters			
Thermal conductivity	k_f	204	W/mK
Fin diameter	d_f	57.2	mm
Fin root diameter	d_r	27.6	mm
Fin tip thickness	t_{ft}	0.25	mm
Fin thickness (mean)	t_f	0.5	mm
Fin root thickness	t_{fr}	0.75	mm
Fin pitch	P_f	2.82	mm
Finned tube bundle parameters			
Bundle width	W_f	0.3	m
Bundle length	L_f	10	m
Bundle height	L_{fi}	2.4	m
Thermal conductivity	$k_{t(f)}$	50	W/mK
Tube outside diameter	$d_{o(f)}$	25.4	mm
Tube inside diameter	$d_{i(f)}$	21.6	mm
Mean thermal contact resistance	R_c	$4x10^{-4}$	m^2K/W
Number of tube rows	$n_{r(f)}$	6	
Number of tubes per row	$n_{tr(f)}$	41	
Number of passes	$n_{p(f)}$	6	
Transverse tube pitch	$P_{t(f)}$	58	mm
Longitudinal tube pitch	$P_{l(f)}$	50	mm
Effective tube length (per pass)	L_t	10	m
Effective total tube length	L_{te}	60	m

Bare tube bundle specifications are listed in Table B.2.

Table B.2: Bare tube bundle specifications

Description	Symbol	Value	Unit
Bundle width	W_b	0.8	m
Bundle Length	L_b	10	m
Bare bundle height	H_b	0.81	m
Number of tube rows	n_r	24	
Number of tubes per row	n_{tr}	21	
Number of tube passes	n_{tp}	2	
Tube thermal conductivity	k_t	45	W/mK
Transverse tube pitch	$P_{t(b)}$	38.0	mm
Lateral tube pitch	$P_{l(b)}$	32	mm
Outer tube diameter	$d_{o(b)}$	19.1	mm
Tube wall thickness	$t_{t(b)}$	1.6	mm

System dimensions relevant to the HDWCS are presented in Table B.3.

Table B.3: System dimensions for the HDWCS

Description	Symbol	Value	Unit
Bare tube bundle inlet height	H_{in}	300	mm
Spray zone height ($H_{sp} = H_{de} - H_b$)	H_{sp}	150	mm
Rain zone drop diameter	d_d	4	mm

The independent air side loss coefficients are presented in Table B.4.

Table B.4: Independent air side loss coefficients

Description	Symbol	Value
Bare bundle inlet losses (Supports and Louvers)	$K_{ct(b)}$	1.5
Water distribution system	K_{wd}	0.5
Plenum recovery	K_{rec}	-0.3

The air mixture properties are presented in Table B.5.

Table B.5: Air mixture properties

Description	Symbol	Value	Unit
Air molecular mass	M_a	28.97	kg/kmol
Vapour molecular mass	M_v	18.02	kg/kmol
Dry-bulb temperature	T_{ai}	305.15	K
Wet-bulb temperature	T_{wbi}	297.15	K
Ambient Pressure	P_{atm}	101325	Pa

Initial parameters required to establish a work point for the system are listed in Table B.6.

Table B.6: Initial parameters for the HDWCS

Description	Symbol	Value	Unit
Process inlet temperature to finned bundle	T_{pi}	311.15	K
Process water mass flow rate	m_p	42.6	kg/s
Deluge water mass flow rate	m_{dw}	12	kg/s
Air mass flux into the finned tube bundle	G_{avi}	2.5	kg/sm^2

B.2 Dry operation

B.2.1 Finned tube bundle energy equation

Converged parameters:

Description	Symbol	Value	Unit
Process medium outlet temperature: Finned bundle	T_{po}	309.75	K
Air outlet temperature: Finned bundle	T_{ao}	309.12	K
Pressure drop over system: Dry operation	$\Delta p_{(dry)}$	119.35	Pa
Flow power ($P = V\Delta p_{(dry)}$)	P_{flow}	80326	W

The following properties of the air at the inlet of the finned tube bundle are calculated from fluid property formulas presented in Appendix A. The specific heats of air and water vapour are calculated at (T_{ai} - 273.15)/2 = 289.15 K as,

Specific heat of air	$c_{p(ai)}$	1006.62	J/kgK	(A.1.2)
Specific heat of vapour	$c_{p(vi)}$	1876.19	J/kgK	(A.2.2)

The remaining fluid properties are calculated at T_{ai} = 305.15 K and given as:

Saturated pressure	p_{vi}	2982.78	Pa	(A.2.1)
Humidity ratio	w_i	0.01558	kg/kg d.a.	(A.3.5)
Air mixture enthalpy	i_{mai}	72129.86	J/kg	(A.3.6b)
Air density	ρ_{avi}	1.1460	kg/m^3	(A.3.1)
Air viscosity	μ_{ai}	1.8705E-05	kg/ms	(A.1.3)
Vapour viscosity	μ_{vi}	9.9579E-06	kg/ms	(A.2.3)

The specific heats of air and water vapour are calculated at (T_{ao} - 273.15)/2 = 291.14 K as,

Specific heat of air	$c_{p(ao)}$	1006.67	J/kgK	(A.1.2)
Specific heat of vapour	$c_{p(vo)}$	1877.91	J/kgK	(A.2.2)

The remaining properties of the air at the outlet of the finned bundle are calculated at $T_{ao} = 309.12$ K as:

air mixture enthalpy	i_{mao}	76249.29	J/kg	(A.3.6b)
Air density	ρ_{avo}	1.1312	kg/m^3	(A.3.1)
Dynamic viscosity outlet air	μ_{avo}	1.8721E-05	kg/ms	(A.3.3)

The process water properties are evaluated at the mean water temperature in the fin bundles $T_{pm} = \frac{T_{pi}+T_{po}}{2} = 310.45$ K

Density	ρ_{pm}	993.33	kg/m^3	(A.4.1)
Specific heat	c_{pp}	4176.84	kJ/kgK	(A.4.2)
Dynamic viscosity	μ_{pm}	6.8636E-04	kg/ms	(A.4.3)
Thermal conductivity	k_p	0.6277	W/mK	(A.4.4)

The total frontal area of the finned tube bundle is calculated from,

$$A_{fr} = W_f L_f = (2.4)(10) = 24 \text{ m}^2 \quad \text{(B.2.1)}$$

And the inlet air mass flow rate is calculated as,

$$m_{avi} = G_{avi} A_{fr} = (2.5)(24) = 60 \text{ kg/s} \quad \text{(B.2.2)}$$

The dry air mass flow rate is calculated with the inlet humidity ratio as,

$$m_a = \frac{m_{avi}}{1+w_i} = \frac{60}{1+0.0156} = 59.0794 \text{ kg/s} \quad \text{(B.2.3)}$$

In order to calculate the internal heat transfer coefficient, the flow regime and inside cross sectional area of a single finned tube is required. The cross sectional area is calculated as,

$$A_{ts} = 0.25\pi d_i^2 = 0.25\pi(0.0216)^2 = 3.6644 \times 10^{-4} \text{ m}^2$$

The velocity of the process water inside the finned tube ideally needs to remain below 3 m/s to prevent vibrations. The water velocity in this case is,

$$v_p = \frac{m_p}{\rho_{pm} A_{ts} n_{tr}} = \frac{42.6}{(993.33)(3.6644\times10^{-4})(41)} = 2.8545 \text{ m/s} \quad \text{(B.2.5)}$$

which is below the maximum value. The process medium Reynolds number through the finned tube is,

$$Re_p = \frac{\rho_{pm} v_p d_i}{\mu_{pm}} = \frac{(993.33)(2.8545)(0.0216)}{6.8636\times10^{-4}} = 89233 \quad \text{(B.2.6)}$$

Which indicate that the flow is fully turbulent, since $Re_p >> 4\,000$. The internal friction factor is subsequently calculated from,

$$f_D = (1.82log_{10}(Re) - 1.64)^{-2} = (1.82log_{10}(89233) - 1.64)^{-2} \quad \text{(2.3.6)}$$

$$= \quad 0.01842$$

Pethukhov (1970) developed an equation for the process water Nusselt number that was subsequently modified by Kröger (2004) and presented as equation (2.3.5). The proses medium heat transfer coefficient in the finned tube bundle is calculated as,

$$h_{p(f)} = \frac{0.125 f_D Re Pr}{1.07+12.7(0.125 f_D)^{0.5}\left(Pr^{0.667}-1\right)} \frac{k_p}{d_{i(f)}} = \frac{0.125(0.01842)(89233)(0.715)}{1.07+12.7(0.125(0.01842)^{0.5}\left((0.715)^{0.667}-1\right)} \frac{0.628}{0.0216} = 12711.53 \text{ W/m}^2\text{K} \quad (2.3.5)$$

Furthermore, the log mean temperature difference (LMTD) across the finned tube is,

$$\Delta T_{lm} = \frac{\left(T_{po} - T_{ai}\right) - \left(T_{pi} - T_{ao}\right)}{\ln\left[\frac{\left(T_{po} - T_{ai}\right)}{T_{pi} - T_{ao}}\right]} \quad (3.2.9)$$

$$= \frac{(309.75 - 305.15) - (311.15 - 309.12)}{\ln\left[\frac{(309.75 - 305.15)}{311.15 - 309.12}\right]}$$

$$= 3.1515 \text{ K}$$

The temperature correction factor for a multi-pass heat exchanger can be found in Kröger (2004). For a 6 pass cross flow heat exchanger the correction factor is calculated from,

$$F_T = 1 - \sum_{i=1}^{4} \sum_{k=1}^{4} a_{i,k} (1 - \phi_3)^k sin\left[2i \bullet arctan(\phi_1/\phi_2)\right] = 1 \quad (B.2.7)$$

Where the dimensionless temperature changes may be defined as:

$$\phi_1 = \frac{T_{pi} - T_{po}}{T_{pi} - T_{ai}} = 0.2072$$

$$\phi_2 = \frac{T_{ao} - T_{ai}}{T_{pi} - T_{ai}} = 0.6020$$

$$\phi_3 = \frac{\phi_1 - \phi_2}{ln\left[(\phi_1 - \phi_2)/(1 - \phi_1)\right]} = 0.5729$$

The constants in eq. (B.2.7) are given in Table B.7.

Table B.7: Constants for equation (B.2.7)

$a_{i,k}$	i = 1	2	3	4
k = 1	-0.339	0.0277	0.179	-0.0199
2	2.38	-0.0999	-1.21	0.04
3	-5.26	0.0904	2.62	0.0494
4	3.9	-0.000845	-1.81	-0.0981

The critical area for the air flow across the finned bundle is calculated from,

$$A_c = \left(\frac{n_{tr(f)}L_t}{P_f}\right)\left[P_{t(f)}P_f - \left(d_f - d_r\right)t_f - P_f d_r\right]$$

$$= \left(\frac{(41)(10)}{(0.0028)}\right)[(0.058)(0.0028) - (0.0576 - 0.0276)(0.0005) - (0.0028)(0.0276)] = 10.3139 \text{ m}^2$$

The effective air side fin surface is given by

$$A_f = n_{tr(f)}n_{r(f)}\frac{L_t}{P_f}\left[\pi\left\{\frac{2}{4}\left(d_f^2 - d_r^2\right) + d_f t_{ft}\right\}\right]$$

$$= (41)(6)\frac{10}{0.0028}\left[\pi\left\{\frac{2}{4}\left((0.0572)^2 - (0.0276)^2\right) + (0.0572)(0.0025)\right\}\right] = 3475.96 \text{ m}^2$$

The total air side surface area is calculated from

$$A_{a(f)} = A_f + \frac{\pi n_{tr(f)}n_{r(f)}L_t d_r\left(P_f - t_f\right)}{P_f} = 3475.96 + \frac{\pi(41)(6)(10)(0.0276)(0.0028-0.0025)}{0.0028} = 3651.47 \text{ m}^2$$

The inside surface area of the finned tube bundle is

$$A_{p(f)} = (41)(6)\pi(10)(0.0216) = 166.9317 \text{ m}^2 \qquad \text{(B.2.8)}$$

In the absence of fouling, the thermal resistance is comprised of the tube wall, the root and the contact resistance and given by,

$$R_{th(f)} = \frac{1}{n_{tr(f)}n_r L_t}\left[\frac{ln\left(d_o/d_i\right)}{2\pi k_t} + \frac{ln\left(d_r/d_o\right)}{2\pi k_t} + \frac{R_c}{\pi d_o}\right] \qquad \text{(B.2.9)}$$

$$= \frac{1}{(41)(6)(10)}\left[\frac{ln\left(25.4/21.6\right)}{2\pi(50)} + \frac{ln\left(27.6/21.6\right)}{2\pi(50)} + \frac{4\times10^{-5}}{\pi(25.4)}\right]$$

$$= 4.3981 \times 10^{-7} \text{ K/W}$$

The first term in equation (B.2.9) relates to the tube wall resistance, the second term relates to the fin root thermal resistance and the third term relates the contact resistance between the tube outside diameter and fin. Constants for the fin efficiency as set out in Kröger (2004) are,

$$\phi = \left(\frac{d_f}{d_r} - 1\right)\left[1 + 0.35ln\left(\frac{d_f}{d_r}\right)\right] = \left(\frac{57.2}{25.4} - 1\right)\left[1 + 0.35ln\left(\frac{57.2}{25.4}\right)\right] = 1.3460$$

$$b = \left(\frac{2h_a}{k_f t_f}\right)^{0.5} = \left(\frac{2(49.198)}{(204)(0.0005)}\right)^{0.5} = 31.0591$$

$$\eta_f = \frac{tanh(bd_r\,\phi/2)}{(bd_r\,\phi/2)} = \frac{tanh((31.0591)(0.0254)(1.346)/2)}{((31.0591)(0.0254)\,(1.346)/2)} = 0.4353$$

The fin effectiveness is,

$$e_f A_a = A_a - A_f\left(1 - \eta_f\right) = 3651.47 - (3475.96)(1 - 0.4353)$$

$$= 1688.48 \text{ m}^2$$

The critical air mass velocity through the fin bundle is determined as,

$$G_c = \frac{m_{avi}}{A_c} = \frac{60}{10.3139} = 5.8174 \text{ kg/sm}^2 \qquad \text{(B.2.10)}$$

The critical air Reynolds number is calculated from,

$$Re_c = \frac{G_c d_r}{\mu_a} = \frac{(5.8174)(25.4)}{1.863\times10^{-5}} = 8618 \qquad \text{(B.2.11)}$$

The ratio of the total air side area to the root area is determined from,

$$\frac{A}{A_r} = 0.5\left(d_f{}^2 - d_r{}^2\right) + d_f t_{ft} + d_r\left(\frac{P_f - t_{fr}}{d_r P_f}\right)$$

$$= 0.5\left((0.0572)^2 - (0.0254)^2\right) + (0.0572)(0.00025) + (0.0254)\left(\frac{0.0028 - 0.00075}{(0.0254)(0.0028)}\right)$$

$$= 17.0303$$

and the air side heat transfer coefficient is calculated using,

$$h_a = 0.38 Re_c^{0.6} Pr_{avm}^{0.333}\left(\frac{A}{A_r}\right)^{-0.15}\frac{k}{d_r} = \qquad \text{(2.3.7)}$$

$$0.38(8186)^{0.6}(0.715)^{0.333}(17.0303)^{-0.15}\frac{0.0266}{0.0254} = 49.1980 \text{ W/m}^2\text{K}$$

The overall heat transfer coefficient based on the outside area is calculated from equation (3.6.1) as,

$$U_a = \frac{1}{A_a}\left[\frac{l}{h_p A_p} + R_{th} + \frac{1}{h_a A_a e_f}\right] = \frac{1}{3651.47}\left[\frac{l}{(12711.53)(166.9317)} + 4.3981 \times 10^{-7} + \frac{1}{(49.1980)(1688.48)}\right] = 21.1491 \text{ W/m}^2\text{K} \quad (3.6.1)$$

The heat transfer rate given by the general heat exchanger equation as,

$$Q_{UA} = F_T U_a A_a \Delta T_{lm} = (1)(21.1491)(3651.47)(3.1515) \quad (2.3.1)$$

$$= 243373.1 \text{ W}$$

The heat transfer rate from the process water has to be equal to that from the air stream. The heat transferred from the process water is given by equation (3.5.1) as,

$$Q_p = m_p c_{ppm}(T_{pi} - T_{po}) = 42.6(4176.84)(311.15 - 309.75) \quad (3.5.1)$$

$$= 243373.1 \text{ W}$$

Similarly the heat transferred to the air stream is,

$$Q_a = m_a c_{pam}(T_{ao} - T_{ai}) = 59.08(1020.82)(309.124 - 305.15) \quad (3.5.1)$$

$$= 243373.1 \text{ W}$$

With $c_{pam} = 0.5(c_{pai} + c_{pao})$ the mean specific heat of the air stream.

B.2.2 Bare tube bundle energy equation: Dry operation

The outlet air and process water temperatures converged to the values as displayed

Description	Symbol	Value	Unit
Process outlet temperature: Bare bundle	T_{po}	309.52	K
Air outlet temperature: Bare bundle	T_{ao}	307.95	K
Air mass flow rate: Bare tube bundle	$m_{avi(b)}$	16.578	kg/s

The inlet air conditions are similar to that determined for the finned tube bundle in Section B.2.1.

The specific heats of the outlet air and water vapour from the bare tube bundle are calculated at (T_{ao} - 273.15)/2 = 290.55 K as,

Specific heat of air	$c_{p(ao)}$	1006.66	J/kgK	(A.1.2)
Specific heat of vapour	$c_{p(vo)}$	1877.40	J/kgK	(A.2.2)

The remaining outlet air properties are evaluated at T_{ao} = 307.95 K with the outlet humidity ratio equal to the inlet humidity ratio.

Humidity ratio	w_o	0.0156	kg/kg d.a.	(A.3.5)
Saturated air mixture enthalpy	i_{mao}	75037.01	J/kg	(A.3.6b)
Air density	ρ_{avo}	1.1355	kg/m^3	(A.3.1)
Dynamic viscosity outlet air	μ_{avo}	1.8661E-05	kg/ms	(A.3.3)

The process water properties are evaluated at the mean water temperature, $T_{pm} = \frac{T_{pi}+T_{po}}{2}$ = 309.65 K, in the bare tube bundles as,

Density	ρ_{pm}	993.61	kg/m^3	(A.4.1)
Specific heat	c_{pp}	4176.92	kJ/kgK	(A.4.2)
Dynamic viscosity	μ_{pm}	6.9727E-04	kg/ms	(A.4.3)
Thermal conductivity	k_p	0.6266	W/m^{2}K	(A.4.4)

The dry air mass flow rate is calculated as earlier from,

$$m_a = \frac{m_{avi}}{1+w_i} = 16.58 \text{ kg/s} \qquad \text{(B.2.3)}$$

No vapour is added to the air-vapour mixture across the bundle, thus the air mass flow rate remains unchanged across the bundle as,

$$m_{avi} = m_{avo} = m_{avm} = 16.58 \text{ kg/s}$$

The frontal area of the of bare tube bundle is calculated as earlier from,

$$A_{fr} = 0.5 W_b L_b = 0.5(0.81)(10) = 4.01 \text{ m}^2 \qquad \text{(B.2.1)}$$

and the critical area through which the air passes is given by,

$$A_c = n_{tr(b)} L_b \left(P_{t(b)} - d_{o(b)}\right) = (10.5)(10)(0.038 - 0.019) = 1.805 \text{ m}^2 \qquad \text{(B.2.12)}$$

The critical air mass velocity is recalculated from equation (B.2.10) as,

$$G_c = \frac{m_{avi}}{A_c} = \frac{16.58}{1.805} = 9.185 \text{ kg/m}^2\text{s} \qquad \text{(B.2.10)}$$

and the log mean temperature difference (LMTD) is according to,

$$\Delta T_{lm} = \frac{\left(T_{po} - T_{ai}\right) - \left(T_{pi} - T_{ao}\right)}{\ln\left[\frac{\left(T_{po} - T_{ai}\right)}{T_{pi} - T_{ao}}\right]} \qquad \text{(3.2.9)}$$

$$= \frac{(309.516 - 305.15) - (309.782 - 307.955)}{\ln\left[\frac{(309.516 - 305.15)}{309.782 - 307.955}\right]}$$

$$= 2.915 \text{ K}$$

The inside cross sectional area of one bare tube is calculated from,

$$A_{ts} = 0.25\pi d_i^2 = 0.25\pi(0.016)^2 = 1.9607 \times 10^{-4} \text{ m}^2$$

The velocity of the process water in the bare bundle is given as,

$$v_p = \frac{m_p n_p}{\rho_{pm} A_{ts} n_{tr} n_r} = \frac{(42.6)(2)}{(993.61)(1.9607\times10^{-4})(10.5)(24)} = 1.735 \text{ m/s} \quad \text{(B.2.5)}$$

The total tube inside surface area as earlier from equation (B.2.8) as,

$$A_p = \pi d_i n_{tr} n_r L_t = \pi(0.016)(10.5)(24)(10) = 125.09 \text{ m}^2 \quad \text{(B.2.8)}$$

and the outside total tube area for the bare tube bundle is calculated as,

$$A_a = \pi d_o n_{tr} n_r L_t = \pi(0.019)(10.5)(24)(10) = 150.42 \text{ m}^2 \quad \text{(B.2.13)}$$

The process Reynolds number is calculated as earlier from,

$$Re_p = \frac{\rho_{pm} v_p d_i}{\mu_{pm}} = \frac{(993.61)(1.735)(0.016)}{6.973\times10^{-4}} = 39059 \quad \text{(B.2.6)}$$

The flow is turbulent since $Re_p >> 4\,000$. The friction factor inside the tube is given by,

$$f_D = (1.82log_{10}(Re) - 1.64)^{-2} = (1.82log_{10}(39059) - 1.64)^{-2} = 0.0222 \quad \text{(2.3.6)}$$

The internal heat transfer coefficient in the bare tube bundle is calculated from,

$$h_{p(b)} = \frac{0.125 f_D Re Pr}{1.07 + 12.7(0.125 f_D)^{0.5}\left(Pr^{0.667} - 1\right)} \frac{k_p}{d_{i(b)}} \quad \text{(2.3.5)}$$

$$= \frac{0.125(0.0222)(39059)(4.648)}{1.07+12.7(0.125(0.0222))^{0.5}\left((4.648)^{0.667}-1\right)} \frac{0.6266}{0.016} = 8697.61 \text{ W/m}^2\text{K}$$

The air-side Reynolds number based on the tube outside diameter is given by equation (B.2.12) as,

$$Re_c = \frac{G_c d_o}{\mu_{am}} = \frac{(9.185)(0.016)}{1.589\times10^{-5}} = 9383 \quad \text{(B.2.12)}$$

The air-side heat transfer coefficient is calculated from,

$$h_a = \frac{0.61\left(\frac{P_t}{d_o}\right)^{0.091}\left(\frac{P_l}{d_o}\right)^{0.053}}{1-2exp\left(-1.09\frac{P_l}{d_o}\right)} Re_C^{0.5} Pr_{avm}^{1/3} \frac{k_{avm}}{d_o} \tag{2.3.9}$$

$$= \frac{0.61\left(\frac{0.038}{0.019}\right)^{0.091}\left(\frac{0.032}{0.019}\right)^{0.053}}{1-2exp\left(-(1.09)\frac{0.032}{0.019}\right)} (9383)^{0.5}(4.648)^{1/3}\frac{0.025}{0.019} = 110.36 \text{ W/m}^2\text{K}$$

The overall heat transfer coefficient based on the outside tube area is given by equation (3.5.3) as,

$$U_a = \left[\frac{d_o}{h_p d_i} + \frac{d_o ln\frac{d_o}{d_i}}{2k_t} + \frac{1}{h_a}\right]^{-1} \tag{3.5.3}$$

$$= \left[\frac{0.019}{(8697.6)(0.016)} + \frac{(0.019)ln\left(\frac{19}{16}\right)}{2(45)} + \frac{1}{110.36}\right]^{-1} = 108.25 \text{ W/m}^2\text{K}$$

From the general heat exchanger equation, equation (3.5.2), the heat transfer from the process water to the air stream is given as,

$$Q = F_T U_a A_a \Delta T_{lm} = (1)(108.250(150.42)(2.915) = 47457.6W \tag{3.5.2}$$

The heat transfer rate from the process water is calculated from,

$$Q_p = m_p c_{ppm}\left(T_{pi} - T_{po}\right) = (42.6)(4176.92)(309.72 - 309.52)$$
$$= 47457.6 \text{ W} \tag{3.5.1}$$

The heat transfer rate to the air stream is calculated by,

$$Q_a = m_a(i_{mao} - i_{mai}) = (16.32)(75037.01 - 72129.86)$$
$$= 47457.6\text{W} \tag{3.5.1}$$

Equation (3.5.2) and both definitions of equation (3.5.1) are in agreement and thus the calculation converges to the correct values. The outlet air temperature is given as,

$$T_{ao} = T_{ai} + \frac{Q}{m_a c_{pam}} = 305.15 + \frac{47457.6}{(16.32)(1006.6)} = 307.95 \text{ K} \tag{3.5.5}$$

and the process water outlet temperature is given by,

$$T_{po} = T_{pi} - \frac{Q}{m_p c_{ppm}} = 309.782 - \frac{47457.6}{(42.6)(4176.92)} = 309.52 \text{ K} \tag{3.5.6}$$

B.2.3 Draft equation

Figure B.2 presents the pressure loss diagram for the HDWCS.

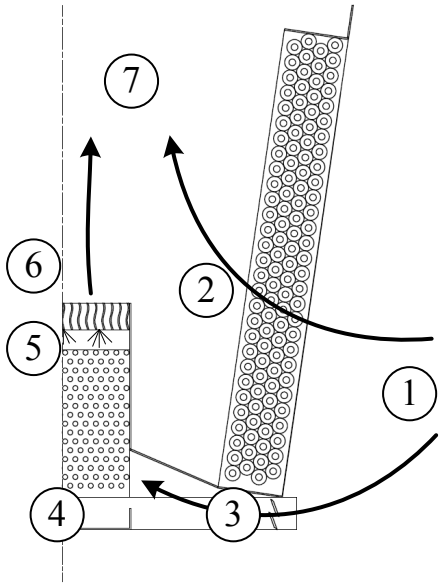

Figure B.2: Pressure loss diagram for draft equation.

The converged mass flow rate through the bare tube bundle together with the pressure drop over each stage under dry operation are calculated as

Description	Symbol	Value	Unit
Air mass flow rate: Bare tube bundle	$m_{avi(b)}$	16.58	kg/s
System Pressure loss: First stage	Δp_{fin}	119.36	Pa
System Pressure loss: Second stage	Δp_{bare}	119.36	Pa

The pressure at point 2 in Figure B.2 can be calculated as follow. The total pressure drop over the finned tube bundle is given by equation (2.3.6) as,

$$\Delta p_{t(fin)} = 2n_r \left\{ 1 + 2exp\left[\frac{(d_f - P_t)/(4d_r)}{(P_t - d_f)/d_r} \right] \right\} \left\{ 0.021 + 13.6 \frac{d_f - P_t}{Re_c(P_f - t_f)} + 0.24256 \left[\frac{d_f - P_t}{Re_c(P_f - t_f)} \right]^{0.2} \right\} \frac{{G_c}^2}{\rho_{av}} + \rho_{avo} {v_{avo}}^2 = \quad (2.3.6)$$

$$= 2(6) \left\{ 1 + 2exp\left[\frac{(0.0572 - 0.058)/(4(0.0254))}{(0.058 - 0.0572)/0.0254} \right] \right\} \left\{ 0.021 + 13.6 \frac{0.572 - 0.058}{8618(0.058 - 0.0005)} + 0.24256 \left[\frac{0.0572 - 0.058}{8618(P_f - t_f)} \right]^{0.2} \right\} \frac{5.817^2}{1.14} + 1.136(2.21)^2 = 120.19 \text{ Pa}$$

The plenum recovery coefficient referred to the mean finned bundle conditions is given by

$$K_{reche} = K_{rec} \left(\frac{\rho_{avm}}{\rho_{avo}} \right) \left(\frac{m_{avo}}{m_{avm}} \right)^2 = -0.3 \left(\frac{1.1407}{1.135} \right) (1)^2 = -0.3019$$

Thus the total pressure drop over the finned bundle section of the system is calculated as

$$\Delta p_{fin} = \Delta p_{t(fin)} + K_{reche} \left(\frac{m_{avm}}{A_{fr}} \right)^2 \left(\frac{1}{2\rho_{avm}} \right) = 120.19 - 3.019 \left(\frac{60}{24} \right)^2 \left(\frac{1}{2(1.139)} \right) = 119.36 \text{ Pa} \quad (B.2.13)$$

The inlet loss coefficient for the air inlet into the second stage occurs between (1) and (3) from Figure B.2 and is referred to the mean bundle conditions as,

$$K_{cthe} = K_{ct(b)} \left(\frac{\rho_{avm}}{\rho_{avi}} \right) \left(\frac{m_{avi}}{m_{avm}} \right)^2 = 1.5 \left(\frac{1.141}{1.146} \right) (1)^2 = 1.4932$$

The bare tube bundle supports loss coefficient referred to the mean bundle conditions,

$$K_{ts(b)he} = K_{ts(b)} \left(\frac{\rho_{avm}}{\rho_{avi}} \right) \left(\frac{m_{avi}}{m_{avm}} \right)^2 = 0.5 \left(\frac{1.141}{1.146} \right) (1)^2 = 0.4977$$

Bundle loss coefficient under dry operation occurs between (4) and (5) in Figure B.2 and is given by equation (2.3.8) as,

$$K_{tb(d)} = 14.5049 Re_C^{-0.04678} = 4.5049(9383)^{-0.04678} = 9.4556 \quad (2.3.8)$$

Drift eliminator loss coefficient occurs between (5) and (6) in Figure B.2 as given by Kröger (2004) as,

$$K_{de} = 27.4892 Ry^{-0.14247} = 27.4892(222353)^{-0.14247} = 4.756 \quad (B.2.14)$$

Drift eliminators loss coefficient referred to the mean bundle conditions,

$$K_{dehe} = K_{de}\left(\frac{\rho_{avm}}{\rho_{avo}}\right)\left(\frac{m_{avo}}{m_{avm}}\right)^2 = 4.756\left(\frac{1.141}{1.135}\right)(1)^2 = 4.7782$$

Kröger (2004) suggests a conservative recovery coefficient in the plenum area of 0.3. This referred to the mean bare tube bundle conditions is given as,

$$K_{reche} = K_{rec}\left(\frac{\rho_{avm}}{\rho_{avo}}\right)\left(\frac{m_{avo}}{m_{avm}}\right)^2 = -0.3\left(\frac{1.141}{1.135}\right)(1)^2 = -0.3014$$

The total pressure drop over the second stage of the system is given as,

$$\begin{aligned} \Delta p_{bare(d)} = \frac{1}{2\rho_{avm}} &\left(K_{cthe} + K_{ts(b)he} + K_{tb(d)} + K_{dehe}\right. \\ &\left. + K_{reche}\right)\left(\frac{m_{avm}}{A_{fr}}\right)^2 \\ &= \frac{1}{2(1.141)}(1.4932 + 0.4977 + 9.4556 + 4.7782 \\ &- 0.3014)\left(\frac{16.58}{4.001}\right)^2 = 119.36\ Pa \end{aligned} \quad (B.2.15)$$

Which is equal to the pressure drop calculated for the finned tube bundle section from equation (B.2.13). The volume flow rate in the plenum region can be determined by adding the volume flow rate through each stage of the HDWCS as,

$$V_{ao(total)} = \left({}^{m_{avo}}/_{\rho_{avo}}\right)_{fin} + \left({}^{m_{avo}}/_{\rho_{avo}}\right)_{bare} = \left({}^{60}/_{1.138}\right)_{fin} + \left({}^{16.58}/_{1.135}\right)_{bare} = 67.3\ \text{m}^3/\text{s} \quad (B.2.16)$$

Thus the flow power required to move this amount of air with the determined pressure rise equal to the pressure drop,

$$P_{flow(dry)} = \Delta p_{bare(d)} V_{ao(total)} = (119.36)(67.3) = 80326\ \text{W} \quad (B.2.17)$$

B.3 Wet operation

B.3.1 Finned tube bundle

The same procedure is followed as demonstrated in Section B.2.1, but at a new work point. A draft equation for wet operation is presented in Section B.3.3. The converged outlet air- and process water temperatures from the finned bundle is calculated as,

Description	Symbol	Value	Unit
Process outlet temperature: Fin bundle	T_{po}	309.75	K
Air outlet temperature: Fin bundle	T_{ao}	309.07	K
Heat transfer rate: Fin bundle	Q	249872	W

B.3.2 Bare tube bundle

The outlet process water temperature calculated in Section B.3.1 is used as the process water inlet temperature for the second stage. The converged outlet temperatures of air and process water for the second stage are calculated as:

Description	Symbol	Value	Unit
Process outlet temperature: Bare bundle	T_{po}	308.35	K
Air outlet temperature: bare bundle	T_{ao}	302.97	K
Deluge water mean temperature	T_{dwm}	307.91	K
Air mass flow rate: Bare bundle	$m_{avi(b)}$	9.319	kg/s

The air entering the bare tube bundle is at the same condition as the air entering the finned tube bundle.

The specific heats of air and water vapour are calculated at (T_{ai} - 273.15)/2 = 298.15 K as,

Specific heat of air	$c_{p(ai)}$	1006.62	J/kgK	(A.1.2)
Specific heat of vapour	$c_{p(vi)}$	1876.19	J/kgK	(A.2.2)

The remaining properties of the air at the inlet of the bare tube bundle are calculated at T_{ai} = 305.15 K as

Saturated pressure	p_{vi}	2982.78	Pa	(A.2.1)
Humidity ratio	w_i	0.01558	kg/kg d.a.	(A.3.5)
Air mixture enthalpy	i_{mai}	72129.86	J/kg	(A.3.6b)
Air density	ρ_{avi}	1.14596	kg/m^3	(A.3.1)
Air viscosity	μ_{ai}	1.8705E-05	kg/ms	(A.1.3)

Vapour viscosity	μ_{vi}	9.9579E-06	kg/ms	(A.2.3)
Air mixture viscosity	μ_{avi}	1.8536E-05	kg/ms	(A.3.3)

The specific heats of air and water vapour are calculated at (T_{ao} - 273.15)/2 = 288.06 K as,

Specific heat of air	$c_{p(ao)}$	1006.59	J/kgK	(A.1.2)
Specific heat of vapour	$c_{p(vo)}$	1875.26	J/kgK	(A.2.2)

The following properties of the air at the outlet of the bare bundle are calculated at $T_{ao} = 302.97$ K as,

Humidity ratio	w_{os}	0.02703	kg/kg d.a.	(A.3.5)
Saturated air mixture enthalpy	i_{maos}	99155.52	J/kg	(A.3.6b)
Air density	ρ_{avo}	1.1466	kg/m^3	(A.3.1)
Dynamic viscosity outlet air	μ_{avo}	1.8325E-05	kg/ms	(A.3.3)

The properties of air at the at the deluge water-air interface are evaluated at the mean deluge water temperature $T_{dwm} = 307.91$ K as,

Specific heat of air	$c_{p(adwn)}$	1007.27	J/kgK	(A.1.2)
Specific heat of vapour	$c_{p(vdwm)}$	1893.71	J/kgK	(A.2.2)
Saturated pressure	p_{vdwm}	5549.88	Pa	(A.2.1)
Humidity ratio	w_{dwm}	0.03623	kg/kg d.a.	(A.3.5)
Air mixture enthalpy	i_{masdwm}	128040.27	J/kg	(A.3.6b)

The process water properties are evaluated at the mean water temperature ($T_{pm} = \frac{T_{pi}+T_{po}}{2} = 309.05$ K) in the bare tube bundles as,

Density	ρ_{pm}	993.82	kg/m^3	(A.4.1)
Specific heat	c_{pp}	4176.99	kJ/kgK	(A.4.2)
Dynamic viscosity	μ_{pm}	7.0564E-04	kg/ms	(A.4.3)
Thermal conductivity	k_p	0.6258	W/m^{2}K	(A.4.4)

The deluge water properties are evaluated at the final deluge water temperature of $T_{dwm} = 307.91$ K as,

Density	ρ_{dwm}	994.21	kg/m^3	(A.4.1)
Specific heat	c_{pdwm}	4177.18	kJ/kgK	(A.4.2)
Dynamic viscosity	μ_{dwm}	7.2194E-04	kg/ms	(A.4.3)
Thermal conductivity	k_{dwm}	0.6243	W/m^{2}K	(A.4.4)

The dry air mass flow rate is calculated from the inlet humidity ratio as

$$m_a = \frac{m_{avi}}{1+w_i} = \frac{9.319}{1+0.0156} = 9.176 \text{ kg/s} \quad \text{(B.2.3)}$$

The outlet air mixture mass flow rate is calculated from the outlet humidity ratio as

$$m_{avo} = m_a(1 + w_{os}) = 9.176(1 + 0.027) = 9.424 \text{ kg/s} \quad \text{(B.3.1)}$$

The mean air mixture mass flow rate is determined as

$$m_{avm} = \frac{m_{avi}+m_{avo}}{2} = \frac{9{,}319+9.424}{2} = 9.371 \text{ kg/s} \quad \text{(B.3.2)}$$

The frontal area (A_{fr}), critical area (A_c), inside (A_p) and outside (A_a) tube areas of the bare tube bundle remain unchanged from dry operation. The critical air mass velocity is calculated from equation (B.2.10) as,

$$G_c = \frac{m_{avm}}{A_c} = \frac{9.371}{1.8085} = 5.192 \text{ kg/m}^2\text{s} \quad \text{(B.2.10)}$$

The approximate water flow rate over half a tube per unit tube length is,

$$\Gamma_m = \frac{m_{dw}d_o}{2n_{tr}L_bP_t} = \frac{12(0.019)}{2(10.5)(10)(0.038)} = 0.0286 \text{ kg/sm}^2$$

The mean Reynolds number for the deluge water and air flow rate across the bundle is required in order to determine the mass and heat transfer coefficients from equations (2.3.11) and (2.3.12). The Reynolds number of the mean air flow is calculated as,

$$Re_{avm} = \frac{m_{avm}d_o}{A_c\mu_{avm}} = \frac{(9.371)(0.019)}{(1.805)(1.843\times10^{-5})} = 1219 \text{ kg/m}^2\text{s}$$

and the Reynolds number for the deluge water is calculated as,

$$Re_{dwm} = \frac{m_{dw}d_o}{A_c\mu_{dwm}} = \frac{(12)(0.019)}{(1.805)(7.22\times10^{-4})} = 158 \text{ kg/m}^2\text{s}$$

A correlation for the mass transfer coefficient is given by,

$$h_d = 5.5439 \times 10^{-8} Re_{avm}^{0.9} Re_{dwm}^{0.15} d_o^{-1.6} = 5.5439 \times 10^{-8}(1219)^{0.9}158^{0.15}0.019^{-1.6} = 0.1221 \text{ kg/sm}^2 \quad \text{(2.3.11)}$$

similarly the heat transfer coefficient as given as,

$$h_{dw} = 2102.9\left(\frac{\Gamma_m}{d_o}\right)^{1/3} = 2102.9\left(\frac{0.0286}{0.019}\right)^{1/3} = 1620.5 \text{ W/m}^2\text{K} \quad \text{(2.3.12)}$$

The air side number of transfer units (NTU_a) is determined with the mass transfer equation,

$$NTU_a = \frac{A_a h_d}{m_a} = \frac{150.42(0.1221)}{9.176} = 0.6604 \text{ W/m}^2\text{K} \tag{3.2.7}$$

The outlet air enthalpy is calculated as,

$$\begin{aligned} i_{mao} &= i_{masdwm} - (i_{masdwm} - i_{mai})e^{-NTU_a} \\ &= 128040 - (128040 - 72130)e^{-0.66} = 99155.52 \text{ J/kg} \end{aligned} \tag{3.2.6}$$

The process water Reynolds number is given by,

$$Re_p = \frac{\rho_{pm} v_p d_{i(b)}}{\mu_{pm}} = \frac{(9933.82)(1.735)(0.016)}{7.056\times10^{-4}} = 38610 \tag{B.2.6}$$

The friction factor inside the tube is calculated as,

$$\begin{aligned} f_D &= (1.82log_{10}(Re) - 1.64)^{-2} = (1.82log_{10}(38610) - 1.64)^{-2} \\ &= 0.0222 \end{aligned} \tag{2.3.4}$$

The internal heat transfer coefficient is calculated from,

$$h_p = \frac{0.125 f_D Re Pr}{1.07 + 12.7(0.125 f_D)^{0.5}\left(Pr^{0.667} - 1\right)} \frac{k_p}{d_i} \tag{2.3.3}$$

$$= \frac{0.125(0.022)(38610)(4.71)}{1.07+12.7(0.125(0.022))^{0.5}\left((4.71)^{0.667}-1\right)} \frac{0.626}{0.016} = 8745.29 \text{ W/m}^2\text{K}$$

The overall heat transfer coefficient, based on the outside area is given by,

$$U_a = \left[\frac{d_o}{h_p d_i} + \frac{d_o ln\frac{d_o}{d_i}}{2k_t} + \frac{1}{h_{dw}}\right]^{-1} \tag{3.2.12}$$

$$= \left[\frac{0.019}{(8745.3)(0.016)} + \frac{(0.019)ln\left(\frac{19}{16}\right)}{2(45)} + \frac{1}{1620.5}\right]^{-1} = 1690.42 \text{ W/m}^2\text{K}$$

The NTU for the process water is given by,

$$NTU_p = \frac{A_a U_a}{m_p c_{ppm}} = \frac{(150.42)(1690.42)}{(42.6)(4177)} = 1.4290 \text{ W/m}^2\text{K} \tag{3.2.11}$$

The amount of heat transferred to the air stream is calculated from the first definition of equation (3.2.4) as,

$$Q_a = m_a(i_{mao} - i_{mai}) = 9.176(99155 - 72129.9) = 247977 \text{ W} \tag{B.3.3}$$

The amount of heat transferred from the process water is calculated from the second definition of equation (3.2.4) as,

$$Q_p = m_p c_{ppm}(T_{pi} - T_{po}) = 42.6(4176.9)(309.745 - 308.35) \\ = 247977 \text{ W} \quad \text{(B.3.4)}$$

Equations (B.3.3) and (B.3.4) is in good agreement and as such the process has converged. The process outlet water temperature is given by equation (3.2.10) as,

$$T_{po} = T_{dwm} + (T_{pi} - T_{dwm})e^{-NTU_p} \quad \text{(3.2.10)}$$
$$= 307.91 + (309.75 - 307.91)e^{-1.429} = 308.35 \text{ K}$$

And the deluge water mean temperature is given by equation (3.2.13) as,

$$T_{dwm} = T_{pi} - \frac{m_a(i_{masdwm} - i_{mai})(1 - e^{-NTU_a})}{m_p c_{ppm}(1 - e^{-NTU_p})} \quad \text{(3.2.13)}$$

$$= 309.75 - \frac{9.176(128040 - 72129.9)(1 - e^{-0.66})}{42.6(4176.9)(1 - e^{-1.429})} = 307.91 \text{ K}$$

B.3.3 Draft equation

From the required flow rate calculated from equation (B.2.17) in Section 0, the mass flow rate over each stage is solved iteratively noting the flow power remains unchanged as discussed in Chapter 5. The air mass flow rate over each stage together with the system pressure drop under wet operation converged to,

Description	Symbol	Value	Unit
Flow power from dry operation	$P_{flow(dry)}$	8032.6	W
Air mass flow rate: Finned tube bundle	$m_{avi(f)}$	62.41	kg/s
Air mass flow rate: Bare tube bundle	$m_{avi(b)}$	9.319	kg/s
System Pressure loss: Wet operation	Δp_{fin}	127.63	Pa

The same procedure is followed as in section 0 with a new air mass flow rate for the finned tube bundle and air properties evaluated at the temperatures from Section B.3.1. The new total pressure drop across the first stage is determined from equation (B.2.13) as,

$$\Delta p_{fin} = \Delta p_{t(fin)} + K_{reche}\left(\frac{m_{avm}}{A_{fr}}\right)^2\left(\frac{1}{2\rho_{avm}}\right) \quad \text{(B.3.5)}$$
$$= 128.53 - \quad 0.302\left(\frac{62.41}{24}\right)^2\left(\frac{1}{2(1.131)}\right) = 127.63 \text{ Pa}$$

As the bare tube bundle is operated wet, the flow resistances differ from dry operation. A rain zone and spray zone as well as water inside the bare tube bundle

increases the air-side pressure drop across the second stage of the HDWCS. The draft calculations for the second stage are repeated in this section to highlight the differences in pressure drop under dry and wet operation.

The inlet loss coefficient for the air inlet into the second stage occurs between (1) and (3) from Figure B.2 and is referred to the mean bundle conditions as,

$$K_{cthe} = K_{ct(b)} \left(\frac{\rho_{avm}}{\rho_{avi}}\right) \left(\frac{m_{avi}}{m_{avm}}\right)^2 = 1.5\left(\frac{1.1462}{1.1459}\right)\left(\frac{9.318}{9.371}\right)^2 = 1.4837$$

The bare tube bundle supports loss coefficient referred to the mean bundle conditions,

$$K_{ts(b)he} = K_{ts(b)} \left(\frac{\rho_{avm}}{\rho_{avi}}\right) \left(\frac{m_{avi}}{m_{avm}}\right)^2 = 0.5\left(\frac{1.1462}{1.1459}\right)\left(\frac{9.318}{9.371}\right)^2 = 0.4945$$

For the rain zone loss coefficient (4) in Figure B.2, the diffusion coefficient is given in Kröger (2004) as,

$$\begin{aligned} D_{rz} &= 0.04357 T_{ai}^{1.5} \left(\frac{1}{M_a} + \frac{1}{M_v}\right)^{0.5} \left[p_{atm}\left(V_a^{\frac{1}{3}} + V_v^{\frac{1}{3}}\right)^2\right]^{-1} \\ &= 0.04357 T_{ai}^{1.5} \left(\frac{1}{28.97} + \frac{1}{18.02}\right)^{0.5} \left[101328\left(29.9^{\frac{1}{3}} + 18.8^{\frac{1}{3}}\right)^2\right]^{-1} \\ &= 2.0753 \times 10^{-5} \text{ m}^2/\text{s} \end{aligned}$$

Where $V_a = 29.9$ and $V_v = 18.8$ are the molecular volumes of air and water vapour respectively. M_a and M_v are the molecular masses of air and water vapour respectively. The Schmidt number foe the rain zone is calculated as,

$$Sc_{rz} = \frac{\mu_{avi}}{\rho_{avi} D_{rz}} = \frac{1.028\times10^{-5}}{(1.122)(2.0753\times10^{-5})} = 0.7794$$

The deluge water velocity in the rain zone is calculated as,

$$v_{dw} = \frac{m_{dw}}{\rho_{dw} A_{fr}} = \frac{12}{(994.2)(4.009)} = 3.0107 \times 10^{-3} \text{ m/s}$$

The air velocity in the rain zone is calculated as,

$$v_{avi} = \frac{m_{avi}}{\rho_{avi} A_{fr}} = \frac{9.319}{1.122(4.009)} = 2.0284 \text{ m/s}$$

The constant coefficients in the rain zone loss coefficient equation is given by,

$$a_\mu = 3.061 \times 10^{-6} \left(\frac{\rho_{dw}^4 g^9}{\sigma_{dw}}\right)^{0.25} = 3.061 \times 10^{-6} \left(\frac{994.2^4 9.81^9}{0.07}\right)^{0.25} = 1.0060$$

$$a_\rho = \frac{998}{\rho_{dw}} = \frac{998}{994.2} = 1.0038$$

$$a_v = 73.298\left(\frac{\sigma_{dw}^3 g^5}{\rho_{dw}^3}\right)^{0.25} = 73.298\left(\frac{0.07^3 9.81^5}{994.2^3}\right)^{0.25} = 0.9831$$

$$a_L = 6.122\left(\frac{\sigma_{dw} g}{\rho_{dw}}\right)^{0.25} = 6.122\left(\frac{(0.07)(9.81)}{994.2}\right)^{0.25} = 0.9941$$

The rain zone loss coefficient is presented in Kröger (2004) as,

$$K_{rz} = 1.5 a_v v_{dw}\left(\frac{H_{in}}{d_d}\right)$$
$$\Big[0.219164 + 8278.7 a_\mu \mu_{avi} - 0.30487 a_\rho \rho_{avi}$$
$$+ 0.954153\left\{\begin{matrix}0.328467\, exp(135.7638 a_L d_d)\\ +0.47\end{matrix}\right\}\left\{26.28482(a_L H_3)^{-2.95729}\right.$$
$$\left. + 0.56\right\} exp\left\{\begin{matrix}ln(0.204814\, exp(0.066518 a_L L_b) + 0.21)\\ (3.9186\, exp(-0.3 a_L H_3))(0.31095\, ln(a_L d_d) + 2.63745)\end{matrix}\right\}\left\{2.17754(\right.$$
$$\left. + 0.21\right\}\Big] = 1.5(0.9831)\left(3.0107 \times 10^{-3}\right)\left(\frac{0.2}{0.0004}\right)$$
$$\Big[0.219164 + 8278.7(1.0060)\left(1.8536 \times 10^{-5}\right) - 0.30487(1.0038)(1.146)$$
$$+ 0.954153\left\{0.328467\, exp\left(135.7638(0.9941)(0.0004)\right)\right.$$
$$\left. + 0.47\right\}\left\{26.28482((0.9941)(0.2))^{-2.95729}\right.$$
$$\left. + 0.56\right\} exp\left\{ln\left(\begin{matrix}0.204814\, exp\left(0.066518(0.9941)(10)\right)\\ +0.21\end{matrix}\right)(3.9186\, exp(-0.3(0.994\right.$$
$$\left. + 2.63745)\right\}\left\{2.177546(0.9831)(2.0284))^{-1.46541} + 0.21\right\}\Big] = 0.2445$$

The rain zone loss coefficient is referred to the mean bundle conditions as,

$$K_{rzhe} = K_{rz}\left(\frac{\rho_{avm}}{\rho_{avi}}\right)\left(\frac{m_{avi}}{m_{avm}}\right)^2 = 0.2445\left(\frac{1.1462}{1.1459}\right)\left(\frac{9.318}{9.371}\right)^2 = 0.2419$$

Bundle loss coefficient under wet operation between (4) and (5) in Figure B.2 is given by equation (2.3.13) as,

$$K_{tb(w)} = 74.227\left(\frac{m_{avm}}{A_c}\right)^{-0.1104}\left(\frac{\Gamma_{dw}}{d_o}\right)^{0.1955} T_{dwm}^{-0.08875}$$
$$= 74.227\left(\frac{9.371}{1.805}\right)^{-0.1104}\left(\frac{0.028}{0.019}\right)^{0.1955}(307.91 - 273.15)^{-0.08875} \qquad (2.3.15)$$
$$= 45.69$$

The spray zone loss coefficient (5) in Figure B.2 is given by Cale (1982). This, together with the water distribution system and referred to the mean bundle conditions are given by,

$$K_{sphe} = \left[H_{sp}\left(0.4\frac{G_{dw}}{G_{av}} + 1\right) + K_{wd}\right]\left(\frac{\rho_{avm}}{\rho_{avo}}\right)\left(\frac{m_{avo}}{m_{avm}}\right)^2 \quad \text{(B.3.6)}$$

$$= \left[0.15\left(0.4\frac{3}{2.324} + 1\right) + 0.5\right]\left(\frac{1.146}{1.147}\right)\left(\frac{9.423}{9.371}\right)^2 = 0.7352$$

Drift eliminator loss coefficient between (5) and (6) in Figure B.2 is given equation (B.2.14) as,

$$K_{de} = 27.4892Ry^{-0.14247} = 27.4892(127562)^{-0.14247} = 5.1481 \quad \text{(B.2.14)}$$

Drift eliminator loss coefficient referred to the mean bundle condition as,

$$K_{dehe} = K_{de}\left(\frac{\rho_{avm}}{\rho_{avo}}\right)\left(\frac{m_{avo}}{m_{avm}}\right)^2 = 5.1481\left(\frac{1.146}{1.147}\right)\left(\frac{9.423}{9.371}\right)^2 = 5.2045$$

The plenum recovery loss coefficient remains unchanged. Referred to the mean bare tube bundle conditions as,

$$K_{reche} = K_{rec}\left(\frac{\rho_{avm}}{\rho_{avo}}\right)\left(\frac{m_{avo}}{m_{avm}}\right)^2 = -0.3\left(\frac{1.146}{1.147}\right)\left(\frac{9.423}{9.371}\right)^2 = -0.3033$$

The total pressure drop over the second stage of the system under wet operation is given as,

$$\Delta p_{bare(w)} = \left(K_{ct(f)he} + K_{rzhe} + K_{ts(b)he} + K_{tb(w)} + K_{sphe} + K_{dehe} + K_{reche}\right)\left(\frac{m_{avm}}{A_{fr}}\right)^2\left(\frac{1}{2\rho_{avm}}\right) \quad \text{(B.3.7)}$$

$$= (1.4837 + 0.2419 + 0.4945 + 45.69 + 0.7352 + 5.2045 - 0.3033)\left(\frac{9.371}{4.001}\right)^2\left(\frac{1}{2(1.146)}\right) = 127.63 \text{ Pa}$$

The pressure drop calculated in equation B.3.7) agrees with that calculated in equation (B.3.5) and as such the air flow rate under wet operation has converged. The volume flow rate in the plenum can by determined by adding the volume flow rate through each stage of the HDWCS as,

$$V_{ao(total)} = \left({}^{m_{avo}}/_{\rho_{avo}}\right)_{fin} + \left({}^{m_{avo}}/_{\rho_{avo}}\right)_{bare} \quad \text{(B.2.16)}$$

$$= \left({}^{62.41}/_{1.131}\right)_{fin} + \left({}^{9.424}/_{1.147}\right)_{bare} = 62.9 \text{ m}^3/\text{s}$$

Thus the flow power required to move this amount of air with the determined pressure rise equal to the pressure drop,

$$P_{flow(dry)} = \Delta p_{bare(d)} V_{ao(total)} = 127.63(62.9) = 8023.6 \text{ W} \quad \text{(B.3.8)}$$

Which is the same flow power as calculated in equation (B.2.17), in Section B.2. The converged values for the flow power under dry and wet operation are in agreement and as such the pressure drop values converged correctly.

C. CALIBRATION OF THERMOCOUPLES AND PRESSURE TRANSDUCERS

The experimental work from Chapter 4 required pressure and temperature measurements to be made in order to calculate air-side pressure drop across and air flow rate through the experimental apparatus. Temperature measurements together with formulas from Appendix A was used to calculate fluid properties.

C.1 Equipment

The equipment used to record temperature and pressure were supplied by the Department of Mechanical and Mechatronic (M & M) engineering at Stellenbosch University (SU).

Thermocouples were manufactured by Temperature Control (Pty) Ltd. The thermocouples were wired to an Agilent data card and a Keysight LXI data logger was used to record temperature measurements. Endress & Hauser pressure transducers, fixed to the wind tunnel, were used to measure the air-side pressure drop across the experimental apparatus and across nozzles inside the wind tunnel to measure the air mass flow rate. Atmospheric pressure was recorded from a mercury barometer installed in the heat transfer laboratory.

Thermocouple calibration was done with a Fluke Field Metrology well and a reference thermocouple device (RTD). Pressure transducer calibration was carried out with a Betz micro manometer 5000 hereafter referred to as the Betz.

Table C.1 presents the instrument name and serial number used for this study

Table C.1: Equipment serial numbers

Instrument	Serial number	
Agilent data card	MY41153683	
Keysight LXI data logger	34972A	
Fluke Field Metrology well	9142	
Reference thermocouple device	1344029856	
Endress & Hauser pressure transducers	FA0067109D	FA008A2109D
	FA00892109D	
Betz micro manometer 5000	226502	
Mercury barometer	Z27186	

C.2 Type-T thermocouples

C.2.1 Calibration procedure

Eight type-T thermocouples with 100 mm long and 1.6 mm thick probes, were used to measure the water and air temperatures during experiments. All 8 thermocouples were calibrated at once. The eight thermocouples equally surrounded the RTD when inserted into the bullet. The aluminium bullet fits neatly into the Field metrology well ensuring a tight fit and uniform heat distribution.

The calibration procedure was carried out in the following sequence:

1. The Field metrology well was adjusted from 10 ºC to 60 ºC and back to 10 C in intervals of 10 ºC. Once the Field metrology well reached a set temperature the resistance of the RTD was monitored for 10 min before the resistance thereof was recorded.
2. The resistance of the RTD was used to calculate the true temperature by relaying the resistance in ohm to a temperature in degrees Celsius. This relation is presented as equation (C.2.1).
3. Once steady state for the reference probe was established, the thermocouple temperature readings were recorded with Agilent Bench link data logging software over a period of 4 min at 10 sec intervals producing 24 readings for each thermocouple. The average from these 24 readings was assumed as the measured temperature for each thermocouple.
4. The Field metrology well was set to the next temperature interval and allowed to reach steady state.
5. Steps 2 to 4 were repeated for each temperature interval. Once all the temperature readings were recorded the Field metrology well was switched off. The recorded data was processed in a spreadsheet to obtain correlations in order to determine the true temperature measured during experiments.

C.2.2 Results

The temperature measured by each thermocouple was plotted against the true temperature measured by the reference probe. The true temperature, measured by the reference probe was determined from the resistance of the RTD together with equation (C.2.1) as,

$$T_{true} = 0.001111611\Omega_{Ref}^2 + 2.32652102\Omega_{ref} - 243.768049 \qquad \text{(C.2.1)}$$

where the true temperature (T_{true}) in degrees Celsius. The measured temperature plotted against the true temperature are presented in Figure C.1.

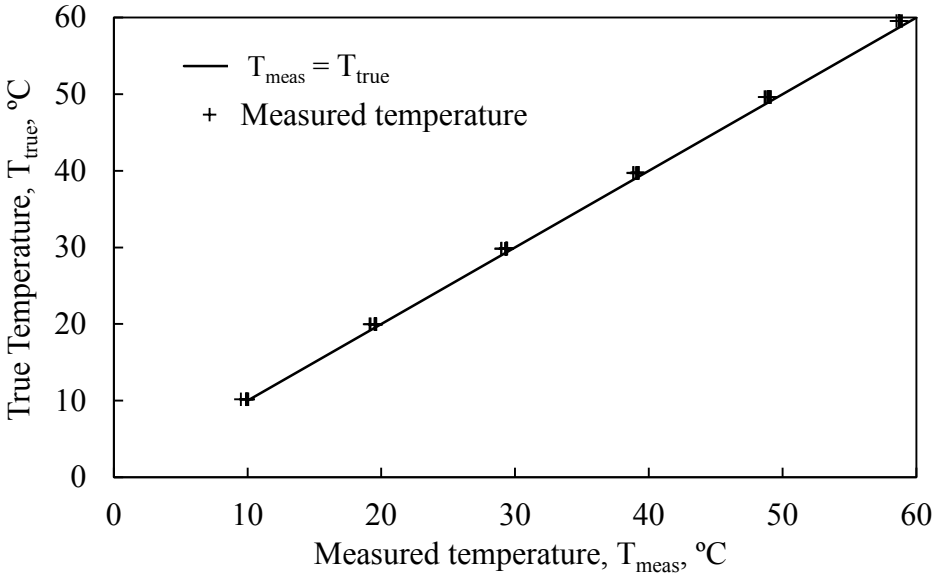

Figure C.1: Measured temperatures for thermocouples

From Figure C.1, the measured temperatures are slightly higher than the true temperature. By fitting linear lines through the measured temperatures for each thermocouple, a linear equation for each thermocouple was developed to relate the measured value to the true value. The linear equation is of the form presented as equation (C.2.2).

$$T_{true} = mT_{meas} + c \qquad \text{(C.2.2)}$$

where the gradient (m) and the y axis cut-off value (c) for each thermocouple is presented in Table C.2.

Table C.2: Linear equation values for each thermocouple

Thermocouple	Gradient (m)	y axis cut-off (c)	Max err (ºC)	Avg err (ºC)
1	1.00585	0.67407	0.072	0.034
2	1.00664	0.12654	0.065	0.026
3	1.00900	0.24033	0.075	0.026
4	1.01160	0.12829	0.085	0.036
5	1.01215	0.13929	0.078	0.028
6	1.00652	0.23535	0.059	0.022
7	1.01327	0.06768	0.088	0.031
8	1.01038	0.22380	0.059	0.022

From Table C.2, the maximum error (Max err) between the true temperature and that predicted by equation (C.2.2) was less than 0.1 ºC for all thermocouples with the average absolute error (Avg err) ranging between 0.02 ºC and 0.036 ºC.

C.3 Endress & Hauser pressure transducers.

C.3.1 Calibration procedure

Three pressure transducers were used to measure a difference in air pressure across the experimental apparatus and inside the wind tunnel. The first pressure transducer measured the air pressure drop across the bare tube bundle during experiments. The second measured the air pressure drop across the nozzle located inside the wind tunnel, to determine the air mass flow rate through the system. The third pressure transducer measured the difference in air pressure outside and inside the wind tunnel at the nozzle inlet which was used to determine the absolute air pressure at that point. The calibration procedure was carried out with the following steps:

1. Initially a positive pressure was induced inside the Betz by blowing air into the Betz's positive chamber.
2. The pressure transducer to be calibrated was zeroed.
3. The positive chamber outlet of the Betz was attached to the positive pressure inlet of the pressure transducer.
4. The pressure readings on the Betz and the pressure transducer were recorded.
5. Air was let out of the Betz's positive chamber via a valve to establish a new set point.
6. Steps 4 and 5 were repeated for several set points.
7. Steps 1 to 6 were repeated for each pressure transducer.

After all three pressure transducers were calibrated, the Betz's light was switched off and all remaining air let out.

C.3.2 Results

The measured pressure drop is plotted against the true pressure difference from the Betz manometer in Figure C.2

From Figure C.2, a linear relationship between the pressure transducers and Betz manometer is observed. The measured pressure is related to the true pressure by a similar procedure than that presented in Section C.2 for the thermocouple. The linear equation is of the form presented as equation (C.3.1).

$$\Delta P_{true} = m\Delta P_{meas} + c \qquad \text{(C.3.1)}$$

Where the gradient (m) and the y axis cut-off value (c) for each pressure transducer is presented in Table C.2.

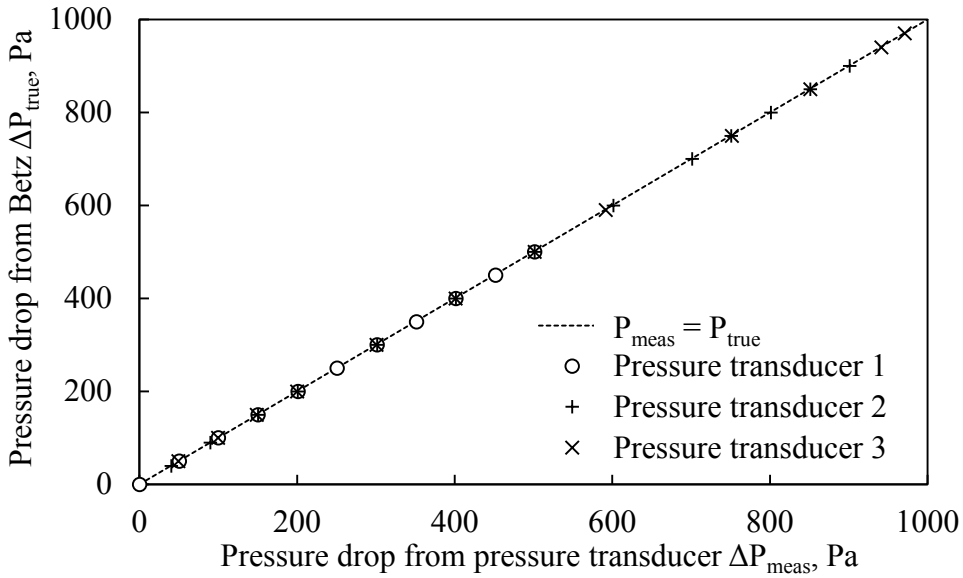

Figure C.2: Measured pressure drops for the pressure transducers.

Table C.3: Linear equation values for each pressure transducer

Pressure transducer	Gradient (m)	y axis cut-off (c)	Max err (Pa)	Avg err (Pa)
1	0.99669	-0.27882	1.9	1.1
2	0.99879	-0.44965	1.6	1.1
3	0.99744	0.48073	1.8	1.1

From Figure C.2, the maximum error (Max err) between the true pressure drop and that predicted by equation (C.3.1) was less than 2 ºPa for all pressure transducers with the average absolute error (avg err) 1.1 Pa.

D. FINNED TUBE BUNDLE MODEL VALIDATION

The core model of the finned tube bundle used the sample calculation of Ackers to validate the converged values based on his input parameters before subsequent components were added. The validation is presented in Table D.1.

Table D.1: Finned tube bundle validation

Description	Symbol	Unit	Model	Ackers (2012)	Diff
Process fluid density	ρ_p	kg/m^3	981.8819	981.8819	0.000%
Specific Heat	cp_p	J/kg	4185.8	4185.8	-0.001%
Dynamic Viscosity	μ_p	kg/ms	0.000446	0.000446	0.000%
Thermal Conductivity	k_p	W/mK	0.6556	0.6556	-0.007%
Prandtl Number	Pr_p		2.847419	2.8474	0.001%
Specific heat for air	cp_a	J/kgK	1007.3	1007.3	-0.002%
Dynamic Viscosity	μ_a	kg/ms	1.88E-05	1.88E-05	0.001%
Thermal Conductivity	k_a	W/mK	0.0269	0.0269	-0.172%
Prandtl Number	Pr_a		0.70684	0.7068	0.006%
Heat transfer rate to air	Q_a	W	3616772	3616750	0.001%
heat transfer rate from process water	Q_p	W	3615304	3616750	-0.040%
Internal Reynolds number	Re_p	-	66469.2	66424.0	0.068%
Internal friction Coefficient	f_D	-	0.0196	0.0196	0.159%
Internal Nusselt Number	Nu_p	-	280.99	278.97	0.723%
Internal heat transfer coeff.	h_p	W/m^{2}K	8688.9	8634.7	0.628%
LMTD	ΔT_{lm}	K	27.3798	27.3798	0.000%
Correction factor variables	φ_1	-	0.5830	0.5830	-0.008%
Correction factor variables	φ_2	-	0.5026	0.5026	0.004%
Correction factor variables	φ_3	-	0.4560	0.4560	0.007%
Reynolds based on critical air mass velocity	G_c	kg/sm^2	7.888	7.8803	0.092%
Area ratio	A/A_r	-	21.557	21.379	0.834%
Nusselt from Ganguli	Nu	-	55.062	55.697	-1.140%
Airside heat transfer coeff.	h_a	W/m^{2}K	58.21	58.88	-1.140%
$A_f + A_r$	A_a	m^2	3096.300	3070.750	0.832%
Proses surface area	A_p	m^2	119.883	119.770	0.094%
Fin efficiency parameter 1	φ	-	1.608	1.596	0.726%
Fin efficiency parameter 2	b	m^{-1}	35.310	35.513	-0.572%
Critical flow area	A_c	m^2	15.085	15.099	-0.092%
Reynolds based on root diameter	Re_r	-	10631.6	10622	0.090%